Optical absorption studies in ion implanted and amorphous semiconductors – Investigations in some tetrahedrally co-ordinated and chalcogenide materials

Thesis submitted to

COCHIN UNIVERSITY OF SCIENCE AND TECHNOLOGY

for the award of the degree of

DOCTOR OF PHILOSOPHY

by

Alex Mathew

Department of Instrumentation
Cochin University of Science and Technology
Cochin – 682 022

June 2004

CERTIFICATE

Certified that the work presented in this thesis is based on the bona fide work done by Mr.Alex Mathew under my guidance in the Department of Instrumentation, Cochin University of Science and Technology, and has not been included in any other thesis submitted previously for the award of any degree.

Cochin-682 022   Dr.K.N.Madhusoodanan

                                                        Supervising Guide

DECLARATION

Certified that the work presented in this thesis is based on the original work done by me under the guidance of Dr.K.N.Madhusoodanan, Reader, Department of Instrumentation, Cochin University of Science and Technology, and has not been included in any other thesis submitted previously for the award of any degree.

Cochin-682 022   Alex Mathew

Contents

Chapter 2

Chapter 3

PREPARATION AND OPTICAL CHARACTERISATION OF Ge_xSe_{100-x} AND As_xSe_{100-x} THIN FILMS

Chapter 4

SUBGAP OPTICAL ABSORPTION STUDIES IN BORON IMPLANTED SILICON

Chapter 5

THERMAL DIFFUSIVITY MEASUREMENTS OF Ge_xSe_{100-x} AND As_xSe_{100-x} THIN FILMS USING PHOTOTHERMAL BEAM DEFLECTION TECHNIQUE

Chapter 6

OPTICAL ABSORPTION STUDIES IN NITROGEN IMPLANTED
Ge_xSe_{100-x} AND As_xSe_{100-x} THIN FILMS **150**

Chapter 7
SUMMARY AND CONCLUSIONS **170**

PREFACE

The study of non-crystalline materials is an active area of research in solid state physics mainly because of the enormous and diverse applications of these materials like xerography, memory and switching elements and energy conversion devices such as solar cells. They differ from their crystalline counter parts by the absence of long range order. Their interesting electrical, optical and magnetic properties along with the wide flexibility in preparation and composition make them unique in several applications. Like crystalline materials, non-crystalline materials can be ionic, covalent, metallic or van der Waals' bonded materials. Consequently, they can be insulating, semiconducting or metallic in nature.

Amorphous semiconductors can be generally classified into two groups as tetrahedrally coordinated semiconductors like a-Si, a-Ge etc and chalcogenide semiconductors like Ge-Se, As-Se etc. Chalcogenide glasses contain one or more of the chalcogen elements, S, Se or Te of the sixth group of the periodic table. The four-fold coordination in Si leads to symmetrical bonding and the formation of rigid structures, while the two-fold coordination in chalcogens is highly asymmetrical and the structure gives rise to greater degree of flexibility for interatomic bonds. Like other glassy solids, these

materials also possess only short-range order and because of this, the theories developed for crystalline materials cannot directly be applied to them.

Chalcogenide glasses form an important class of amorphous solids. They have very interesting physical properties and can be prepared in the bulk as well as thin film forms. One of the greatest advantages of these glasses is the composition dependent tunability of their properties, which enables one to design materials for specific requirements. They have potential technological applications such as materials for threshold and memory switching, inorganic photoresist, xerography, IR detection and transmission etc. These materials are suitable for IR optical elements such as cell windows and prisms and as FIR beam condensers, splitters and other accessories, since they do not absorb IR radiation. Many of these glasses can be formed by the conventional melt quenching technique over a wide composition range making them suitable model systems for systematic studies on composition dependent properties.

In order to explain the features observed in the composition dependence of various properties of chalcogenide glasses, various models like random network models and topological models have been proposed. According to the chemically ordered covalent network (COCN) model, heteropolar bonding is maximized, there by favouring chemical order. Topological models use the concept of average coordination number Z and interpret the properties of chalcogenide glasses in terms of Z.

We have selected silicon as a representative of the family of tetrahedrally co-ordinated materials and the glass systems Ge_xSe_{100-x} ($5 \leq x \leq 40$) and As_xSe_{100-x} ($10 \leq x \leq 60$) as representatives of the class of chalcogenides for our studies. For most of the device applications, chalcogenide materials are used in the form of thin films. The optical properties of thin films are sensitive to many parameters including their thickness and hence can provide important information on both device and materials characteristics. In this context, we have carried out the optical characterization of the thin film samples of the systems Ge-Se and As-Se, which includes the determination of their optical band gaps and refractive indices. For the preparation of thin films, we have also designed and fabricated a vacuum coating unit capable of creating ultimate pressures of about 10^{-5} Torr.

It has long been known that intrinsic chalcogenide glasses behave like p-type semiconductors and are insensitive to doping in small amounts. This behaviour is attributed to the local valence saturation of the dopant atoms. Fermi level is considered to be pinned due to the equilibrium between positively and negatively charged defect states, known as valence alternation pairs (VAPs). The presence of a large number of defect states in the band gap makes them normally insensitive to impurity doping. Incorporation of impurities into a semiconductor by high-energy ions is a non-equilibrium process which can result in intriguing property changes in the material. The ion-solid interaction process can lead to the modification of the composition,

structure, electronic properties and topography of the semiconductor. Ion implantation is a key technology for the fabrication of doped layers in silicon semiconductor microelectronic devices. In this context, we have carried out a study of modification effects in the two classes of materials of amorphous semiconductors by the technique of ion implantation. Optical absorption measurements in these samples have been carried out by Photothermal Deflection Spectroscopy (PDS), a highly sensitive technique which allows the detection of low levels of absorption, typical of the subgap region of semiconductors.

During the past few years, thermal wave physics has emerged as a valuable tool for the characterization and analysis of the material parameters. The determination of thermal parameters is an important method for characterizing materials. Thermal diffusivity is an important thermo-physical parameter which is of direct importance in heat flow studies as it determines the rate of periodic or transient heat propagation through a medium. Its determination is often necessary because of its controlling effect and common occurrence in thermal conduction problems. Based on these lines, we have carried out the thermal diffusivity measurements on the thin films of the systems Ge-Se and As-Se using PBD technique.

The thesis is divided into seven chapters. In the first chapter, an overall

review of amorphous semiconductors is given. It includes an introduction to amorphous semiconductors, followed by a brief discussion on the important structural models proposed for chalcogenide glasses and their electrical, optical and thermal properties. The chapter also gives a brief description of the Physics of thin films, ion implantation and photothermal effects.

Chapter 2 presents a description of the experimental techniques used in the present investigation. A brief description of the experimental set up of a photothermal deflection spectrometer is given, followed by the illustration of the design and fabrication of a vacuum coating unit which is employed for the preparation of thin films in our studies. The chapter includes the details of the preparation of the samples and also the description of the UV-Vis-NIR spectrophotometer used for the optical characterisation of the thin film samples under investigation.

Chapter 3 gives the details of the preparation and optical characterisation of the thin film samples of the systems Ge_xSe_{100-x} ($5 \leq x \leq 40$) and As_xSe_{100-x} ($10 \leq x \leq 60$). The absorption and transmission spectra of these samples are analysed. From the absorption spectra, the optical band gaps are determined. The variation of optical band gap of these samples with composition is investigated and the observed behaviour is explained on the basis of various models. A simple calculation following traditional methods has been employed for deducing the refractive indices of the samples from the

v

fringe pattern of the transmission spectra and the variation of refractive index with wavelength for different compositions of the samples is also investigated.

Chapter 4 deals with the employment of the subgap optical absorption measurement by PDS to characterize the defects, amorphization and annealing behaviour in silicon implanted with B^+ ions. The effect of ion dose, implantation temperature and thermal annealing on the subgap absorption are investigated. The chapter also presents the profiles of the ion range and vacancy distribution obtained by the TRIM simulation. The changes induced in the band edge slopes and in the subgap features of the spectra are described. The various stages of formation, quenching and annealing of divacancies are monitored as a function of implantation conditions and annealing cycles. The chapter also describes the investigations on the structural modifications and defect evolution under annealing in amorphous material produced by implantation.

Chapter 5 outlines the results of thermal diffusivity measurements of the thin film samples of the glass systems Ge_xSe_{100-x} ($5 \leq x \leq 40$) and As_xSe_{100-x} ($10 \leq x \leq 60$) using PBD technique. For this, we have adopted the phase method, making use of the tangential (parallel) component of deflection signal based on the skimming configuration, where the probe beam grazes the sample surface. The experiment has been performed for two different modulation frequencies and the results are verified using the amplitude method. The variation of thermal diffusivity with composition for the two sets of samples has also been

investigated and explained on the basis of structural changes taking place in the glass network with the change in composition.

Chapter 6 reports the results of the optical absorption measurements by PDS in nitrogen implanted thin film samples of Ge-Se and As-Se systems. The profiles of the ion range and vacancy distribution are obtained by the TRIM simulation. The variations of optical band gap and inverse logarithmic slope with implantation for the different compositions of the samples are investigated and are explained on the basis of structural changes taking place in the network due to ion bombardment.

Chapter 7 is the concluding chapter incorporating overall conclusions of the work presented in earlier chapters. Further scopes for the work that can be done in this direction on other chalcogenide glass systems are also discussed.

Chapter 1

Introduction

In this chapter, an overall review of amorphous semiconductors is given. It includes an introduction to amorphous semiconductors, followed by a brief discussion on the important structural models proposed for chalcogenide glasses and their electrical, optical and thermal properties. The chapter also gives a brief description of the Physics of thin films, ion implantation and photothermal effects.

PART A: Review of the Physics of Amorphous Semiconductors

1.1. Introductory remarks

The study of non-crystalline materials is an active area of research in solid state physics mainly because of the enormous and diverse applications of these materials like xerography, memory and switching elements and energy conversion devices such as solar cells. Research in the area of amorphous semiconductors gained momentum in 1950's with the discovery by Kolomiets that chalcogenide glasses behave like intrinsic semiconductors and that their electrical conductivity can't be increased by adding dopants [1]. The studies by Spear [2] on the drift mobility in amorphous selenium and by Tauc [3] on amorphous germanium made important contributions to this area. Ovshinsky's report [4] on the switching and memory effects in chalcogenide glasses was indeed a turning point which attracted several scientists to the field of amorphous materials. The studies in the field of amorphous silicon [5,6] and the discovery that the electronic properties of a-Si and a-Ge could be controlled by substitutional doping [7] were milestones in the development in the field of amorphous materials. This led to the fabrication of cheap and efficient photovoltaic and photothermal devices, thin film a-Si p-n junctions and thin film transistors [8-10], all of which played a remarkable role in making the field of amorphous semiconductors, a frontier area of research.

2

In contrast to the remarkable progress that was made in the understanding of the physics of crystalline solids, a proper theoretical understanding of disordered systems remained largely undeveloped because of the mathematical complexity in dealing with non-periodic systems. An important theoretical study on this subject was presented by Anderson [11] who interpreted the transport properties of amorphous semiconductors based on the concept of localization, according to which, if we think of the center of the band of states produced by a simple Hamiltonian, disorder in the network can localize the eigen states. Above a critical strength of disorder, all states are localized. Later, several workers solved the problems associated with disordered systems, by exploiting scaling theories and the ideas of localization and percolation [12-14]. Pioneering theoretical work by Mott [15] also made significant contribution to our understanding of the amorphous state.

1.2. Classification and Preparation of amorphous semiconductors

1.2.1. Classification of amorphous semiconductors

Amorphous semiconductors can be divided into two groups as tetrahedrally co-ordinated silicon like materials and chalcogenide glasses. Chalcogenide glasses contain one or more of the chalcogen elements of the sixth group of the periodic table, sulphur, selenium and tellurium [16]. The distinction between these two classes is based on chemical considerations. The four-fold co-ordination in Si leads to symmetrical bonding and the formation of rigid structures. Thus, a continuous random network with tetrahedral bonds can

3

be constructed with negligible density deficit and little possibility for local reorganization of atoms. On the other hand, two fold co-ordination in Se is very asymmetrical and the structure gives rise to greater degree of flexibility. A major distinction comes from the fact that in Se, but not in Si, the uppermost valence band is formed from non bonding lone pair p electrons.

The class to which a particular material belongs can be determined by some of the distinctive properties such as the presence of paramagnetic centers, photoinduced ESR, luminescence, variable range hopping conduction etc. The Si type materials have large density of dangling bonds. The density of paramagnetic centres is found to be between 10^{19} and 10^{20} cm^{-3}, while in Se and chalcogenide glasses, it is negligible. The creation of paramagnetic centres by irradiation is possible in chalcogenides, while no such photoinduced effect is found in Si-type materials. At low temperatures, Si-type materials show variable range hopping conduction with a $T^{-1/4}$ dependence amongst localized states at the Fermi level, while in the case of Se and chalcogenides, the conductivity is temperature activated in an Arrhenius manner with an energy close to one half the optical band gap.

1.2.2. Methods of preparation of amorphous semiconductors

Amorphous materials are usually prepared by two different methods, i.e; vapour condensation technique and melt quenching technique. The former method is employed for the preparation of thin films, while the latter gives rise to bulk glasses, having a well defined glass transition temperature.

Chalcogenide glasses can be prepared in the form of bulk glasses by melt quenching technique and also in the form of thin films, but the Si-type materials can't be prepared in the glassy form. They are usually prepared in the thin film form by deposition on a substrate [17]. Several techniques such as vacuum evaporation, sputtering, electrolytic deposition, glow discharge deposition, chemical vapour deposition etc. are employed for preparing thin films of these materials.

The reasons for the dependence on different techniques for the preparation of the two classes of materials can be explained by the nature of chemical bonds and is based on the mismatch between constraints and the number of degrees of freedom in three dimensions and in the flexibility required to accommodate the mismatch. The flexibility of covalent bond angles is least for the tetrahedrally coordinated Si-type materials and largest for the two-fold coordinated Se-type materials. Therefore, covalent random network of a-Si is highly over constrained and no longer forms glass. Therefore, based on the average co-ordination number $<r>$, a classification of non-crystalline solids can be made as shown in Fig.1.1. According to this, glasses are restricted to $3 \geq <r> \geq 2$. Materials with higher connectivity i.e; $4 \geq <r> \geq 3$ are over constrained amorphous while those with $<r> < 2$ are underconstrained amorphous. The average coordination $<r> = 4$ separates non-crystalline metals from semiconductors or insulators.

1.2.3. Glass formation

The process of glass formation has always received continued attention. A

```
←——Metals ——→ ←——     Semiconductors      ——→
                         · or insulators

                  Overcon                  underconstrained
                  strained                 amorphous
                  amor-        glass
                  phous
```

6   5   4   3   2   1

Average coordination number
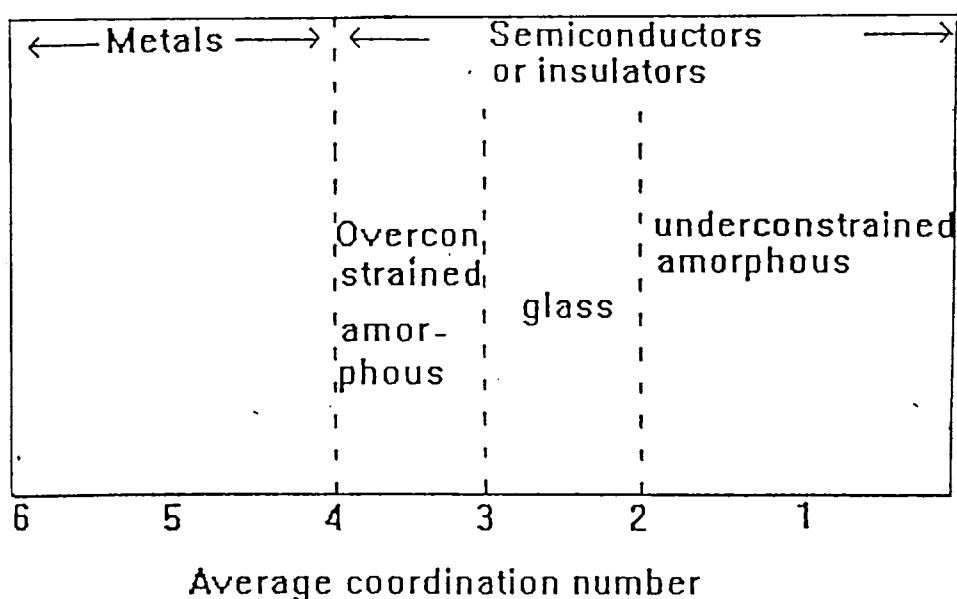
Fig.1.1. Classification of non-crystalline solids based on the average co-ordination number

glass is a material formed by cooling from the normal liquid state. The glass transition may be defined as a transition which involves no discontinuous change in first order thermodynamic properties such as volume, heat content and entropy, but does involve a progressive increase in the derivative second order thermodynamic properties like specific heat capacity and thermal expansivity [18]. The temperature at which second order properties change from 'liquid-like' to 'solid-like'is known as the glass transition temperature (T_g).

At glass transition, the diffusive motion is arrested so that the liquid is locked into a particular cell of phase space which corresponds to the atomic configuration fixed in the glass. Glass transitions are usually characterized by the phenomenological value T_g and by a width ΔT_g of the glass transition region around T_g. In this region, the diffusive motion of the

6

melt begins to freeze in, before a glassy structure is achieved with viscosity values typical of solids (10^{14} Nsm^{-2}). Both T_g and ΔT_g depend on the cooling rate [16].
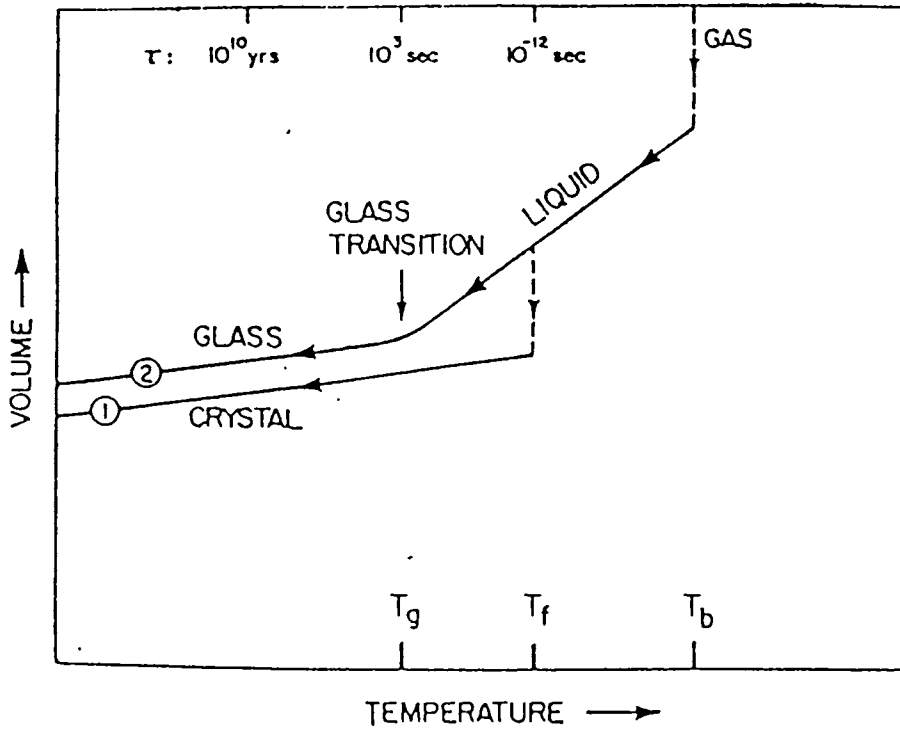
Fig.1.2. The two cooling paths by which an assembly of atoms can condense into the solid state. Route(1) to the crystalline state and route (2) to the amorphous state

Nearly all materials can, if cooled fast enough and far enough, be prepared as amorphous solids. A given material may solidify through either of the two routes indicated in Fig.1.2. As soon as the temperature of the liquid is lowered to T_f, it may take route (1) to the solid state and crystallize. In the temperature interval between T_f and T_g, the liquid is referred to as 'undercooled' or 'supercooled'. If this temperature can be taken below T_g before crystallization has had time to occur, the undercooled liquid solidifies

7

as glass and remains in this form essentially indefinitely. Hence, the formation of amorphous state is essentially a process bypassing crystallization [19].

Inorder to bypass crystallization process, the liquid should be cooled very fast. Cooling rates of the order of 10^2 Ks^{-1} to 10^6 Ks^{-1} are required to freeze the disorder. For pure metals, cooling rates of the order of 10^9 Ks^{-1} are required [19]. Details of glass formation and related processes are discussed in many review articles [20-24].

1.3. Structural models

Amorphous materials have a disordered structure and lack long range periodicity of constituent atoms. However, the disorder is not complete on the atomic scale. Short range order, similar to that present in crystalline materials is present also in these disordered materials. Hence, the structural modelling of amorphous semiconductors is done by the repetition of one or more basic molecular units in a way that can't be topologically identified with any known crystalline structure or with any infinite periodic array, but the atomic order within a molecular unit might be similar within small bond angle distortions in both crystalline and amorphous phases. This reveals the importance of short range order in describing the structural behaviour of a non-periodic network.

Determination of the atomic structure of amorphous materials is a non-trivial task because the uncertainty in the determination is compounded by the fact that the structure of a non-crystalline material, at both

microscopic and macroscopic levels, often depends on the method of preparation. Also, more than one experimental structural probe must be used to obtain a complete picture of the structural arrangement in an amorphous solid.

Structural models play an important role in the determination of the structure of amorphous materials. There have been many discussions on the types of structural models that can be used to describe amorphous solids [25]. The main point in describing the structure is the specification of the short range order and the topological rules which determine it. Given the short range order with three parameters, i.e; the number of bonds Z, the bond length a and the bond angle θ having well determined values in a narrow range, it is possible to construct a model for the amorphous structure. Such models are called random networks. The first model of an amorphous solid by a random network of atoms was proposed by Zachariasen in 1932 [26], with near perfect short range order, with particular reference to oxide glasses.

1.3.1. Network models (CRN and COCN)

CRN (Covalent Random Network) model assumes a definite short range order as each of its atoms fulfill its chemical valence requirements according to Mott's 8-n rule [27], where n is the number of valence electrons of the particular atom. The underlying principle of this model is that a closed outer shell of eight electrons is the most stable structure. Small variations introduced in bond lengths and bond angles lead to disorder in the glassy

matrix. The major source of randomness is the variation in bond angles, while the variation in bond length is much less and are within 1% to those found in crystals. For two fold co-ordinated chalcogens, the flexibility of covalent bond angles is largest compared to tetrahedrally coordinated Si type materials. CRN model generates the amorphous structure without taking into account structural defects such as dangling bonds and voids. This model is found to be suitable for glasses such as a-Si, SiO_2 and As_2Se_3.

The random covalent network (RCN) [28-30] and chemically ordered covalent network (COCN) models describe the structure of chalcogenide glasses more appreciably. These two models differ only in their approach to the distribution of bonds. The network structure for a binary alloy system A_xB_{1-x}, where A and B are two different atomic species and x is a normalized concentration variable can be specified by four factors such as the local coordination of A and B, the distribution of bond types A-A, A-B and B-B, the specification of characteristic local molecular environments and the topological rules for the interconnection of the molecular building units [31,32]. The RCN model gives a statistical estimation of the fraction of the different types of bonds, by considering each type to be equally probable, neglecting the relative bond energies. Hence, A-A, A-B and B-B bonds are equally preferred at all compositions except at x=0 and x=1. On the other hand, the COCN model emphasizes the relative bond energies and is based on the assumption that heteropolar A-B bonds are preferred to A-A and B-B bonds at all compositions. A completely chemically ordered phase thus occurs at a composition $X_C = Z_A/Z_A+Z_B$ at which only A-B bonds are

present, where Z_A and Z_B are the co-ordinations of A and B atoms respectively. For compositions defined by $1 > x > X_C$, the alloys contain A-B and B-B bonds, whereas for $X_C > x > 0$, the alloys contain A-B and A-A bonds. $GeSe_2$ and As_2Se_3 are the critical compositions in Ge_xSe_{1-x} and As_xSe_{1-x} systems respectively [30]. At critical compositions of many systems, anomalous variations are observed in their physical properties [33-36].

1.3.2. Mechanical threshold model

Phillips proposed a simple dynamical model [37] for network glasses based on topological considerations, which attempts to relate the glass forming tendency with the number of constraints acting on the network. According to Phillip's theory [37,38,39], the glass structure is maximally optimised when the number of degrees of freedom (N_d) available for the atoms equals the number of interatomic force field constraints (N_c) in the network at a critical average co-ordination number $Z = Z_c$. When the average co-ordination number $Z < Z_c$, the network is underconstrained and tends to disintegrate into non-polymerized fragments. When $Z > Z_c$, the network is overconstrained.

Later, Thorpe extended Phillip's model to predict the elastic behaviour of covalent glasses in terms of the average number of constaints in the system [40-43]. This model treats the network glass as made up of elastically soft or floppy and elastically rigid regions. For low average co-ordination number Z, the network is a polymeric glass ($N_d > N_c$) in which the rigid regions are isolated. As the average co-ordination number is increased, the rigid regions grow in size and get interconnected. At $Z = Z_c$ or $N_d = N_c$, the

network transforms into a completely rigid glassy structure. This transition

is known as 'rigidity percolation'. The rigid regions start percolating and at

Z_{av} = 2.41, the system transforms into a mechanically rigid amorphous solid.

This point at which the threshold occurs is termed the mechanical or rigidity

percolation threshold.

According to Phillips - Thorpe model, the number of constraints can

be written as,

$$N_c = \frac{Z}{2} + (2Z-3)$$
                                              (1.1)

where Z/2 is the bond stretching constraints and (2Z-3) is the bond bending

constraints for the system with Z bonds. For a 3D system, a structural phase

transition at the critical value Z = 2.41 is predicted at which the network

changes from a floppy to rigid type, as shown in Fig.1.3, thereby possessing

mechanically optimized structures.

Tanaka modified the Phillips and Thorpe model by considering that

the interactions in chalcogenide glasses is not confined to short range scales

and is extended to medium range scale also. This is evidenced by the

characteristic features in the composition dependence of various properties

of chalcogenide alloys exhibiting characteristic signatures at the average co-

ordination <Z> = 2.67, which can be connected to the formation of stable

layer structures in the network [44]. Considering the planar medium range

configurations, the number of angular constraints gets reduced to (Z-1)

instead of (2Z-3). Hence, eqn.(1.1) gets modified to

$$N_d = \frac{Z}{2} + (Z-1)$$
                                              (1.2)

predicting a composition driven structural phase transition at Z = 2.67. 2D

layered structures are fully evolved at this critical value and for higher

values of Z, there is a transition to a 3D network due to the increase in the

number of cross linked sites.
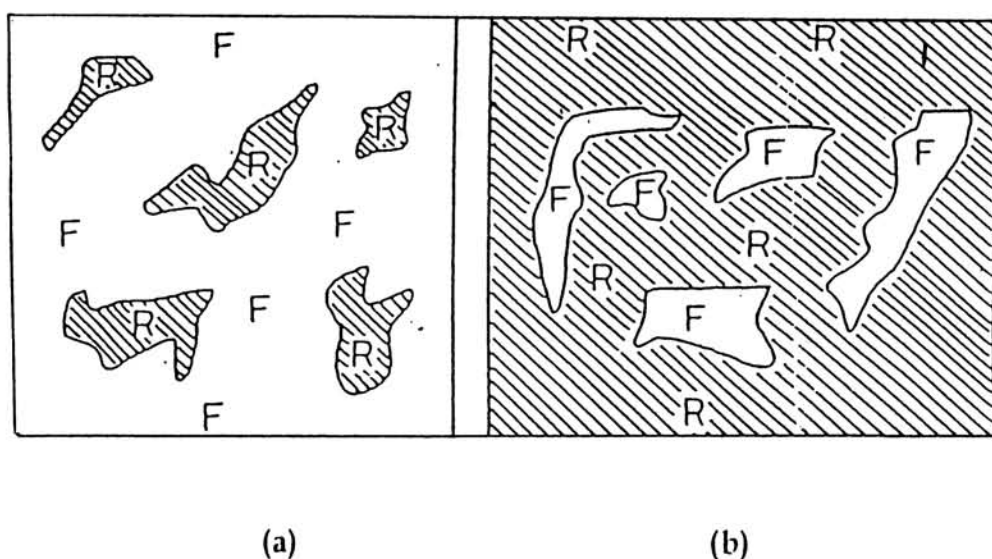

(a)   (b)

Fig.1.3. Rigid and floppy regions in the network of (a) polymeric glass
and (b) amorphous solid

1.4. Band models

1.4.1. General characteristics

A model for the electronic structure of a material is essential for the proper

interpretation of experimental data of its electrical transport properties. The

main features of the energy distribution of the density of electronic states

N(E) of crystalline semiconductors are the sharp structure in the valence and

conduction bands, and the abrupt terminations at the valence band

maximum and the conduction band minimum. The sharp edges in the

density of states produce a well defined forbidden energy gap. Within the

band, the states are extended which means that the wave function occupies

the entire volume. The specific features of the band structure are consequences of the perfect short-range and long-range order of the crystal. In an amorphous solid, the long-range order is lacking, whereas the short-range order is only slightly modified. The concept of density of states is also applicable to non-cystalline solids.

The first effort in generalizing the theory of crystalline semiconductors to amorphous ones was done by Mott [45,15]. Based on Anderson's theory [11], Mott argued that the spatial fluctuations in the potential caused by the configurational disorder in amorphous materials may lead to the formation of localized states, which do not occupy all the different energies in the band, but form a tail above and below the normal band. Mott postulated further that there should be a sharp boundary between the energy ranges of extended and localized states. The states are localized in the sense that an electron placed in a region will not diffuse at zero temperature to other regions with corresponding potential fluctuations. There is a particular density of electronic states above which the states in amorphous solid become extended, leading to the existence of critical energies in each band where a sharp jump in mobility from negligible values to finite ones takes place. These critical energies play the same role that band edges play in crystalline solids and are called the mobility edges. The energy difference between the mobility edges of the valence band and those of the conduction band is called the mobility gap.

Several models were proposed for the band structure of amorphous semiconductors, which were the same to the extent that they all used the

concept of localized states in the band tails, though opinions vary as to the extent of tailing.

1.4.2. Cohen-Fritzsche-Ovishnsky (CFO) model

The CFO model [46] is an extension of Mott's model. This model assumes that the tail states extend across the gap in a structureless distribution. This gradual decrease of the localized states destroys the sharpness of the conduction and valence band edges. The extensive tailing makes the conduction and valence band tails overlap in the midgap, leading to an appreciable density of states in the middle of the gap. A consequence of the band overlapping is that there are states in the valence band, ordinarily filled, that have higher energies than states in the conduction band that are ordinarily unfilled. A redistribution of the electrons must take place, forming negatively charged filled states in the conduction band tail and positively charged empty states in the valence band. This model therefore ensures self-compensation and pins the Fermi level close to the middle of the gap, as required by the electrical properties of these materials [47,48].

The CFO model was specifically proposed for the multicomponent chalcogenide glasses exhibiting switching properties. One of the major objections against the CFO model was the high transparency of the amorphous chalcogenides below a well defined absorption edge. This leads to the conclusion that the extent of tailing is only a few tenths of an electron volt in the gap [49]. It is now almost certain from different observations that the extent of tailing in chalcogenides is rather limited. The energy states as described by the CFO model are shown in Fig.1.4(a).

1.4.3. Davis and Mott (DM) model

According to this model [50-52], the tails of localized states should be rather narrow and should extend a few tenths of an electron volt into the forbidden gap. Davis and Mott propose furthermore the existence of a band of compensated levels near the middle of the gap, originating from defects in the random network, e.g., dangling bonds, vacancies etc. Fig.1.4(b) sketches the DM model, where E_c and E_v represent the energies which separate the ranges where the states are localized and extended. The centre band may be split into a donor and an acceptor band, which also pin the Fermi level [Fig.1.4(c)]. Mott suggested that at the transition from extended to localized states, the mobility drops by several orders of magnitude producing a mobility edge. The interval between the energies E_c and E_v acts as a pseudo gap and is defined as the mobility gap. Cohen [53] proposed a slightly different picture for the energy dependence of mobility. He suggested that there should not be an abrupt but rather a continuous drop of the mobility occurring in the extended states just inside the mobility edge.

Experimental evidence, mainly coming from luminescence, photoconductivity and drift mobility measurements has been found for the existence of various localized gap states, which are split off from the tail states and are located at well- defined energies in the gap. These states are associated with defect centers, the nature of which is always not known.

The DM model explains three processes leading to conduction in amorphous semiconductors, in different temperature regions. At very low temperatures, conduction can occur by thermally assisted tunneling between
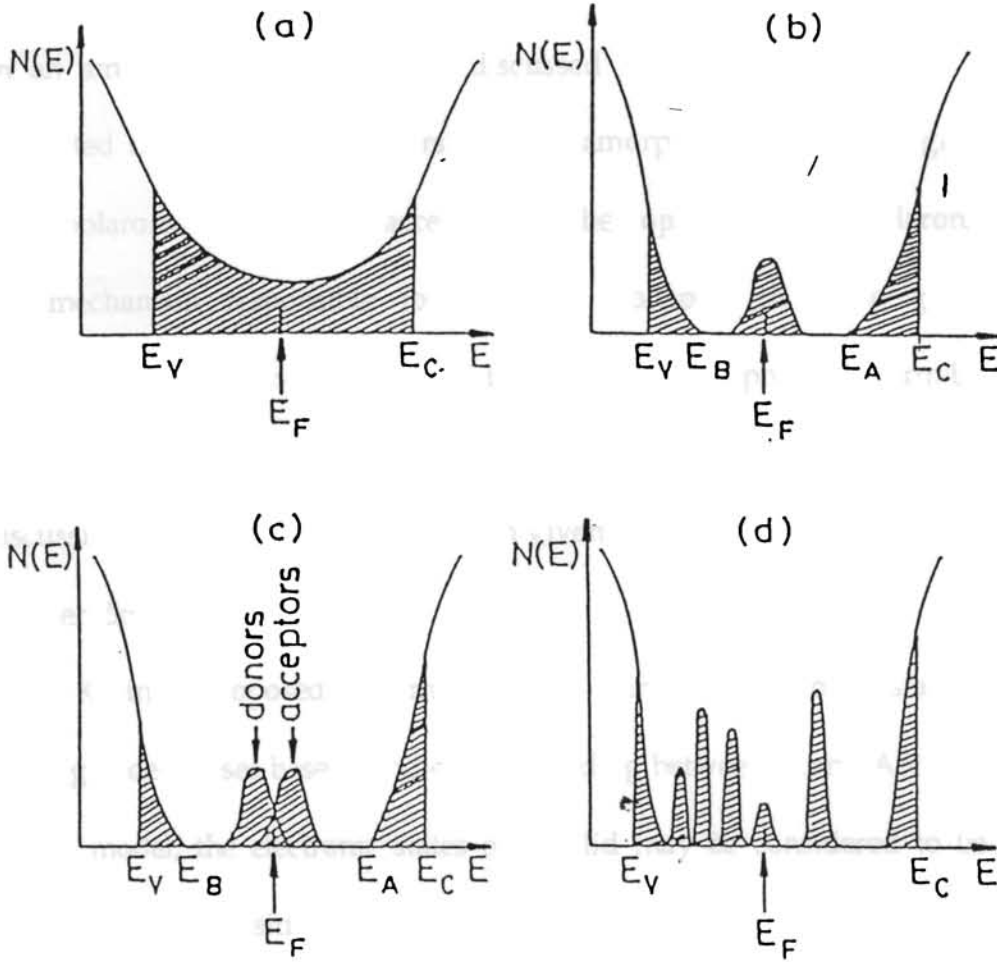

Fig.1.4. Schematic density of states for amorphous semiconductors (a) CFO model (b) Davis-Mott model showing a band of compensated levels near the middle of the gap (c) modified Davis-Mott model (d) the 'real' glass with defect states

states at the Fermi level. At higher temperatures, charge carriers are excited into the localized states of the band tails; carriers in these localized states can take part in the electric charge transport only by hopping. At still higher temperatures, carriers are excited across the mobility edge into the excited

states. Thus, it follows that electrical conductivity measurements over a wide temperature change are needed to study the electronic structure of amorphous semiconductors.

The role of lattice distortion in the presence of an extra charge carrier in an amorphous solid has been discussed in detail by Emin [54]. He suggested that the charge carriers in some amorphous materials might be small polarons. It is generally accepted that the hopping of small polarons is the mechanism responsible for electrical transport in oxide glasses. Physicists have increasingly adopted the chemical view point as a firm base to begin the analysis of the electronic structure of amorphous solids. Good discussions of this approach have been given by Mooser and Pearson [55], Kastner [56] and Adler [57].

Kastner proposed a simple model for the electronic states in chalcogenide glasses based on chemical bonding between atoms. According to this model, the electronic states of a solid may be considered to be a broadened superposition of the molecular orbial states of the constituent bonds. When any two atoms come close for their bonding electrons to interact, the energies of their states get shifted by the interaction. Thus, group IV elements (Si, Ge) have hybridized sp^3 orbitals which are split into bonding (σ) and antibonding (σ^*) states. In a solid, these molecular states are broadened into bands. In tetrahedral semiconductors, the bonding band forms the valence band and the antibonding band forms the conduction band. In group VI elements (Se, Te), the s states lie sufficiently deep in energy and are thus chemically inert. One of the three p orbitals is occupied

18

by two paired electrons of opposite spin, which are referred to as non-bonding or lone pair electrons and bonding is effected by the other two p orbitals, each occupied by one electron, so that chalcogens are found to be in two-fold co-ordination. In a solid, the lone pair (LP) electrons form a band near the original p state energy and σ and σ^* bands are split symmetrically with respect to this reference energy. The bonding band is no longer the valence band; this role is played by the LP band. For this reason, chalcogenide semiconductors are referred to. as "lone pair semiconductors"[56]. The bonding in Ge and Se are sketched in Fig.1.5.

1.5. Defect related models

1.5.1. Street and Mott model

Street and Mott [58], and Mott, Davis and Street 59] chose to apply the Anderson negative U_{eff} concept to specific defects in an otherwise fully connected network. Considering the two dangling bonds at the ends of the selenium chain, when they each contain a single electron, the defects are neutral and will be designated D^0. Transfer of an electron from one chain end to the other will lead to the creation of two charged defects D^+ and D^-. The model developed by Street and Mott assumes that the electron-phonon interaction makes electron pairing energetically favourable at defects, which when neutral (D^0) have orbitals containing one electron.

Thus, the reaction

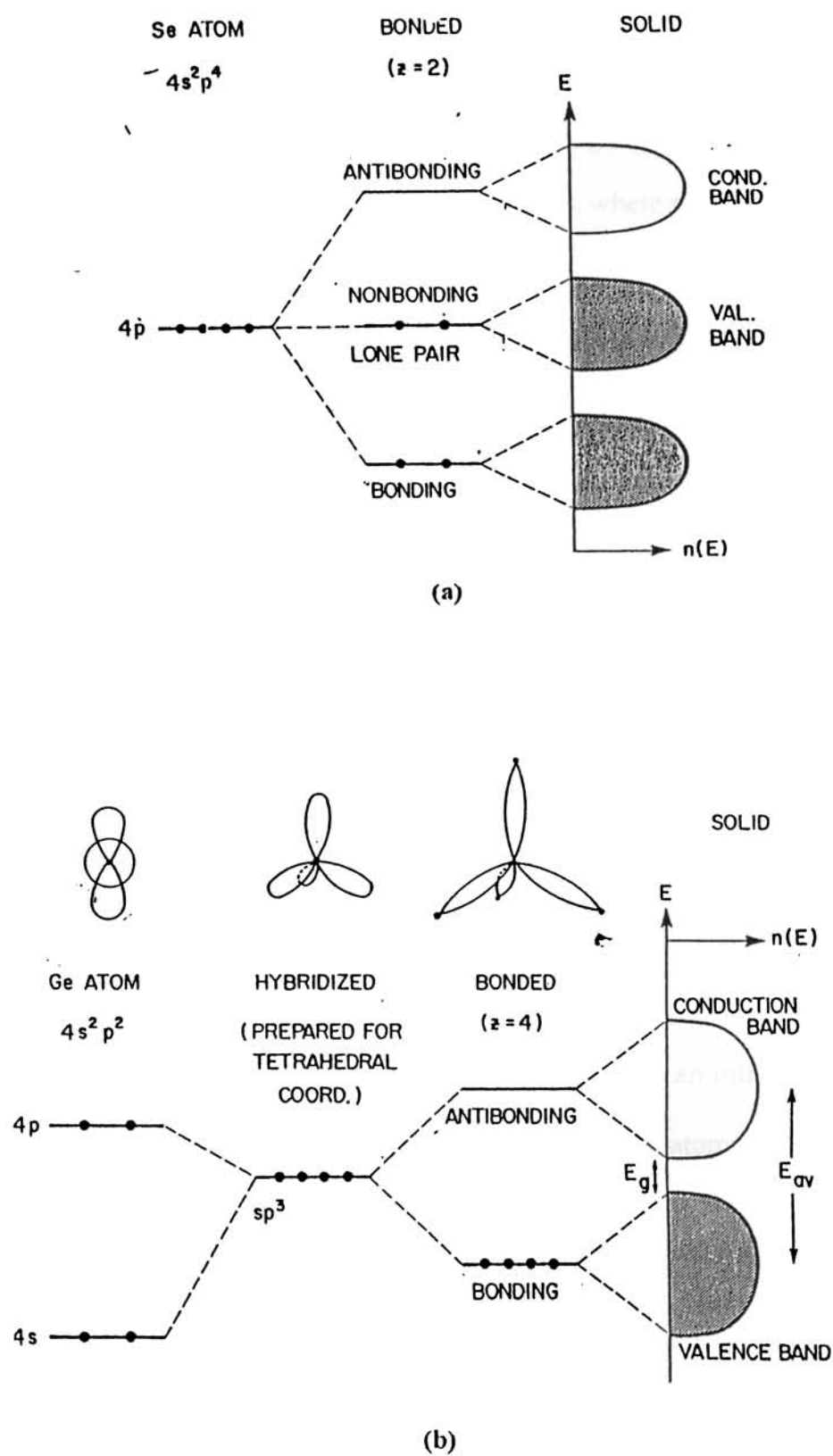$$2D^0 \rightarrow D^+ + D^- \tag{1.3}$$

(a)

(b)

Fig.1.5. Bonding schematic for the electronic structure of (a) solid selenium (b) a tetrahedrally coordinated covalent solid (crystalline or amorphous), illustrated for germanium

is exothermic. Here D^+ and D^- represent the defect when empty and when containing two electrons respectively.

According to this model, chalcogenide glasses contain $10^{18} - 10^{19}$ cm^{-3} dangling bonds. The bonds are point defects, where normal coordination is not satisfied due to the constraints of local topography. The major objection to this model is the assumption of high density of dangling bonds. Also the model doesn't explain why large negative U_{eff} characterizes chalcogenide glasses and is absent in tetrahedrally bonded amorphous materials [60].

1.5.2. KAF model

This model has been suggested by Kastner, Adler and Fritzsche [61]. They postulated the formation of valence - alternation pairs which need so little energy of formation that even crystals can't be grown without them. For a-Se, these defect states are singly and triply coordinated sites designated by Kastner as C_1^- and C_3^+. In a-As, the corresponding pairs of defects would be labelled P_2^- and P_4^+, where P species is a pnictide atom. The existence of these spin-paired, charged defect states is related in an intimate way to the nonbonding or lone pair electrons of group V and VI atoms.

1.6. Properties of amorphous semiconductors

1.6.1. Structural properties

For an amorphous solid, the essential aspect with which its structure differs with respect to that of a crystalline solid is the absence of long-range order. There is no translational periodicity. Its structure is developed by the repetition of one or more basic molecular units that can't be identified

topologically with any known crystalline structure. Amorphous materials do not possess the long-range translational order (periodicity) characteristic of a crystal but have short range order of a few lattice spacings. There are many discussions on the type of structural models that can be used to explain amorphous solids [58]. Even with the restraints imposed by individual atoms and short range order, there is an infinite number of allowed structures for an amorphous material.

The experimental methods used for the detailed investigation of the structure of amorphous materials fall under four major categories, ie; diffraction methods, vibrational spectroscopy, photo emission spectroscopy and hyperfine interactions [62-65]. The RDF of amorphous semiconductors give evidence for short range and medium range orders. EXAFS helps to probe the local structure of each type of atom separately. IR absorption, Raman scattering, X-ray and UV photoemission techniques are very useful in structural studies. Hyperfine interaction techniques include NMR, quadrupole resonance, Mossbauer effect etc. Differential thermal analysis provides information about changes in structure with variation of temperature [66].

1.6.2. Electrical properties

For amorphous semiconductors, there is a band of localized states which exists near the centre of the band gap. These localized states arise from specific defect characteristics of the material like dangling bonds, interstitials etc., which depend on the conditions of sample preparation and subsequent

annealing treatments. In amorphous semiconductors which may contain a high concentration of defects and consequently have a high density of states in the gap, electron transport can take place via such defect states, and the magnitude of this defect-controlled conductivity may greatly exceed that due to conventional band conduction. Moreover, the temperature dependence of conduction can have a distinct form, easily distinguishable from the simple activated behaviour characteristic of band conduction.

Davis and Mott model [50-52] predicts three regions of the d.c. conductivity of amorphous semiconductors as follows (i) conduction in extended states (ii) conduction in band tails and (iii) conduction in localized states at Fermi energy E_F.

Conductivity in extended states is characterized by large mobility which decreases sharply at the mobility edge. The variation of conductivity is given by [67]

$$\sigma = \sigma_0 \exp\left[-\left(\frac{E_C - E_F}{kT}\right)\right],$$ (1.4)

where the pre- exponential factor σ_0 is given by

$$\sigma_0 = eN(E_C)kT\mu_C$$ (1.5)

Here N (E_c) is the density of states at the mobility edge E_c, and μ_c is the mobility. Electrons at and above E_c can move freely, while electrons below it can move through activated hopping [68]. Mobility in this region is of the order 10 cm^2 V^{-1} S^{-1}.

Conduction via band tails takes place by exchange of energy with a phonon. If the current is carried mainly by holes and conduction is by hopping, then conductivity is given by

$$\sigma = \sigma_1 \exp\left\{ \frac{-E_F - E_B + \Delta W_1}{kT} \right\} \tag{1.6}$$

where ΔW_1 is the activation energy for hopping and E_B is the energy at the band edge. σ_1 is expected to be less than σ_o by a factor of 10^2 to 10^4.

In the third region (conduction in localized states), carriers move between states located at E_F via phonon assisted tunneling process, which is analogous to impurity conduction observed in heavily doped and highly compensated semiconductors at low temperatures. Conductivity in this region is given by

$$\sigma_1 = \sigma_2 \exp\left\{ \frac{-\Delta W_2}{kT} \right\} \tag{1.7}$$

where $\sigma_2 < \sigma_1$ and ΔW_2 is the hopping energy. As temperature is lowered, and the carriers tunnel to more distant cites, conductivity behaves as,

$$\ln \sigma = A - \frac{B}{T^{1/4}} \tag{1.8}$$

This variable range hopping at low temperatures is one of the interesting properties of amorphous semiconductors. As one goes from extended to localized states, mobility decreases by a factor of 10^3. This drop in mobility is called the mobility shoulder. The three mechanisms for charge transport that contribute to d.c current can also contribute to a.c conductivity. Measurement of thermo electric power in amorphous chalcogenides have shown them to be p type in majority of cases. But, in

contradiction to this, Hall coefficient has been exhibited as n-type for chalcogenide glasses. This has been explained by the theory of Friedman [62].

1.6.3. Thermal properties

At low temperatures, amorphous materials exhibit a markedly different behaviour from their crystalline counterparts in phonon related properties such as specific heat capacity, thermal conductivity and acoustic absorption [68,69]. At low temperatures, thermal conductivity decreases slowly with decreasing temperature. Thermal conductivity is weakly temperature dependent near 10K showing a plateau region and a T^2 dependence at temperatures below 10K. The magnitude of the temperature dependence appear to depend on the amorphous structure of the material rather than chemical composition. Hence the thermal transport below 10 K is provided by phonons [70]. Acoustic and dielectric absorption in amorphous solids is strongly enhanced at low temperatures.

1.6.4. Optical properties

Optical absorption in amorphous semiconductors can be separated into three regions [71] with absorption coefficients $\beta \geq 10^4$ cm^{-1}, 1cm^{-1} $< \beta < 10^4$ cm^{-1} and $\beta \leq 1$ cm^{-1}, referred to as the high absorption region C, the exponential part B which extends over four orders of magnitude of β and the weak absorption tail A respectively as shown in Fig.1.6.

The regions B and C arise due to transitions within a fully coordinated system perturbed by defects, while the region A arises due to

transitions involving the defect states directly. The absorption edge has a defect induced tail at lower energies, an exponential region at intermediate energies and a power law region at higher energies.

In the high absorption region, the frequency dependence of the absorption coefficient is governed by a power law of the type

$$\beta E = B\ (E-E_g)^p, \qquad\qquad\dots\dots\dots(1.9)$$

where p = 2 for amorphous semiconductors, assuming parabolic bands, B is a constant and E_g is the optical band gap. Thus, a plot of $(\beta E)^{1/2}$ versus E yields a straight line, which when extrapolated to E for which $\beta^{1/2} \to 0$ gives the optical energy gap E_g.
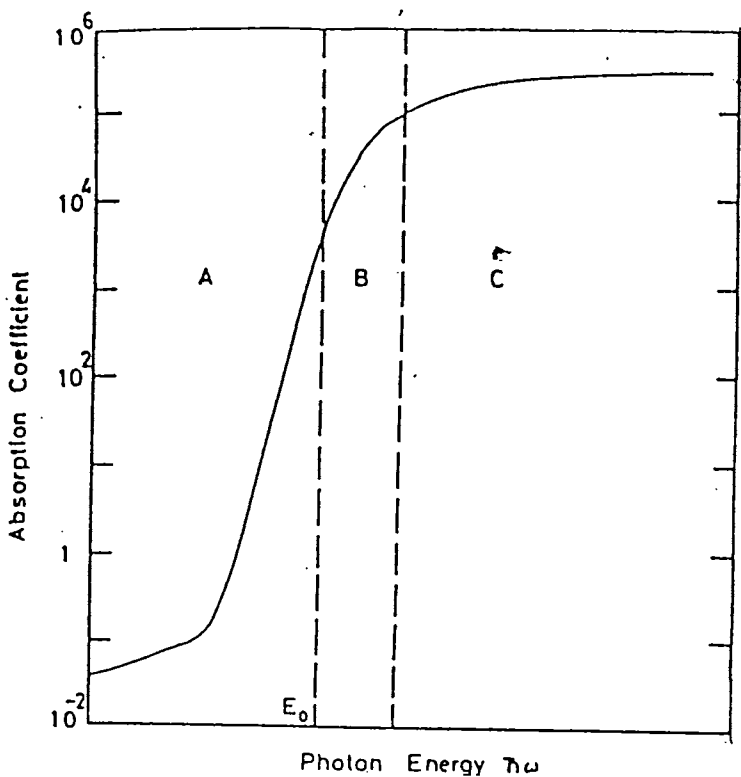

Fig.1.6. Schematic representation of the absorption spectrum of amorphous semiconductors showing three different regions A,B and C

The exponential region of the absorption edge is associated with intrinsic disorder in amorphous semiconductors in the intermediate range of absorption coefficient from 1 cm^{-1} (or less) to about 10^4 cm^{-1} in which the absorption constant is described by the formula

$$\beta E = Constant. \exp(E/E_c) \qquad (1.10)$$

where E_c is the energy characterising the slope. The exponential tail is due to disorder induced potential fluctuations [72,73] and strong electron-phonon interaction [74]. In the weak absorption tail region below the exponential part, the shape is found to depend on the preparation, purity and thermal history of the material [69]. The mobility gap in many amorphous semiconductors corresponds to a photon energy at which the optical absorption coefficient has a value of approximately 10^4 cm^{-1}.

1.7. Chalcogenide glasses

Chalcogenide glasses form an important class of materials and are recognized as a group of materials which always contain one or more of the chalcogen elements, S, Se or Te in conjunction with more electropositive elements , most commonly As and Ge, but also Bi, Sb, P, Si, Sn, Pb, B, Al, Ga, In, Ti, Ag, Lanthanides and Na. These glasses have a disordered structure and lack long-range periodicity of constituent atoms, but short-range order similar to that present in crystalline materials is present also in these disordered materials.

Chalcogenide glasses exhibit several interesting physical properties different from that of tetrahedrally coordinated amorphous semiconductors

like a-Si. The two important aspects contributing to these differences are the network flexibility in chalcogenides arising out of the relatively lower co-ordination and the nature of the co ordination defects. The two fold co-ordination present in the structure enables chalcogenides to cover a wide range of compositions, with physical properties varying appreciably even among samples of the same material. This composition dependent tunability of properties is the greatest advantage of these glasses, which helps designing of materials for specific requirements.

In chalcogenide glasses, conduction is predominantly by carriers hopping between localized states at the band edges. The d.c. conductivity of most of these glasses at room temperature follows the relation

$$\sigma = C \exp(-E/kT) \tag{1.11}$$

The thermoelectric power of chalcogenide glasses are normally positive indicating that they are p-type conductors.

1.8. Applications of amorphous semiconductors

Amorphous materials have widespread applications in electronic, electrochemical, optical and magnetic areas of modern technology. Many amorphous semiconductors are used as passive and active elements in electronic devices [75,76]. The different applications include fabrication of window glass, fiber optic wave guides for communications networks, computer-memory elements, solar cells, thin film transistors, transformer cores and in xerography. Amorphous materials are used in the fabrication of solid-state batteries, electrochemical sensors and electrochromic optical devices [77,78].

28

The immense applications of amorphous chalcogenides are related to their photoconducting property. Photoconducting materials find applications in vidicons, image intensifiers, light operated relays, switches etc. They are employed as IR filters and other IR optical elements. The phenomenon of electrical switching in amorphous materials is exploited by their application as computer memory elements. Switching materials find applications in electrical power control also.

PART B: Thin Films, Ion Implantation and Photothermal Effects

1.9. The Physics of Thin Films

1.9.1. Introduction

Two dimensional materials created by the process of condensation of atoms, molecules or ions are called thin films. A thin film may arbitrarily be defined as a solid layer having a thickness varying from a few A^0 to about 10µm or so. Thin films have got unique properties significantly different from the corresponding bulk materials because of their small thickness, large surface-to-volume ratios and unique physical structures which are direct consequences of the growth processes.

The characteristic features of thin films can be drastically modified to obtain the desired physical characteristics. These features form the basis of the phenomenal rise in thin film researches and their extensive applications in the diverse fields of electronics, optics, space science, air crafts, defense and other industries. These investigations have led to numerous inventions

in the form of active devices and passive components, piezo-electric devices, micro-miniaturisation of power supply, rectification and amplification, sensor elements, storage of solar energy, magnetic memories, superconducting films, interference filters, reflecting and antireflection coatings and many others. The present developmental trend is towards newer types of devices, monolithic and hybrid circuits, FET, switching devices, cryogenic applications, high density memory systems for computers etc. Further, because of compactness, better performance and reliability coupled with the low cost of production and low package weight, thin film devices and components are preferred over their bulk counterparts.

Film properties are sensitive not only to their structures but also to many other parameters including their thickness, especially in the thin film regions. Hence, a stringent control of the latter is imperative for reproducible electronic, dielectric, optical and other properties. Some of the factors which determine the properties of a film are the following *viz.* rate of deposition, substrate temperature, environmental conditions, residual gas pressure in the system, purity of the material to be deposited, inhomogeneity of the film, structural and compositional variations of the film etc., some of which have been actually observed [79-81]. It is also a common experience that a film may contain many growth defects or imperfections [82-85] such as lattice defects, stacking faults, twinning, disorders in atomic arrangement, dislocations, grain boundaries and various other defects. Surface states of a film also play a dominant role in modifying electrical and other properties.

1.9.2. Preparative techniques of thin films

Thin films can be prepared from a variety of materials such as metals, semiconductors, insulators or dielectrics and for this purpose, various preparative techniques have also been developed [17, 86-90], which in general are (a) thermal deposition in vacuo by resistive heating, electron beam gun , laser gun evaporation etc. from suitable sources, (b) sputtering of cathode materials in presence of inert or active gases either at low or medium pressures, (c) chemical vapour deposition (CVD) by pyrolysis, dissociations, reactions in vapour phase, (d) chemical deposition from solutions including electro-deposition, anodical oxidation, chemical reaction etc. The primary requirement for the methods (a) and (b) is a high vacuum deposition system at a pressure of about 10^{-5} T or less. In methods (c) and (d), a high vacuum is not an essential condition. The choice of a preparative technique is, however guided by several factors particularly the melting point of the charge, its stability, desired purity, characteristics of deposits etc.

1.9.3. Thermal evaporation in vacuo

Thermal deposition is the most widely used method for the preparation of thin films. The method is comparatively simple and is adopted for the deposition of metals, alloys and also many compounds. The process of film formation by evaporation consists of several physical stages.

(1) transformation of the material to be deposited into the gaseous state

(2) transfer of atoms / molecules from the evaporation source to the

substrate

31

(3) deposition of these particles on the substrate

(4) rearrangement or modifications of their bindings on the surface of the

substrate

The quality and characteristics of the deposit will depend on the rate of deposition, substrate temperature, ambient pressure etc. During evaporation, a fraction of the vapour atoms will be scattered due to collision with the ambient gas atoms. Pressures lower than 10^{-4} T are necessary to ensure a straight line path for most of the emitted vapour atoms.

In the method of resistive heating, the material to be evaporated is heated in a resistively heated filament or boat made of refractory metals like W, Mo, Ta or Nb. The choice of a particular refractory metal as a heating source depends on the materials to be evaporated. In the process of thermal evaporation, a little amount of charge is put into the filament or boat and a current is slowly passed through the source and gradually increased so that the melt forms a bead or a layer over the heating source. Usually a shutter is placed in between the heating source and the substrate, which is removed only when appropriate deposition conditions are established, then the deposition on the substrate starts. When the required film thickness is obtained, the shutter is brought to the original position so as to cut off further deposition.

Vacuum deposition of thin films was first carried out by Nahrwold in 1887. Evaporated thin films find industrial usages for an increasing number of purposes such as front surface mirrors, interference filters, sun glasses,

decorative coatings, in the manufacture of CRT, in solar cells and in semiconductor hetero-junction lasers.

1.10. Ion Implantation in Semiconductors

1.10.1. Introduction

When a substrate is bombarded by a beam of energetic ions, it will not only lose some of its own ions by sputtering but will also retain some of the incident ions. The incident ions that are retained are said to have been implanted, and the technique of using an energetic ion beam to introduce ions into a substrate is called ion implantation.

Ion implantation in semiconductors has received attention in several rather different contexts. Semiconductor physicists and device engineers are interested in the implantation process because it provides a new doping technique with several potential advantages over more conventional doping methods. Ion implantation is a superb method for modifying surface properties of materials since it offers accurate control of dopant composition and structural modification at any selected temperature. Materials scientists are interested in the electrical properties of ion-implanted semiconductors because they provide an important tool for studying solubility problems, diffusion processes and radiation damage effects. Nuclear scientists are interested in the ion distribution profile in an implanted semiconductor because it yields important information on the nature of the physical processes that occur when an energetic particle interacts with a crystalline target.

Historically, interest in ion-implanted semiconductors appears to have arisen first in the semiconductor device field. In 1952, Ohl [91] described improvements in the electrical characteristics of silicon point contact diodes that could be obtained by bombarding the surface of a silicon chip with various gases. The possible chemical effect that can be obtained from ion implantation seems to have been first described in a patent filed by Shockley in 1954 [92].

The first attempt to implant conventional dopants into semiconductors was that of Cussins [93], who in 1955 implanted a wide variety of ions, including boron into both single crystal and amorphous germanium targets. Active interest in ion implanted devices was later stimulated in 1963 when McCaldin and Widmer [94] described the preparation and properties of n-p junctions in which the n layer was formed by cesium implantation. This work clearly demonstrated the necessity of careful annealing to minimize the effect of radiation damage. Following this lead, Gibbons, Moll and Meyer [95] implanted rare earth elements into semiconductors in an effort to produce efficient electroluminescent materials and concurrent with the work of Mc Caldin and Widmer, King and his associates produced both improved nuclear radiation detectors [96] and solar cells [97].

The topics of research and development work on ion implantation in semiconductors that are receiving principal attention are 1) range-energy relations for the implanted ions, 2) crystalline sites and energy levels of the implanted ions, 3) structural and electrical effects of implantation-produced

damage and its annealing behaviour and 4) device fabrication and characterization.

1.10.2. Ion implanters

An ion implanter consists of the following major components: an ion source, an extracting and ion analyzing mechanism, an accelerating column, a scanning system and an end station [98]. The ion source contains the species to be implanted and an ionizing system to ionize the species. The source produces an ion beam with very small energy spread enabling high mass resolution. Ions are extracted from the source by a small accelerating voltage and then injected into the analyzer magnet. Fig.1.7 gives the schematic illustration of a medium current implanter.
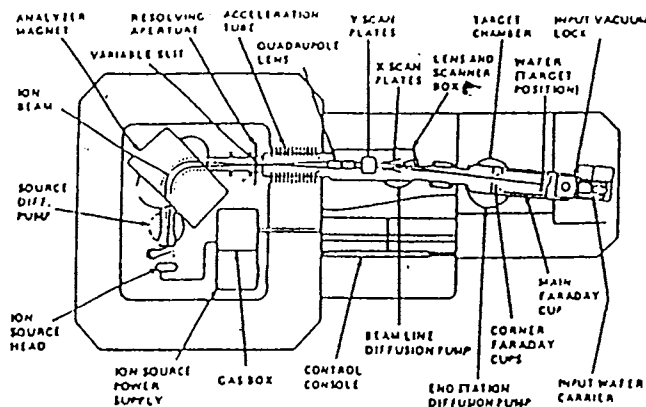
Fig.1.7. Schematic illustration of a medium current implanter with a maximum potential of 200kV and a current of 1mA.

A spatial separation of ions occurs due to the differences in the mass and charge. Only the selected ions are injected into the accelerating column, the others are stopped by the presence of suitable screens. The ions are

distributed uniformly over a target by electrical fields varying in the x and y

directions with a saw tooth or by a mechanical shift of the target.

Ion source is the most important component in industrial implanter.

All the sources [99,100] produce ions by means of a confined electrical

discharge which is sustained by the gas or vapour of the material to be

ionized. The species to be implanted must be present in the beam as charged

particles. The most common sources in ion implanters are positive ion

sources. In the case of tandom accelerators for high energy implants,

negative ion sources are needed. In tandem accelerators, negatively charged

ions are produced in the source, pre-accelerated to ~ 20 - $100KeV$, separated

by a magnet and injected into the acceleration tubes inside a tank.

Since high energy implantation is now becoming more and more

important for industrial application also, different technical solutions have

been adopted. Among these is the production of linear accelerators (LINAC)

for this aim. These are made by a series of cavities that in some cases are

polarized by a radio-frequency voltage. The linear accelerator is a resonance

device in which the electric component of a time varying rf electromagnetic

acts on charged particles to produce acceleration.

1.10.3. Range distribution

Ions hitting a target penetrate inside, lose their kinetic energy through

collisions with the nuclei and with the electrons of the material and finally

come to rest. The distribution of the implanted ions depends on several

parameters such as the ion mass and energy, the target mass and the beam

direction with respect to the main axes or planes in the case of a single

crystal target as the silicon wafer. The total distance which an ion of mass M_1

travels in coming to rest in a target of atoms of mass M_2 is the range R and is

shown in Fig 1.8.

The distance along the axis of incidence is called the projected range

R_p and the net distance travelled along the axis perpendicular to that

of incidence is called the perpendicular distance $R_\perp$. Because of ion

scattering, the total path R is greater than R_p and the relationship [101]

between R and R_p for low energy ions is given by Eq.1.12.
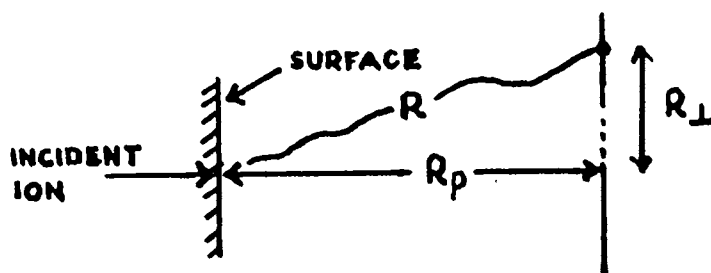
Fig.1.8. Range R, projected range R_p, and perpendicular distance $R_\perp$ for a
single ion incident on a target

$$R = \left[1 + \frac{M_2}{3M_1} \right]$$ (1.12)

The number of collisions experienced by an ion per unit path length and the

energy lost per collision are random variables, i.e; all the ions of a given type

and having the same incident energy will not have the same range. Rather,

there will be a distribution of stopping points in space which is described by

a range distribution function. R and R_p are the mean values and the standard

deviation, or straggle in the projected range is ΔR_p.

The range distribution is of course of first importance for applications of ion implantation to semiconductor device design and fabrication. In a typical case, the target material and ion to be implanted are known and we want to know what range distribution we can expect for a given beam energy, or perhaps how the beam energy should be modulated during the implantation to obtain a desired range distribution. If the target is amorphous, the range distribution will depend primarily on the energy, mass and atomic number of the incoming ions, the mass and atomic number of the target atoms, the density of the target, the temperature of the target during the implantation and the ion dose rate. If the target is a single crystal, the range distribution will also depend sensitively on the orientation of the crystal with respect to the ion beam, the surface condition of the crystal, and its past history.

The two major forms of energy loss that must be included in the development of range-energy relations that are appropriate for ion implantation conditions are (1) interactions of the ion with the electrons in the solid [102] and (2) collisions of the ion with the nuclei of the target. These two forms of energy loss are independent of each other. Thus, for a single incident projectile, the average rate of energy loss with distance can be written as the sum as given below.

$$-\frac{dE}{dx} = N[S_n(E) + S_e(E)] \qquad (1.13)$$

where E = the energy of the particle at a point x along its path,

$S_n(E)$ = the nuclear stopping power,

$S_e(E)$ = the electronic stopping power,

N = the average number of target atoms per unit volume.

Eq.(1.13) can be integrated to give the total distance R that a projectile of

initial energy E_0 will travel before coming to rest.

$$R = \int_0^R dx = \frac{1}{N} \int_0^{E_0} \frac{dE}{S_n(E) + S_e(E)} \tag{1.14}$$

The distance R is called the average total range and is a useful quantity for

making sample estimates of the average penetration depths of ions in

amorphous targets.

1.10.4. Damage production and annealing

An ion implanted into a target with an initial energy E_0 will ultimately come

to rest, losing its energy in a series of collisions with the atoms and electrons

of the target. Both of these energy-loss mechanisms are important in

determining the range of the ion, but only the atomic or nuclear collisions

can transfer enough energy to target atoms to produce radiation damage.

Furthermore, if the target is crystalline, the target atoms will be bound to

their lattice positions with a certain energy so that collisions will produce

damage only when the energy transferred by the projectile to a target atom

exceeds its displacement threshold energy E_d.

Collisions in which the energy transferred to a target atom, say E is

greater than E_d will displace that atom from its lattice site, thus producing

damage within the crystal. The displaced target atom may then be treated as a secondary projectile of energy $E - E_d$, which too will be brought to rest through a series of nuclear and electronic stopping events. In the course of its trajectory, the secondary projectile may have sufficiently energetic interactions with other target atoms to produce further displacements and a second generation of recoiling target atoms. Thus, the production of damage is a cascade process in which the incident projectile is simply the primary damage – producing particle. The various events are represented qualitatively by Fig.1.9, where the track of the incident projectile serves as a tree trunk with branches representing the trajectories of displaced target atoms. The envelope of all these displacements is referred to as a "damage cluster", which will have a size and character that depends on a large number of factors, including the mass of the incident ion and its energy, the mass of the target atom, and the temperature of the target.

A typical cross section of an implanted sample, if analyzed by transmission electron microscopy, reveals a variety of extended defects, amorphous zones, stacking faults, dislocation loops, twins, clusters etc. The visibility is limited to effects of dimensions above 1-2 nm. Point defects like interstitials, vacancies and small clusters can't be detected. The two basic types of intrinsic point defects are vacancies (V) and self interstitials (I) shown in Fig.1.10. In semiconductors, point defects often introduce electronic states in the band gap and can exist in different electronic configurations. A vacancy in Si can be either neutral or negatively or positively charged. Also point defects form complexes among themselves,

like divacancy V-V. From the point of view of ion implantation, perhaps the most important simple defect in silicon is the divacancy.

The E.S.R experiments indicate that the crystalline Si lattice can accommodate only a limited density of defects which may not be exceeded without inducing serious structural changes in the irradiated material. When the irradiation starts, vacancy-type defects are introduced into the crystalline lattice in growing numbers upto a critical level at which amorphization sets in. When the crystalline lattice has reached a critical state of damage, further irradiation causes the material to relax to the amorphous state.

For conditions of practical importance in ion implantation, the radiation damage produced by the injected ions is severe, and the crystal must be carefully annealed if the chemical effects of the implanted ions are to dominate the residual damage. Both the type and the amount of crystalline damage determine the annealing mechanisms that can operate, and therefore the annealing temperatures and times that must be used to return the crystal to a relatively undamaged state.
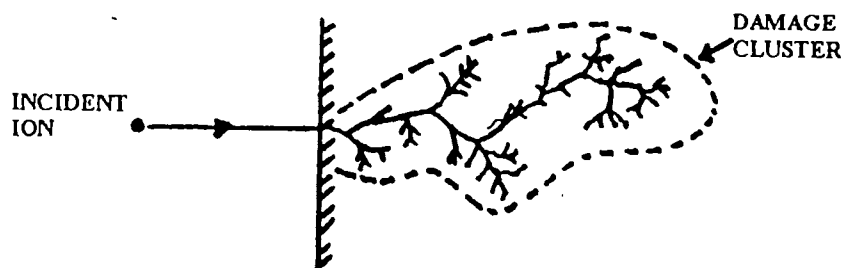
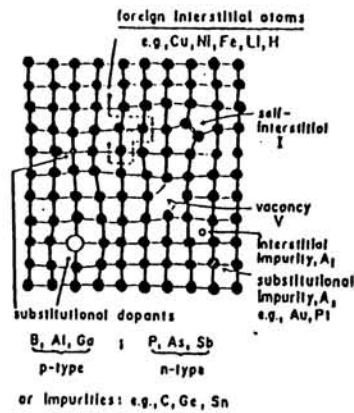Fig.1.9. Illustrating the formation of a damage cluster by collision cascades

Fig.1.10. The various types of intrinsic and extrinsic point defects in an elemental semiconductor crystal such as silicon

1.10.5. Computer simulations

Ion range and damage distribution predictions are essential for ion implantation and a wide variety of computer simulations have been developed. An inherent problem is that the generation of a realistic simulation of all the events that occur as an energetic ion travels into a target requires a detailed knowledge of the types of interaction between the ion and the target electrons and atoms. Ideally, the simulation should take account of the simultaneous motion of all the displaced atoms as well as the incoming ion and follow their motion until the material relaxes down to thermal energies. It should also include the possibility of annealing of the damage, sputtering from the surface and the formation of new compounds. Including all these possibilities is indeed a trivial task and so, the simulations normally only address the problem of range distributions and initial damage creation. Many of the simulations are well refined and widely used , some have been upgraded continuously over the years from their original versions, eg. The

TRIM (Transport of Ions in Matter) of Biersack and Haggmark [103] has been modified both by Biersack and his co-workers.

Computer simulations of ion ranges have been reviewed at regular intervals and excellent items have been included by Biersack and Ziegler [104], Ziegler [105] and Webb [106]. The problems of sputtering and computer simulation in general include other books or reviews such as those of Behrisch and Wittmaack [107], Harrison [108,109], Robinson [110], Anderson [111], Frenkel [112] and Eckstein [113].

There are two classes of simulation approach. These are to either simulate the trajectories of the ions and displaced lattice ions or to use analytical expressions to encompass overall transport properties. Trajectory simulation is conceptually simple in that one specifies an ion of a given energy, spatial position and direction, defines an interaction potential and computes the results of the collision on the primary and struck ion. Programs based on the TRIM code are widely used for amorphous targets and low ion doses; they include interaction potentials based on a very large experimental data base and hence offer reliable predictions of the impurity distributions. TRIM follows a large number of individual ion trajectories in a target, each trajectory beginning with a given position, direction and energy of the ion. It is then followed through a sequence of collisions with the target atoms. It has been shown that the program calculations are consistent with the experimental results in most common cases. Variants of TRIM include codes for sputtering, high dose damage estimates and formation of

new compounds. A different binary-type code which is designed for crystalline targets is named MARLOWE.

Existing simulation programs are widely used and offer moderately accurate predictions of implanted ion ranges and initial damage distributions for amorphous targets. In all cases, there is a compromise between computer speed and accuracy.

1.11. Photothermal Effects

1.11.1. Introduction

Interaction of electromagnetic radiation with matter causes absorption, emission and inelastic scattering of light. Except for emission, absorbed energy results in production of several forms of energy like luminescence, photochemical energy, photoelectrical energy or heat (Fig.1.11). Heat can be produced promptly or at various time delays. This heating induces changes in the sample as well as in the surrounding medium. These changes are referred to as photothermal effects [114,115]. Although it may seem counterintuitive to pursue phenomena based on the transformation of energy to the most chaotic form, heat, these techniques have many advantages for applications in low absorption environments and in the domain of materials characterization and nondestructive testing.

The discovery of photothermal effects dates back to Graham Bell's observation in 1880, of the generation of acoustic waves in a sample resulting from the absorption of photons. Unfortunately, this technique found only a few applications due to non-availability of good light sources.

In 1968, there was an upsergence in its use, after the invention of laser sources. Photothermal effects are observed commonly in nature. A concrete example of the photothermal effect observed in nature is the optical mirage effect, which is one of the photothermal effects that have been exploited for physical and chemical analysis.

In short PT generation is an example of energy conversion and has in general three kinds of applications. a) PT material probing which do not cause any sample modification, b) PT material processing which causes the sample to change to another useful form and c) PT material destruction which makes the sample useless. Of the above three, it is the PT material probing that makes significant contribution to the field of science and technology. Photothermal material characterization relies on high sensitivity detection techniques to monitor the effects caused by PT material heating of a sample. The effects are illustrated in Fig.1.12. Most of the photothermal effects occur simultaneously. The choice of a suitable PT effect for detection depends on the nature of the sample and its environment, the light source used and the purpose of measurement.

Detection methods for the various photothermal effects are classified generally into two depending on whether the detection methods are applied to sample itself or to the surrounding media. The former one is the *direct detection* scheme and the latter is the *indirect detection* scheme. It is to be noted that all the PT detection schemes require a modulation in the excitation light. The modulation can be in the form of continuous train of

pulses at nearly 50% duty cycle (continuous modulated PT detection) or in

the form of short intense pulses (pulsed PT detection). The continuous

modulated PT detection is in the frequency domain (lock-in-detection) and

pulsed PT detection is in the time domain. Brief descriptions of the various

PT methods are given in Table1.1.

Temperature rise: Temperature rise can be directly measured using

thermocouples, thermistors, or pyroelectric detectors and is called *laser*

calorimetry or *optical calorimetry* or *photothermal calorimetry* [116,117]. Though

the observed temperature rise can be directly measured and can be related

to physical parameters like absorption coefficients, response and sensitivity
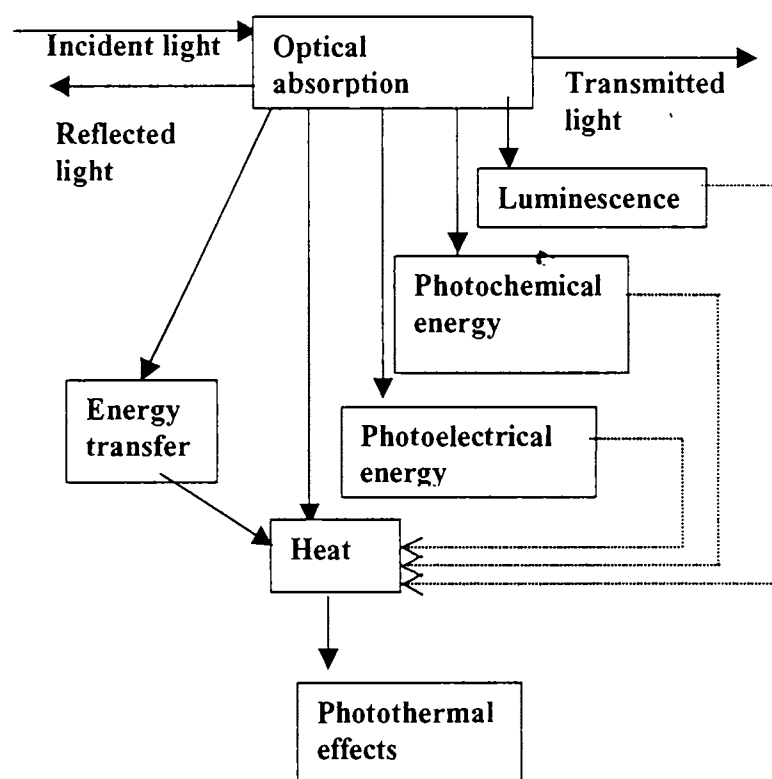
Fig.1.11. Block diagram indicating the consequences of optical absorption

leading to prompt or delayed heat production

is low. Moreover, heat leakage from the sample must be minimized by elaborate thermal isolation. However it was shown that fast rise time and high sensitivity for a thin film sample is possible if it is directly coated on to a thin film pyroelectric detector [118,119]. Heat produced within the solid due to the non-radiative de-excitation process can give rise to electrical signal in a pyroelectric thin film in contact with the sample and analysis of the dependence of the pyroelectric signal gives the optical, thermal and geometric parameters of the solid/pyroelectric system [120].

Pressure change: Another temperature dependent parameter exploited is the pressure change. Pressure variations or modulations resulting from the absorption of modulated light by the sample are referred to as *optoacoustic* or *photoacoustic* generation [121-123]. The pressure wave generated after light excitation contains contributions from various sources such as radiation pressure, electrostriction, thermoelastic expansion (by non radiative transition or thermal energy of chemical reaction), photoinduced volume change etc. The acoustic wave can be detected in the sample itself (direct photoacoustic detection) or it can be detected via coupling fluid medium adjacent to the sample (indirect photoacoustic detection).

Refractive index change: The majority of studies addressing the use of photothermal spectroscopy for chemical analysis have been based on the refractive index measurements. The refractive index change produced upon light absorption may be induced by the pressure wave, density change, a temperature change (by radiationless transition or chemical reaction), molecular alignment, vibration excitation, rotational excitation, electronic

excitation, concentration change, photoinduced volume change, creation of electric field (charge creation), clustering and so on. In transparent samples, the temperature dependent changes in refractive index of the sample itself are probed. For opaque samples, the temperature dependent changes in refractive index of the fluid that couples heat out of the sample are measured. Two types of refractive index gradient are produced -*Thermal RIG* and *Acoustic RIG*. The thermal RIG is produced by the decreased density of the medium caused by the local temperature rise, decays in time following

Photothermal effects	Detection methods (applicable to Sample S or adjacent fluid F)
1.Temperature rise	Laser Calorimetry (S or F)
2. Pressure change	Direct photoacoustic detection(S) Indirect photoacoustic detection (F)
3. Refractive index change (Thermal or acoustic)	Probe beam refraction (S or F) Probe beam diffraction (S or F) Other optical probes (S or F)
4. Surface deformation (Thermal or acoustic)	Probe beam deflection (S) Optical interference (S)
5.Thermal emission change	Photothermal radiometry (S)
6.Reflectivity/absorptivity change	Transient thermal reflectance (S) Transient piezo reflectance (S) Optical transmission monitoring (S) or (F)

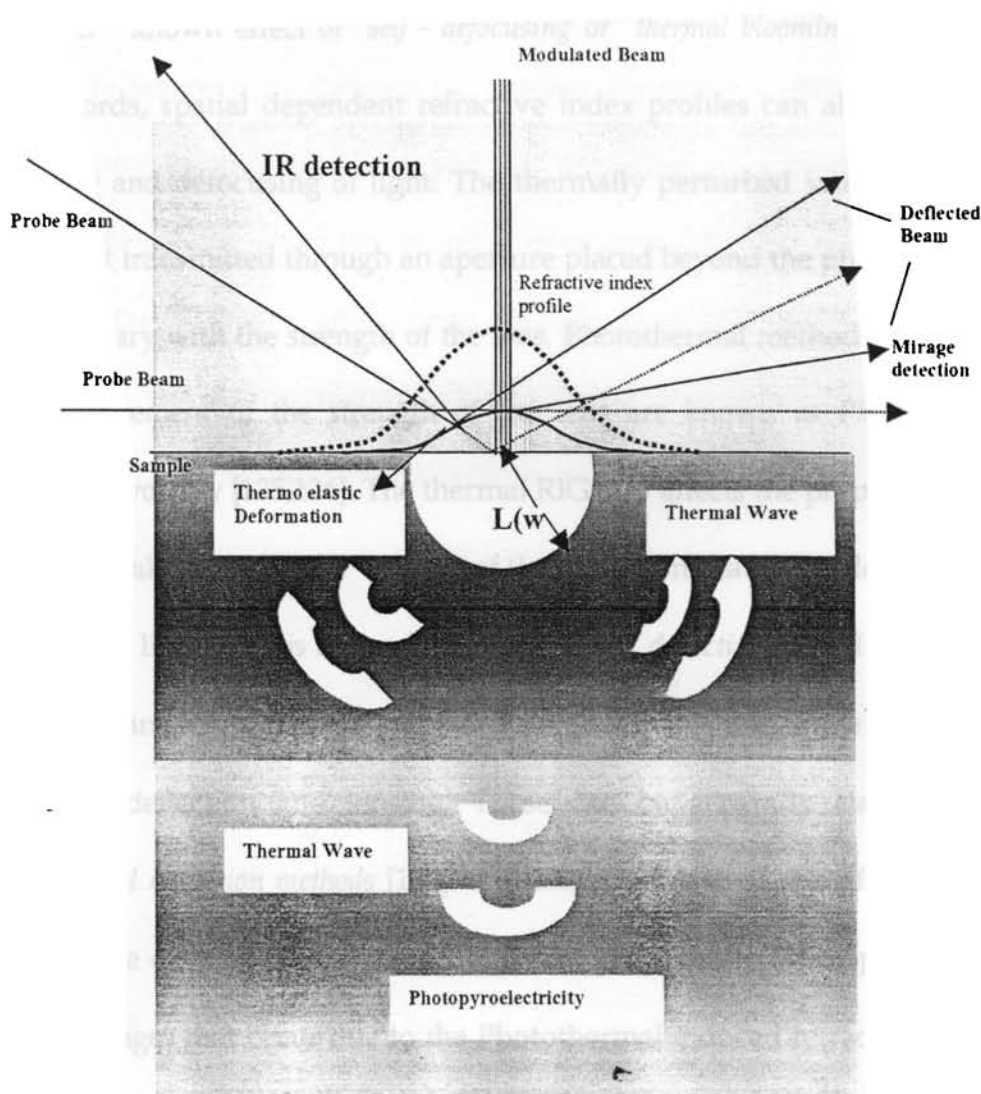Table 1.1. Descriptions of the various PT methods

Fig.1.12. Schematic of the various photothermal effects and the detection mechanisms

the diffusional decay of the temperature profile and remains near the initially optically excited region. The acoustic RIG is associated with the density fluctuation of the medium caused by the propagation of PA wave, decays in propagation distance following attenuation of the PA wave and travels at acoustic velocity away from initially optically excited region. The thermal RIG generated by the excitation beam affects the propagation of an optical beam in its vicinity, including its own propagation, resulting in

the well - known effect of *self - defocusing or thermal blooming* [124]. In other words, spatial dependent refractive index profiles can also result in focussing and defocusing of light. The thermally perturbed sample acts as lens. Light transmitted through an aperture placed beyond the photothermal lens will vary with the strength of the lens. Photothermal methods based on the measurement of the strength of the lens are known as *Photothermal lensing spectroscopy* [125,126]. The thermal RIG also affects the propagation of another weak beam in the vicinity of the excitation beam. The detection of bending of light path is utilized in *Photothermal deflection method* [127-131]. Some experimental apparatus measures a signal that is due to the combined effects of deflection and lensing. These can be generally classified as *Photothermal refraction methods* [132] and take advantage of the effects of the temperature distribution on the probe beam propagation. The optical path length changes that occur due to the Photothermal induced refractive index change can be measured with *interferometry*. A periodic refractive index modulation results in a volume phase diffraction grating. The grating will diffract light at an angle that meets requirements from Bragg's law. The amount of light diffracted is proportional to the refractive index change. The diffracted light is measured with a photoelectric detector. Methods used to measure spectroscopic signals based on volume phase grating formed by the photothermal heating are called *Photothermal diffraction spectroscopy* [133,134]. The various configurations dealing with the different measurements cited above are depicted in Fig.1.13 (a-e).

Surface deformation: Under steady state isobaric conditions, the density is related to temperature through the volume expansion coefficient. Though temperature dependent density changes are difficult to measure directly, these changes can affect the samples in several different ways. In solid samples, the density change causes changes in sample dimensions which give rise to two optical methods for monitoring temperature changes based on surface deformation. A homogeneous deformation displaces the surface of the sample. Interferometry can be used on reflective samples. Since small
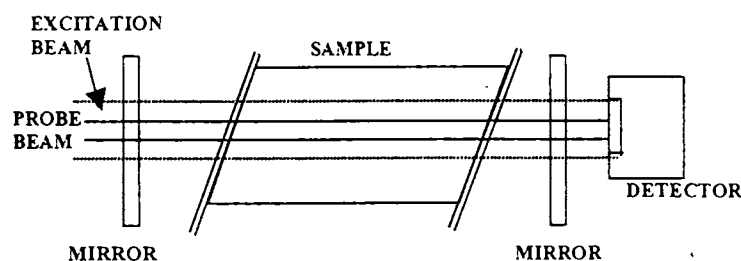
Fig.1.13(a). Interferometry
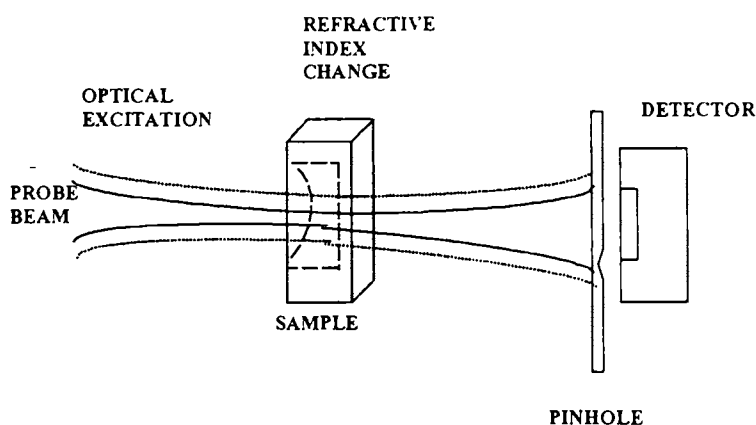
Fig. 1.13 (b). Thermal lensing

51
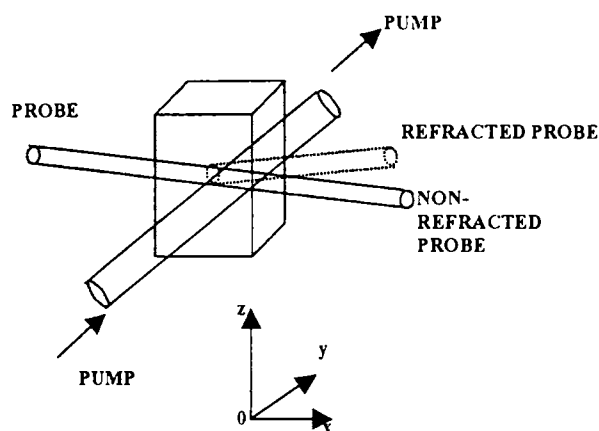
Fig.1.13 (c). Perpendicular probe beam deflection through the sample
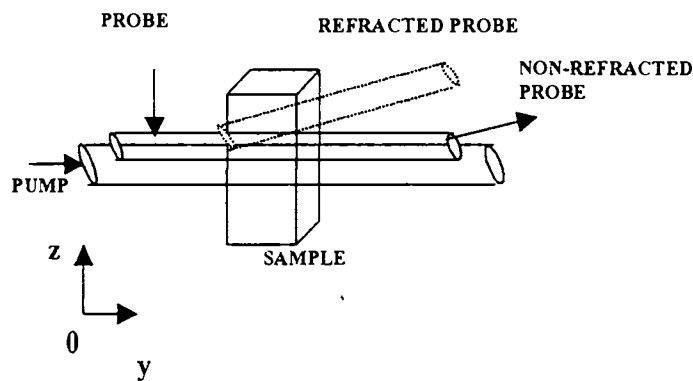
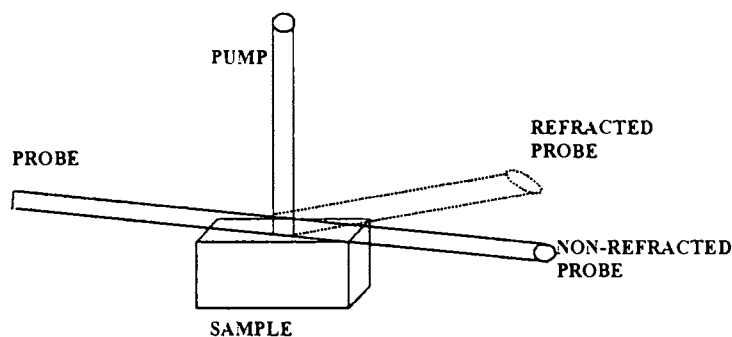**Fig.1.13 (d).** Parallel probe beam deflection

Fig.1.13 (e). Perpendicular probe beam deflection outside the sample surface (mirage effect)

displacements of the order of few parts per million of the wavelength of the probe beam light can be measured using interferometry, this method may be used for sensitive measurements. Spatially heterogeneous expansion (contraction) can also cause the surface angle to change. A probe beam reflected from the surface will change angle when heterogeneous expansion occurs. Measurement of probe beam angle gives rise to the method of PT surface displacement technique [135-137].

Infrared emission changes: Temperature changes can also be indirectly measured using methods, which monitor infrared emission since the thermal infrared emission is related to sample temperature. The method of photothermal radiometry [138] can be used to measure the infrared emission changes. Although not very sensitive, this method has great potential application in non-destructive material analysis and testing. Using infrared sensitive cameras, it can be used for imaging the thermal properties of large samples.

Other PT changes: Modulated PT heating of many types of metal or semiconductor samples causes modulated reflectivity changes [139] or transmission and scattering changes [140] that can be due to density change or the photoacoustic carrier generation at the surface. Transient thermal reflectance can be used to monitor thermal properties. PT heating can cause changes in absorptivity of the sample. Zapka and Tam have used probe beam absorption measurements to detect the change in the Boltzmann molecular population distribution due to PT heating of a gaseous sample [141].

- Photothermal signals depend on the thermodynamic and energy transfer properties of the sample. Temperature changes resulting from optical absorption are directly related to heat capacity and thermal conductivity. Since the thermal and optical properties are to be known to a high accuracy, absolute sample absorption measurements are difficult. Hence, the dependence on thermodynamic and energy transfer properties allows for the analysis of thermal structure of materials. Photothermal methods have been efficiently used for the measurement of acoustic velocities, thermal diffusion coefficients, sample temperature, bulk flow rates, phase transition, volume expansion coefficients and heterogeneous thermal conductivities in the solids [142-148].

Photothermal measurements are usually performed using laser light sources. There are two main reasons for this. One is the high spectral purity and power of the laser beam. For an excitation of a sample with a given absorption coefficient, the temperature change will be proportional to the optical power, in the case of continuous excitation or energy in the case of pulsed excitation. The photothermal signal is generally proportional to the temperature change. Thus, the greater the power or energy, the greater is the photothermal signal. Lasers can deliver high power or pulsed energies over very narrow optical bandwidths thereby enhancing the photothermal signals. The second reason is the spatial coherence. The temperature change is not only proportional to the optical power or energy, but also is inversely proportional to the volume over which light is absorbed since the heat capacity scales with the amount of substance. The spatial coherence

properties of the laser light also allow the light to be focussed to small, diffraction-limited volumes. The small volumes enhance the signal magnitude and allow the photothermal spectroscopy to be used in small volume sample analysis and allow for microscopic analysis of heterogeneous samples.

1.11.2. Photothermal Probe Beam Deflection (PBD) or Mirage Effect
[114,128-130,149-151]

The geometry for the mirage deflection is as shown in Fig.1.14. The propagation of the beam through the spatially varying index of refraction is given by

$$\frac{d}{ds}\left(n\ \frac{dr_0}{ds}\right) = \nabla_\perp n(r,t) \tag{1.15}$$

where r_0 is the perpendicular displacement of the beam from its original direction, n is the uniform index of refraction and $\nabla_\perp n(r,t)$ is the gradient of the index of refraction perpendicular to S (the ray path). This relation can be integrated over the ray path S

$$\frac{dr_0}{ds} = \frac{1}{n} \int_{path} \nabla_\perp n(r,t)ds \tag{1.16}$$

Since the deviation is small, one can get the expression of the deflection $\theta(t)$

$$\theta = \frac{dr_0}{ds} = \frac{1}{n}\frac{\partial n}{\partial T}\int \nabla_\perp T(r,t)ds \tag{1.17}$$

$$= \frac{1}{n}\frac{\partial n}{\partial T}\int_{-\infty}^{+\infty} \nabla T_s \times ds$$

In our case, the probe beam is propagating through the fluid along the x-direction. Hence, the probe deflects with components in x-y plane and z-x plane so that after calculating the vector product in the integrand of the above expression, we get the transverse (θ_t) and the normal (θ_n) components of the deflection, respectively.

$$\theta_n = -\frac{1}{n}\frac{\partial n}{\partial T}\int_{-\infty}^{+\infty}\frac{\partial T_g}{\partial z}dx\ \hat{j}$$ (1.18)

$$\theta_t = \frac{1}{n}\frac{\partial n}{\partial T}\int_{-\infty}^{+\infty}\sin\alpha\frac{\partial T_g}{\partial r}dx\ \hat{k}$$ (1.19)

θ_n and θ_t are the deflections normal and parallel to the sample surface.

1.11.3. Applications of Photothermal Effects

The photothermal phenomenon finds application in various areas of research. The high sensitivity of the PDS has led to applications for the analysis of low absorbance samples. The technique has been used to measure acoustic velocities, thermal diffusion coefficients, sample temperatures, bulk sample flow rates, specific heats, volume expansion coefficients, and heterogeneous thermal conductivities in solids. A technique namely thermal wave imaging allows nondestructive material inspection by measuring the rate of heat transfer in heterogeneous materials. A research group at the Hampton University has applied PDS to environmental monitoring. They are engaged in the development of the technique to measure pollutants in water or soil solution. Their approach is to measure weak absorption of pollutants using PDS and then compare the results with existing methods. They have also applied PDS to measure small

56

concentrations of iron and phosphate in water solutions. Photothermal spectroscopy is also characterized as a trace analysis method.
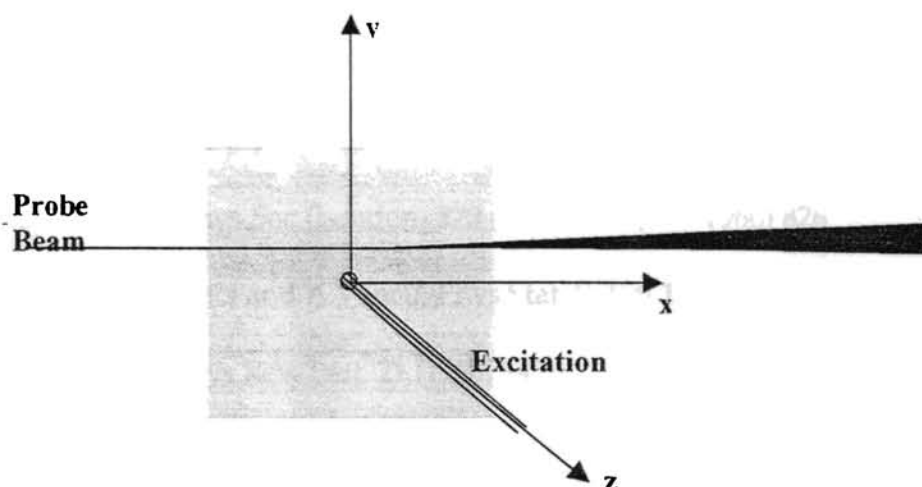

Fig.1.14. Geometry for 'mirage' deflection. The probe beam is along x direction and excitation beam or pump beam is along z direction.

PDS is now used as a powerful characterization technique in many laboratories in the World to study the disorder induced absorption, effect of doping etc. One of the major groups making significant contributions to the development of the technique is at the University of Rome, who has applied the technique for the study of ion implanted semiconductors [152]. A few laboratories in India like I I T Kanpur, IACS Calcutta, TIFR Bombay and NPL New Delhi use PDS technique for measuring the optical absorption in semiconducting materials; but most of these works are related to the absorption measurement in a-Si:H and related materials and much effort has not been made to enhance the measurement capability.

References

1. B.T.Kolomiets, Proc.Int.Conf.on Semiconductor Physics, Prague 1960

   (Czechoslovak Academy of Sciences,1961) p.884; Phys.Stat.Solidi **7**

   (1964),359,713

2. W.E.spear, Proc.Phys.Soc.(London) **870** (1957) 1139; **76** (1960) 826

3. J.Tauc, R.Grigorovici and A.Vancu, Phys.Stat. Solidi **15** (1966) 267

4. S.R.Ovshinsky, Phys.Rev. Lett. **21** (1968) 1450

5. H.F.Sterling and R.C.G.Swann, Solid State Electron.**8** (1965) 653

6. R.C.Chittick, J.H.Alexander and H.F.Sterling , J.Electrochem. Soc. **116**

   (1969) 77

7.W.E.Spear and P.G.Le Comber, Solid State Commun. **17** (1975)

   1193;Phil.Mag.**33** (1976) 935

8.W.E.Spear, P.G.Le Comber S.Kinmond and M.H.Brodsky,

   Appl.Phys.Lett.**28** (1976) 105

9. C.R.Wronski, D.E.carlson and R.E.Daniel, Appl. Phys. Lett. **29** (1976) **602**

10.W.E.Spear and P.G.Le Comber, "The Physics of Hydrogenated

   Amorphous Silicon I", ed: J.D.Joannopaulos and G.Lucovsky

   (Springer Verlag, Berlin, 1984) p.63

11. P.W.Anderson, Phys.Rev.**109** (1958) 1492

12. E.Abrahams, P.W.Anderson, D.C.Licciardello and T.V.Ramakrishnan,

   Phys.Rev.lett., **42** (1979) 673

13. P.A.Lee and T.V.Ramakrishnan, Rev.Mod.Phys., **57** (1985) 287

14. D.J.Thouless, "III Condensed Matter", ed: L.R.Ballian, R.maynard and

G.Toulose (North-Holland, Amsterdam,1978) p.5

15. N.F.Mott and E.A.Davis, "Electronic Processes in Non-Crystalline

Materials" (Clarendon press, 1971)

16. R.Zallen, "The Physics of Amorphous Solids" (John Wiley,

New York, 1983)

17. K.L.Chopra, "Thin Film Phenomena" (Mc Graw- Hill, New York,1969)

18. G.O.Jones, "Glass", 2nd ed.,(Chapman and Hall, London, 1971)

19. D.Turnbull, Contemp.Phys.10 (1969) 473

20. E.S.R.Gopal, Proc.30 Years Commemoration, Saha Institute of Nuclear

Physics, Calcutta, India (1983) 37

21. D.Turnbull, "Undercooled Alloy Phases" ed: E.W.Collings and C.C.Koch,

Metallurgical Soc.Warrendale PA (1986) 3

22. F.Yonezawa, "Solid State Physics" ed. H.Ehrenreich and D.Turnbull, 45

(Academic Press Inc.)199

23. R.B.Schwarz and W.L.Johnson, Phys.Rev.Lett. 51(1983) 415

24. C.C.Koch, O.B.Cavin, C.G.Mc Kamey and J.O.Scarbough, Appl. Phys.Lett

43 (1983) 1017

25. A.C.Write and A.J.Leadbetter, Phys.Chem.Glass **17** (1976)122

26. W.H.Zachariasen, J.Am.Chem.Soc. **54** (1932) 3841

27. N.F.Mott, Adv.in Phys. **16** (1967) 49

28. G.Lucovsky and T.M.Hayes " Amorphous Semiconductors",

ed. M.H.Brodsky (Springer Verlag, Berlin, 1985)

29. R.M.White, J.Non-Cryst.Solids **16** (1974) 387

30. J.C.Phillips, Phys.Today (February, 1982) 27

31. G.Lucovsky, F.L.Galeener, R.H.Geils, R.C.Keezer, "The Structure of Non-Crystalline Materials", ed: by P.H.Gaskell (Taylor and Francis, London, 1977) 127

32. G.Lucovsky, R.J.Nemanich, F.L.Galeener, "Amorphous and Liquid Semiconductors", ed: by W.E.spear (G.G.Stevenson, Dundee, 1979) 130

33. A.Srinivasan, K.N.Madhusoodanan, E.S.R. Gopal and J.Philip, Phys.Rev.B **45** (1992) 8112

34. A.Giridhar, P.S.L. Narasimham and S.Mahadevan, J.Non-Cryst.Solids **37** (1980) 165

35. G.Mathew, K.N.Madhusoodanan and J.Philip, Phys.Stat.Sol.(a) **168** (1998) 239

36. A.Giridhar and S.Mahadevan, J.Non-Cryst.Solids **51** (1982) 305

37. J.C.Phillips, J.Non-Cryst.Solids **34** (1979) 153

38. J.C.Phillips, J.Non-Cryst.solids **43** (1981) 37

39. J.C.Phillips, Phys.Stat.Solidi (b) **101** (1980) 473

40. M.F.Thorpe, J.Non-Cryst.Solids **57** (1983) 355

41. J.C.Phillips and M.F.Thorpe, Solid State Commun. **53** (1985) 699

42. S.Feng, M.F.Thorpe and E.Garboczi, Phys.Rev.B **31** (1985) 276

43. H.He and M.F.Thorpe, Phys. Rev.Lett. **54** (1985) 2107

44. K.Tanaka, Phys.Rev.B **39** (1989) 270

45. N.F.Mott, Phil.Mag. **22** (1990) 7

46. M.H.Cohen, H.Fritzsche, S.R.Ovshinsky, Phys. Rev.Lett. **22** (1969) 1065

47. H.Fritzsche "Electrical and Structural Properties of Amorphous Semiconductors" (Academic Press, London, 1973) 55

48. H.Fritzsche, "Amorphous and Liquid Semiconductors", ed: J.Tauc,

    (Plenum Press, New York, 1974) p.221

49. D.Adler, Nature Wissen shaften 69 (1982) 574

50. E.A.Davis and N.F.Mott, Phil.Mag. 22 (1970) 903

51. N.F.Mott, Phil. Mag. 26 (1972) 505

52. N.F.Mott, Contemp. Phys. 26 (1985) 203

53. M.H.Cohen, J.Non-Cryst. Solids 4 (1970) 391

54. D.Emin: "Aspects of the Theory of Small Polarons in Disordered

    Materials", Electronic and Structural Properties of Amorphous

    Semiconductors, ed: P.G.Le Comber, J.Mort (Academic Press, London,

    New York, 1973) p.261

55. E.Mooser and W.B.Pearson "Progress in Semiconductors" 5

    (Wiley, New York, 1960) p.104

56. M.Kastner , Phys. Rev.Lett. 28 (1972) 355

57. D.Adler , J.Chem.Ed. 57 (1980) 560

58. R.A.Street and N.F.Mott, Phys. Rev. Lett. 35 (1975) 1293

59. N.F.Mott, E.A.Davis and R.A.Street, Phil.Mag. 32 (1975) 961

60. M.Kastner and H.Fritzsche, Phil.Mag. B 37 (1978) 199

61. M.Kastner, D.Adler and H.Fritzsche, Phys. Rev. Lett. 37 (1976) 1504

62. R.Grigorovici, J.Non-Cryst.Solids 1 (1969) 303

63. G.Lucovsky " Physical Properties of Amorphous Materials", ed: D.Adler,

    (Plenum Press, New York, 1985)

64. L.Ley, M.Cardona and R.A.Pollk, "Photo emission in Solids-II"

    (Springer-Verlag, Berlin, 1979)

65. P.P.Seregin, A.R.Regel, A.A.Andreev and F.S.Wasredinov,Phys.Stat.Solidi **74a** (1982) 373

66. R.C.Mackenzie, "Differential and Thermal Analysis", ed: R.C.Mackenzie, (Academic Press, New York, 1970)

67. P.Nagels "Amorphous semiconductors", ed: M.H.Brodsky, (Springer Verlag, Berlin, 1985)

68. A.Vasko, D.Lezal and I.Srb, J.Non-Cryst. Solids **4** (1970) 311

69. R.C.Zeller and R.O.Pohl, Phys. Rev. B **4** (1971) 2029

70. S.Alexander, O.E.Wohlman and R.Orbach, Phys. Rev.B **34** (1986) 2726

71. J.Tauc, "Amorphous and Liquid Semiconductors", ed: J.Tauc (Plenum Press, 1974)

72. J.Tauc, Mat.Res.Bull. **5** (1970) 721

73. J.D.Dow and D.Redfield, Phys.Rev.B **5** (1972) 594

74. R.A.Street, Solid State Commun. **24** (1977) 363

75. Hamakawa , " Non-Crystalline Semiconductors", ed: M.Pollak, Vol.I (CRC Press, 1987)

76. A.Madan and M.P.Shaw , "The Physics and Applications of Amorphous Semiconductors" (Academic Press, 1988)

77. J.Gabona "Glass: Current issues" (1985)

78. G.Eisenman "Glass electrodes for hydrogen and other cations- Principle and Practice" Marcel Dekker (1967)

79. H.Mayer , "Structures and Properties of thin films",ed: C.A Neugebauer., J.B Newkirk. and D.A Vermilyea (Wiley, New York, 1959) p.225

80. P.B Hirsch., A.Howie , R.B Nicholson, D.W Pashley and M.J Whelan,

"Electron microscopy of thin crystals", (Butterworths, London, 1965)

81. C.A. Neugebauer and M.B Webb., J.Appl.Phys. **33** (1962) 74

82. D.W. Pashley and A.E.B Presland., J.Inst.Met. **87** (1959) 419

83. G.A. Bassett and D.W.Pashley, ibid (1959) 449

84. J.W Matthews, Phil.Mag. **4** (1959) 1017

85. V.A.Phillips, ibid **5** (1960) 571

86. R.W.Berry, P.M.Hall and M.T.Harris, "Thin Film Technology"(Van

Nonstrand, New York, 1968)

87. L.Holland, "Vacuum Deposition of Thin Films", (Chapman and Hall,

London, 1956)

88.J.C.Anderson (Ed.) "The use of Thin Films in Physical Investigation"

(Academic Press, London,1966)

89. R.Glang, "Handbook of Thin Film Technology", ed. By L.I.Maissel and

R.Glang (Mc Graw Hill, New York, 1970) p.1-3

90. D.S.Campbell, "Physics of Non-metallic Thin Films", ed. C.H.S.Dupuy

and Cachard (Plenum Press, New York, 1976) p.9

91. R.S.Ohl, Bell Sys.Tech.J. **31** (1952) 104

92. W.Shockley, "Forming semiconductor devices by ionic bombardment",

US Patent 2 787 564

93 W.D.Cussins, Proc.Phys.Soc.(London) **68** (1955) 213

94 J.O.Mc Caldin and A.E.Widmer, J.Phys.Chem.Solids **24** (1963) 1073

95.J.F.Gibbons, J.L.Moll and N.I.Meyer, Nucl.Instr. and Methods **38** (1965)

165

96.F.W.Martin, S.Harrison and W.J.King, IEEE Trans.Nuclear Science NS-

13 (Feb.1966) 22-29

97. W.J.King and J.T.Burrill, Proc.4th Photovoltaic Specialists Conf.,

   (Cleveland, Ohio) Pt.I- C, Sec.B2, 1964

98. M.I.Current and W.A.Keenan, Solid State Technology **28 (2)** (1985) 139

99. K.G.Stephens, "Handbook of Ion Implantation Technology"

   ed. J.F.Ziegler, (Elsevier 1992) p.455

100. I.G.Brown, "The Physics and Technology of Ion Sources", (John

   Wiley and sons, New York, 1989)

101. H.E.Schiott, Mat.Fys.Medd.Dan. Vidensk.Selsk **35 (9)** (1966) 1

102. R.B.Leighton, "Principles of Modern Physics", (New York: Mc Graw

   Hill, 1959), p.494-496

103. J.P. Biersack and L.G. Haggmark , Nucl. Inst. Methods **132** (1976) 647

104. J.P. Biersack and J.F. Ziegler , Springer series in Electro-physics

   10 (1982) 122

105. J.F. Ziegler in "Ion Implantation Science and Technology" (Academic

   Press,1984) p. 51

106. R.P.Webb "Practical Surface Analysis II, Ion and Neutral Spectroscopy",

   (Appendix 3) D. Briggs and M. Seah (eds.) (John Wiley, Chichester,

   1992)

107. R.Behrisch. and K.Wittmaack. (eds) Sputtering by Particle Bombardment

   III (Springer Topics in Appl. Phys. 64, 1991)

108. D.E.Harrison Rad. Effects **70** (1983) 1

109. D.E.Harrison Critical Revs in Solid State and Material Science, 14(1),

   s1 (1988)

110. M.T.Robinson ."Sputtering by Particle Bombardment", Chp. 3, p 73-144. Topics in Applied Physics, ed: R. Behrisch. Vol. 47 (Springer Verlag, Berlin, 1981)

111. H.H.Anderson, Nucl. Inst. Methods B 18 (1987) 321

112. Frenkel, "Simple Molecular Systems at Very High Density",eds: A. Polian, P. Loubeyre and N. Boccara (Plenum Press, 1989) p. 411

113. W.Eckstein, "Computer Simulation of Ion-Solid Interactions" Series in Material Science, 10 (Springer Verlag, Berlin, 1991)

114. J A.Sell, "Photothermal Investigations of Solids and Liquids", (Academic Press Inc, New York, 1988)

115. S.E.Bialkowski, "Photothermal Spectroscopy Methods for Chemical Analysis", (John Wiley &Sons, Inc.)

116. G.H. Brilmyer, A.Fujishima, K.S.V. Santhanam, A. J.Bard, Anal.Chem. 49 (1977) 2057

117. M. Bass, L.Liou, J.Appl.Phys. 56 (1984)184

118. H. Coufal, P.Hefferle, Appl.Phys. A 38 (1985) 213

119. H. Coufal, P. Hefferle, Can.J.Phys. 64 (1986) 1200

120. A. Mandelis, M.M. Zver, J.Appl.Phys. 57(9) (1985) 4421

121. A.Rosencwaig, "Photoacoustics and Photoacoustic spectroscopy", (Wiley, NewYork, 1980).

122. A.Rosencwaig and J.B.Willis, J.Appl.Phys. 51(8) (1980) 4361

123. D.A. Hutchins and A.C. Tam, IEEE Transactions on Ultrasonics, Ferroelectrics and Frequency Control UFFC-33 (5) (1986) 429

124. R.C. Leite, R.S. Moore, J.R. Whinnery, Appl.Phys.Lett. 5 (1964) 141

125. R.L.Swofford, M.E.Long, A.C.Albrecht, J.Chem.Phys **65** (1976) 179

126. H L. Fang, R.L. Swofford, J.Appl.Phys. **50(11)** (1979) 6609

127. A.C. Boccara, D.Fournier, J.Badoz, Appl.Phys.Lett. **36** (1980) 130

128. J.C.Murphy, L.C.Aamodt, J.Appl.Phys. **51(9)** (1980) 4580

129. L.C.Aamodt, J.C.Murphy, J.Appl.Phys. **52(8)** (1981) 4903

130. J.C.Murphy, L.C.Aamodt, Appl.Phys.Lett. **39(7)** (1981) 519

131. A.C.Boccara, D.Fournier, W.Jackson, D.Fournier, Opt. Lett. **5(9)** (1980) 377

132. N.J.Dovichi, T.G.Nolan, W.A.Weimer, Anal.Chem. **56** (1984) 1700

133. J.F.Power, M.A.Schweitzer, Opt.Eng. **36(2)** (1997) 521

134. S.E.Bialkowski, A. Chartier, Appl.Opt. **36(27)** (1997) 6711

135. M.A.Olmstead, N.M.Amer, Phy.Rev.Lett. **52** (1984) 1148

136. J.C. Cheng and S.Y. Zhang, J.Appl.Phys. **70** (1991) 7007

137. G.L.Bennis, R.Vyas, R.Gupta, S.Ang, W.D.Brown, J.Appl.Phys. **84** (1998) 3602

138 P.E.Nordal, S.O.Kanstad, Phy.Scr. **20** (1979) 659

139. A.Rosencwaig, J.Opsal, W.L.Smith, D.L.Willenborg, Appl.Phys.Lett. **46** (1985) 1013

140. A.Rosencwaig, J.Opsal, W.L.Smith, D.L.Willenborg, J.Appl.Phys. **59** (1986)1392

141. W.Zapka, A.C.Tam, Opt.Lett. **7** (1982) 86

142. C.J.Dasch, J.A.Sell, Opt.Lett. **11** (1986) 603

143. W.A.Weimer, N.J.Dovichi, Appl.Opt. **24** (1985) 2981

144. P.Hess, "Photoacoustic, Photothermal and Photochemical processes in

gases", (Springer-Verlag, New York, 1989)

145. H.B.Lin, A.J.Campillo, Appl.Opt. **24** (1985) 222

146. D.Fournier, A.C.Boccara, A.Skumanich, N.Amer, J.Appl.Phys. **59** (1986) 787

147. N.A.George, C.P.G.Vallabhan, V.P.N Nampoori, A.K.George, P.Radhakrishnan, J.Phys.D:Appl.Phys. **33** (2000) 3228

148. N.Mikoshiba, H.Nakamura, K.Tsubouchi, Proc.of the IEEE Ultrasonic Symposium San Diego, San Diego, CA (1982).

149. A.Rosencwaig, A.Gersho, J.Appl.Phys.**47** (1976) 64

150. H.S. Carslaw and J.C. Jaeger, "Conduction of heat in solids", (Oxford, Clarendon, 1959)

151. A.Figari, J.Appl.Phys. **71(7)** (1992) 3138

152. U.Zammit, M.Marinelli and R.Pizzoferrato, J.Appl.Phys. **69** (1991) 3286

Chapter 2

Experimental Techniques

This chapter presents a description of the experimental techniques used in the present investigations. A brief description of the experimental set up of a photothermal deflection spectrometer is given, followed by the illustration of the design and fabrication of a vacuum coating unit which is employed for the preparation of thin films in our studies. The chapter includes the details of the preparation of the samples and also the description of the UV-Vis-NIR Spectrophotometer used for the optical characterisation of the thin film samples under investigation.

2.1. Introduction

The samples under present investigations are in the form of thin films prepared by the technique of thermal evaporation. The essential requirement for this technique is a high vacuum deposition system at a pressure of about 10^{-5} T or less. The optical absorption measurements in the samples have been carried out using a photothermal deflection spectrometer. The absorption and transmission spectra of the samples are recorded using a UV-Vis-NIR spectrophotometer. Details of these techniques are described in the following sections of this chapter. The results presented in chapters 3, 4, 5 and 6 have been obtained by carrying out measurements using the above techniques.

2.2. Experimental set up of a photothermal deflection spectrometer

Photothermal Deflection Spectroscopy (PDS) is based on the detection of thermal waves generated in a sample due to the absorption of an intensity modulated light beam (pump beam) and subsequent non-radiative relaxation. The thermal wave generated in the sample is propagated to the surrounding medium and produces corresponding change in refractive index . This change in refractive index induces periodic deflection of a probe beam grazing the sample surface. Usually, the surrounding medium is chosen as CCl_4.

The deflection of the probe beam is detected using a position sensitive detector. The PDS signal depends on the optical absorption coefficient and thermal properties of the sample. Thus, by the analysis of the PDS signal recorded as a function of the wavelength of the incident pump beam, absorption spectrum of the sample can be obtained.

The two popular types of light sources used for pump beam are incandescent or arc lamps and lasers. A monochromator is used for selecting the wavelength of the pump beam. The lamp-monochromator combination can provide continuous tunability over a wide wavelength range. High pressure xenon arc lamps, Hg lamps, tungsten lamps etc. are the commonly used incandescent sources. The lamp-monochromator combination is used with strongly absorbing samples or where low resolution suffices.

Lasers are widely accepted light sources in photothermal experiments, especially for measuring weak absorption. This is mainly because of their high spectral radiance resulting from the extremely narrow line widths and high collimation. Modulation of the incident light beam is essential for the generation of photothermal signals. Amplitude modulation of the incident beam is the most commonly used method which can be achieved by several methods such as mechanical, electrical, electro-optic etc. One of the inexpensive, efficient and common methods to accomplish amplitude modulation is to use a mechanical chopper, while using which, care should

be taken to minimize the vibration noise.

The block diagram of the PDS experimental set up is shown in Fig.2.1. It consists of a high power Xe lamp (1000W) as the pump source and He-Ne laser as the probe beam. A monochromator is used for selecting the wavelength of the pump beam. The other components are a mechanical chopper for intensity modulation, a PDS cell made of quartz in which the sample is placed, a position sensitive detector for the detection of the probe beam deflection and a lock-in amplifier for signal processing. The normalization of the PDS signal for the wavelength dependence of the intensity of the xenon lamp can be achieved using a photoacoustic (PA) optical power meter as shown in the figure. The PA power meter consists of a PA cell with carbon black as the sample, microphone for detecting the PA signal and a lock-in amplifier for PA signal processing. Splitting a small portion of the pump beam and directing it to the PA cell can perform online normalization. Use of PA power meter provides an excellent normalization system for the entire range of wavelength used.

One of the great problems in PDS measurements is the detection of the deflection of the probe beam [1]. Usually a quadrant cell or a bicell position sensitive detector consisting respectively of four or two discrete detection elements on a single substrate separated by a miniscule gap, or a continuous position sensing detector is used for the purpose.
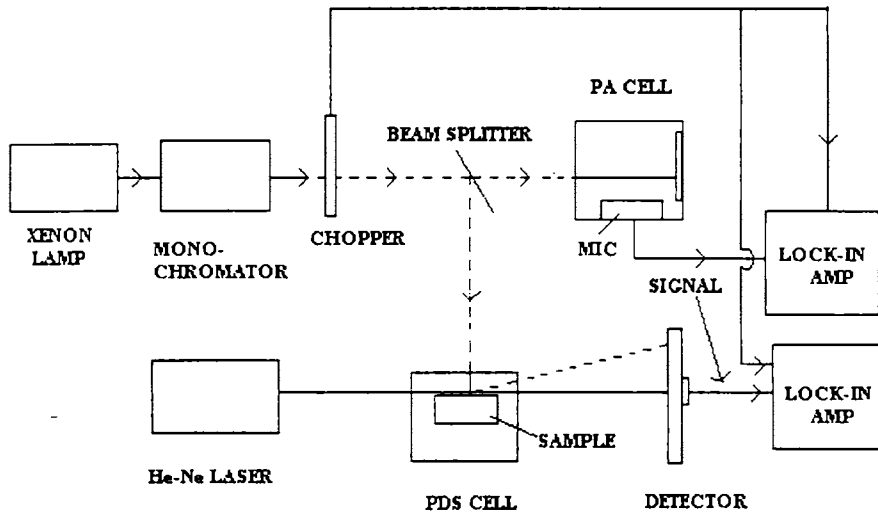
Fig.2.1. The block diagram of the PDS experimental set up

2.3. Design and fabrication of a thin film vacuum coating unit

The deposition technique of thin films using thermal evaporation requires a high degree of vacuum to form the material in the required composition and purity. The process of deposition starts by creating vacuum in the deposition chamber, usually of the order of 10^{-5} T or less. In the deposition procedure, the supporting devices needed include material sources, masking arrangements, power supplies, thickness monitoring devices, deposition rate controllers etc. Hence, a typical vacuum coating system consists mainly of two parts; the vacuum pumping system and the deposition set up.

The process of deposition chamber evacuation begins at atmospheric pressure and then proceeds to high vacuum. For this, a variety of combination of pumps such as oil-diffusion, turbo-molecular, getter ion and cryo absorption [2] are made use of. The most common pumping arrangement for the production of high vacuum consists of a positive displacement mechanical pump for initial evacuation followed by a vapour stream pump, usually a diffusion pump [3]. Mechanical pumps move gases by the cyclic motion of a system of mechanical parts. The objective of gas transport by means of rotating bodies can be accomplished in different ways, and various operating principles are reviewed by Dushman [4]. A survey of commercially available models and their performance has been published by Lucas [5]. For thin film evaporators, the type of mechanical pump which is of interest is the oil-sealed rotary pump, using which ultimate pressures of about 10^{-3} T can be obtained.

Diffusion pumps operate on the idea of evacuating a vessel by momentum transfer from streaming to diffusing molecules, which was first patented by Gaede [6]. The basic features of modern diffusion pumps have been described by Langmuir in 1916 [7]. Diffusion pumps are essentially vapour ejectors which can't discharge directly into the atmosphere. Therefore, it is always backed by a mechanical pump for the removal of the output discharge. By using diffusion pumping system, vacuum of the order of 10^{-6} T can be easily achieved. The general description of vacuum evaporation apparatus and

methods along with the basic plant layouts and design features, reviews of the

commoner types of vacuum hardware and established operating techniques

have been extensively reported in various books [8-13].

The layout of a pumping system of a general purpose coating unit is

shown in Fig.2.2. The system is divided into three main parts, the pumping

system, the coating chamber and the electrical services. The pumping system

consists of a diffusion pump backed by a rotary pump along with a number of

vacuum valves for separating different parts of the system from each other and

from the surrounding atmosphere. The coating chamber is a bell jar dome

which is provided with an evaporation source and a substrate holder, both

coming inside it. The bell jar dome opens at a gasket-sealed joint and may be

fully raised, thus allowing complete assembly and positioning of materials

inside the chamber. The evaporation source is a molybdenum boat or a

tungsten filament in which the bulk material is evaporated. The electrical

services provide electrical power into the coating chamber for heating the

vapour sources.

The ball jar dome rests on a base plate which is provided with a number

of feedthroughs for electrical connections and also for fitting the gauges for the

measurement of pressure. The design and construction of electrical

feedthroughs vary according to the currents and voltages which they are

intended to transmit. High current, low voltage feedthroughs are needed to

energize resistance heated evaporation sources. The base plate is provided with a bore at its centre through which the coating chamber is connected to the diffusion pump via a baffle valve or a butterfly valve. This valve permits the diffusion pump to be under vacuum and at operating temperature when the coating chamber is at atmospheric pressure. Two types of gauges are commonly used, one is a thermal conductivity gauge known as the pirani gauge and the other is a thermal ionization gauge known as the penning gauge. The pressure range detectable by a pirani gauge is about 10^{-3} to 10^{-1} T, while all pressure measurements below 10^{-3} T are carried out by a penning gauge.

The rotary pump is connected to the coating chamber by a valve known as the roughing valve and to the backing side of the diffusion pump by a valve known as the backing valve. This forms a two-way valving system made with two isolation valves joined by a "T" section. When the diffusion pump is kept continuously at working temperature, it is necessary to reduce the chamber pressure to a fraction of millimeter of mercury before opening the baffle valve, otherwise the diffusion pump fluid would be blown as vapour into the backing space. The coating chamber is pre-exhausted by means of the rotary mechanical pump by a process called "roughing" which is achieved through the roughing valve. The process of roughing reduces the pressure in the system, bringing it to the correct operating range. When suitable operating pressure conditions are reached, the diffusion pump takes over. The rotary mechanical pump is then
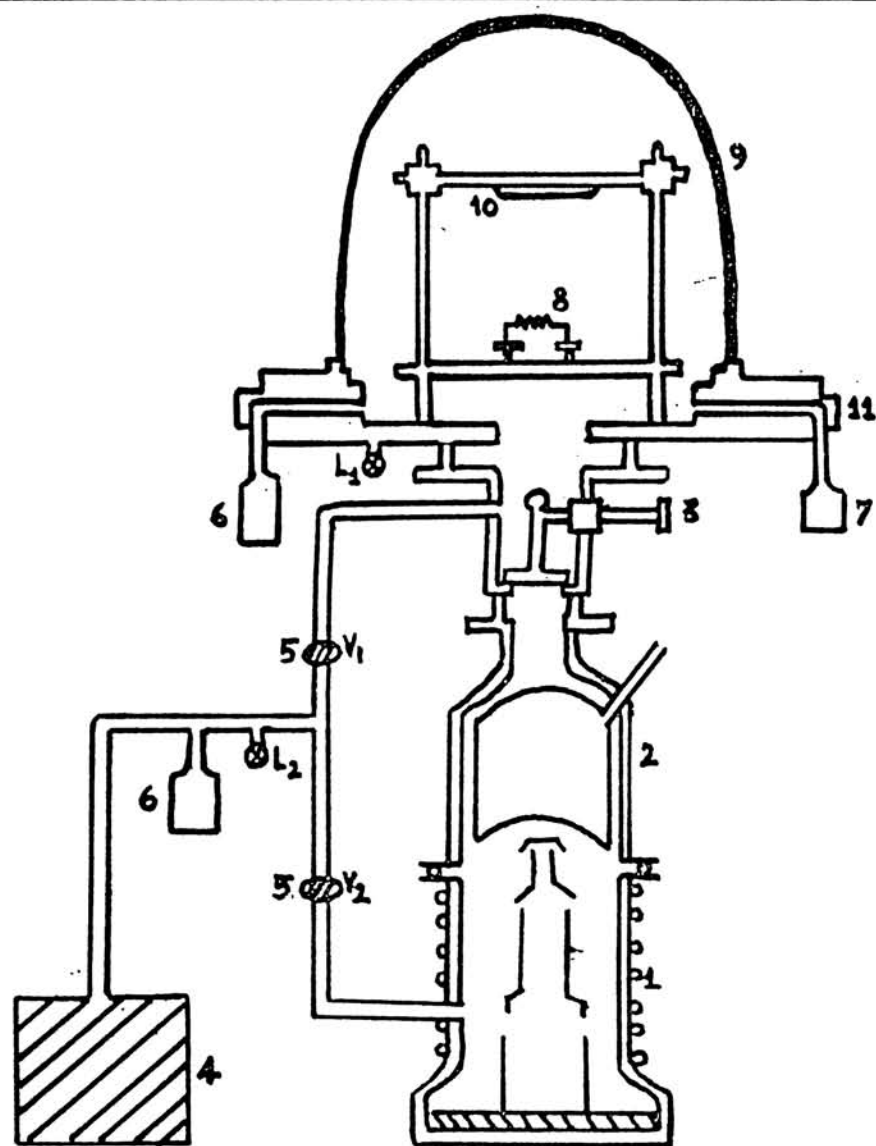
1. Diffusion Pump
2. Liquid Nitrogen Trap
3. Baffle valve/ Butterfly valve
4. Rotary Pump
5. V_1 – Roughing Valve
   V_2 – Backing Valve
6. Pirani Gauge Head
7. Penning Gauge Head
8. Tungsten Filament
9. Glass Bell Jar
10. Substrate Holder
11. Base Plate
12. L_1 – Dome Leak
    L_2 – T Section Leak

Fig.2.2. The layout of a pumping system of a general purpose coating unit

used to maintain proper discharge pressure conditions for the diffusion pump at the foreline connection. This operation is called forepumping or "backing" which is achieved through the backing valve. The diffusion pump is also provided with a water circulation arrangement for cooling.

Air admittance valves are fitted on the coating chamber and also in the T section. Opening the valve on the chamber admits air into it, thus making it possible to raise the dome and take the coated films and other materials out. The valve in the T section is opened soon after the rotary pump is switched off so as to admit air into it and hence to prevent back suction of oil into the stator. A needle valve may also be connected to the chamber if the gas pressure is to be controlled during ionic bombardment cleaning etc.

The photograph of the vacuum coating system that we have designed and fabricated for the preparation of thin films of materials under present study is shown in Fig.2.3. The base plate is polished well and chromium plated. The thickness at the side of the base plate is 1.7 cm. A bore of 10.5 cm diameter is made at the centre of the plate for connecting the diffusion pump. 12 feedthroughs each of 1.5 cm diameter are provided on the base plate. Two ports are used for the pirani and penning gauges, two more ports for fitting heavy duty electrodes for carrying electrical power into the coating chamber for heating the vapour source, and the remaining ports are closed by dummies. A 30 cm glass dome is pressure-sealed on the base plate using an L-gasket. A 10V,
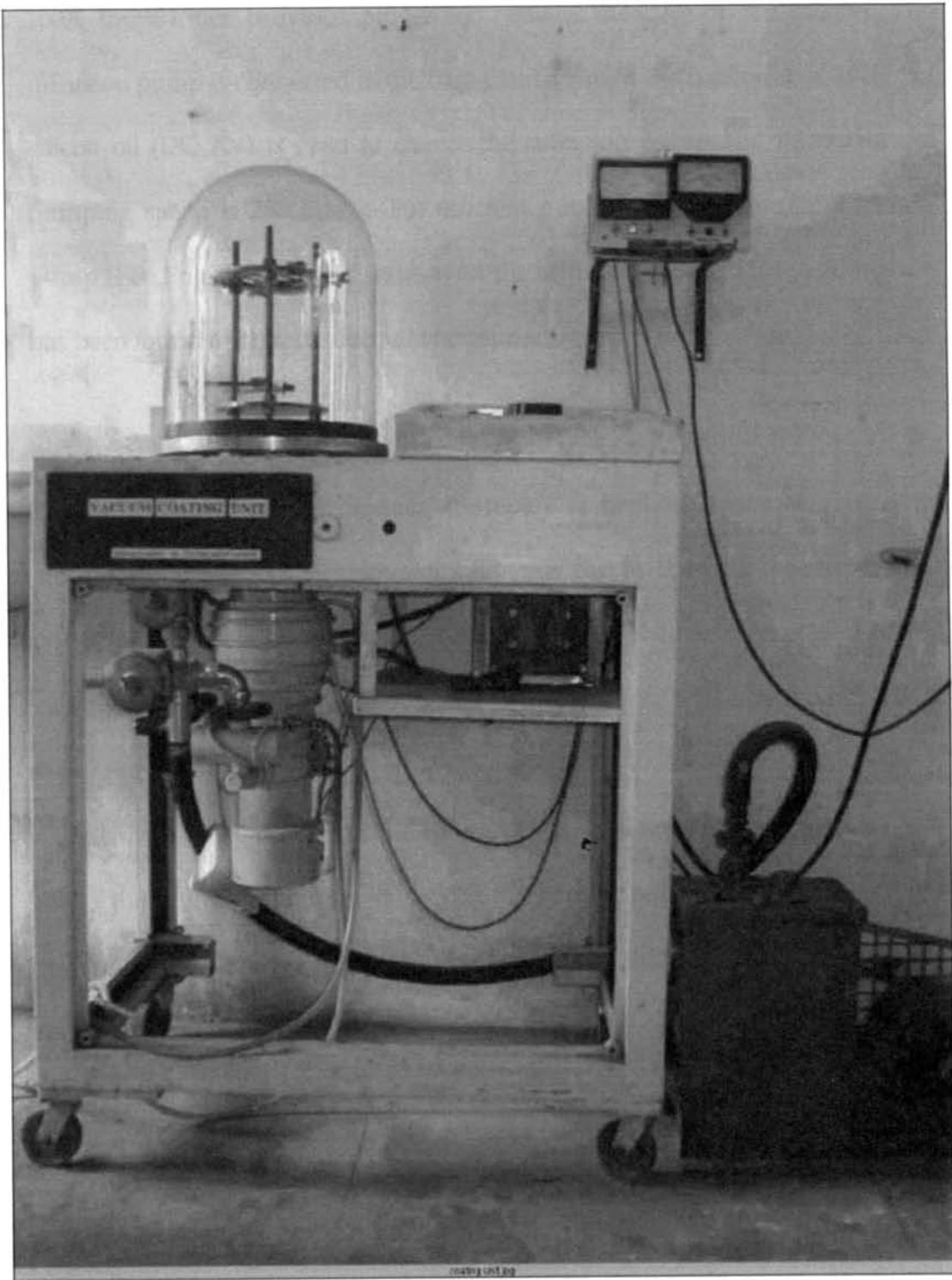
Fig.2.3 Photograph of the vacuum coating system

100A transformer provides power for resistive heating of the source. The diffusion pump is connected to the base plate through the baffle valve. 100 cc of silicon oil (DC 704) is used to charge the diffusion pump and its maximum pumping speed is 200 litre/s. For efficient pumping, a 200 litre/min. rotary pump (Leo Engg.) is used in series with the diffusion pump. This combination has been found to provide ultimate pressures of about 10^{-5} T.

2.4. Sample Preparation

There are a number of techniques to prepare amorphous materials. Since the amorphous phase is thermodynamically less stable than the corresponding crystalline form, its preparation can be regarded as the addition of excess free energy in some manner to the crystalline polymorph, which can be done by faster rate of cooling.

The most common method for preparing bulk amorphous material is the melt quenching technique, in which the amorphous solid is formed by continuous hardening i.e; increase in viscosity of the melt. An essential pre-requisite for glass formation from the melt is that the cooling be sufficiently fast to preclude crystal nucleation and growth, as crystal growth will always dominate over the formation of amorphous phase if allowed to take place.

The usual way of preparing amorphous samples is to seal the charge (1 to 10g) in a fused silica or quartz ampoule under a good vacuum ($\sim 10^{-6}$ T) and keep the ampoule in a rocking or rotating furnace at sufficiently elevated

band gap of samples under investigation. Hitachi model U-3410 double beam recording spectrophotometer has been employed for this purpose. It comprises of a monochromator section (including control section), display section, floppy disc section, graphics plotter and operating section. The unit has a wavelength ranging from 187 to 2600 nm with 0.07 nm resolution. The wavelength accuracy is 0.2 nm in the UV-Vis range and ±1 nm in the NIR range. The monochromator adopts the model 340 prism/grating double monochromatic system. The lenses used in the conventional monochromator have all been replaced by mirrors to eliminate image deviation due to chromatic aberration. The PbS detector converges the light beam with a torroidal mirror located below the photomultiplier. This permits placing the PbS symmetrically against the sample and reference beam whereby the two beams are completely balanced. A mechanical chopper is placed before the first monochromator to chop the light beam, which minimizes deviation in zero signal. The long life, easily replaceable iodine free tungsten lamp is used as the visible wavelength light source. The photometric output from the detector is fed through the preamplifier to an A/D converter and input into the computer, where it is discriminated into reference signal, sample signal and zero signal for storage by gate signals obtained in synchronization with rotation of the sector mirror for splitting the light beam. The reference signal is compared with a predetermined standard value and used for controlling the voltage applied to the dynode of

the photomultiplier.

2.6. Conclusions

A vacuum coating unit employing the technique of thermal evaporation has been designed and fabricated for the preparation of thin film samples under investigation. A photothermal deflection spectrometer has also been set up for the optical characterisation of these samples.

References

1. J.D. Spear and R.E. Russo, Rev. Sci. Instrum. **67** (1996) 2481

2. A. Roth, "Vacuum Technology" (North-Holland, Amsterdam, 1976)

3. C.G. Carpenter, "Vacuum Technology" (Adam Hilger, London, 1970)

4. S. Dushman, "Scientific Foundations of Vacuum Technique", 2nd ed., , (John Wiley and Sons Inc., New York, 1962) p.118

5. T.E. Lucas, Vacuum **15** (1965) 227

6. W. Gaede, Deutsches Reichspatent 286, 404, 1913; and Ann.Physik **46** (1915) 357

7. I. Langmuir, Gen.Elec.Rev. **19** (1916) 1060

8. R. Glang, R.A .Holmwood and J.A .Kurtz, "High Vacuum Technology" in "Handbook of thin film technology", eds: L.I.Maissel and R. Glang , Mc-Graw Hill, New York, 1983)

9. A. Guthrie, "Vacuum Technology" (John Wiley, New York, 1963)

10. G. Lewin, "Fundamentals of Vac.Sci.and Tech.", (Mc-Graw Hill, New York, 1965)

11. A.H. Turnbull, R.S. Barton and J.C. Riviere, "An Introduction to Vacuum Technique" (George Newnes, London, 1962)

12. H.J. Steinherz, "High-Vacuum Engineering" (Reinhold, New York, 1963)

13. L. Holland, "Vacuum deposition of thin films" (Chapman and Hall Ltd., London, 1970)

Chapter 3

Preparation and optical characterisation of amorphous Ge_xSe_{100-x} and As_xSe_{100-x} thin films

-

This chapter gives the details of the preparation and optical characterisation of the thin film samples of the systems Ge_xSe_{100-x} ($5 \leq x \leq 40$) and As_xSe_{100-x} ($10 \leq x \leq 60$). The absorption and transmission spectra of these samples are analysed. From the absorption spectra, the optical band gaps are determined. The variation of optical band gap of these samples with composition is investigated and the observed behaviour is explained on the basis of various models. A simple calculation following traditional methods has been employed for deducing the refractive indices of the samples from the fringe pattern of the transmission spectra and the variation of refractive index with wavelength for different compositions of the samples is also investigated.

3.1. Introduction

Amorphous semiconducting chalcogenide glasses constitute an important class of materials with potential applications in electronic, electrochemical, optical and magnetic areas of modern technology such as solar cells, optical recording and imaging devices and memory and switching devices. The two-fold coordination present in their structure enables them to cover a wide range of compositions, with physical properties varying appreciably even among samples of the same material. This composition dependent tunability helps designing of materials for various specific requirements as passive and active elements in electronic devices [1,2] and in the fabrication of solid state batteries, electrochemical sensors and electrochromic optical devices [3,4]. For most of the device applications, these materials are used in the form of thin films. The optical properties of thin films are sensitive to many parameters including their thickness and hence can provide important information on both device and materials characteristics. The studies of vanadium oxide [5] and tungsten oxide [6] electrochromic layers have indicated that a better understanding of semiconductor film behaviour is needed to control optical properties.

In this chapter, we report the determination of optical band gaps and refractive indices of amorphous Ge_xSe_{100-x} ($5 \leq x \leq 40$) and As_xSe_{100-x} ($10 \leq x \leq 60$) thin films. The absorption and transmission spectra of these samples are analysed. The absorption edges of semiconducting materials are commonly

used to determine their optical band gaps. A careful examination of the optical transmittance can be used to reveal basic design and materials parameters. From the absorption spectra, the optical band gaps are determined. The variation of optical band gap of these samples with composition is investigated and the observed behaviour is explained on the basis of chemical bonding between the constituents. A simple calculation following traditional methods has been employed for deducing the refractive indices of the samples from the fringe pattern of the transmission spectra and the variation of refractive index with wavelength for different compositions is also investigated.

Of the glass forming alloys of the family $A_x{}^V B_{100-x}{}^{VI}$, $As_x Se_{100-x}$ glasses are perhaps the most studied ones. It is found that the incorporation of additives like As or Ge in pure amorphous selenium used for photographic drums improves the lifetime and sensitivity of the material [7]. These additives crosslink the Se chains and decrease the tendency of crystallization, thereby increasing the lifetime of pure Se drum [8]. The various properties of amorphous As-Se alloys have been presented in literature by a number of papers [9, 10-12] and also by Mott and Davis [13]. Several workers have carried out the studies of composition dependent variation of properties of these glasses [14].

3.2. Experimental details

$Ge_x Se_{100-x}$ glass samples of different compositions in the range $(5 \leq x \leq 40)$ and

As_xSe_{100-x} glass samples of different compositions in the range $(10 \leq x \leq 60)$ in the bulk form are prepared by the conventional melt quenching technique. Appropriate quantities of the constituent elements having 99.999% purity are sealed in an evacuated quartz ampoule. The ampoule is then kept in a furnace at about 1200K for about 24 hours. For homogeneous mixing of the constituents, the ampoule is rotated periodically at a speed of 10-12 rpm. Finally the ampoule is quenched in ice water and then broken to take out the sample. The amorphous nature of the sample is confirmed by X-ray diffractometry. The thin films of these glasses of approximate thickness $3000A^0$ are prepared by thermal evaporation in high vacuum $(2 \times 10^{-5}$ T) on glass substrates.

3.3. Determination of optical energy gap (E_g)

Optical band gap of the samples under investigation are determined by recording their optical absorption spectra using a UV - Vis - NIR spectrophotometer (Hitachi- Model U3410).

For amorphous semiconductors, in the high absorption region, (absorption coefficient $\beta \geq 10^4 cm^{-1}$) the absorption is characterized by

$$\beta h\nu = B (h\nu - E_g)^2 \tag{3.1}$$

where B is a constant , $h\nu$ is the photon energy and E_g is the optical energy gap. Thus, a plot of $(\beta h\nu)^{1/2}$ as a function of $h\nu$ yields a straight line whose intercept on the abscissa provides E_g.

3.4 Determination of refractive index (n)

Considering a thin film of refractive index n bounded by two transparent media with refractive indices n_o and n_1, (n_o and n_1 are the refractive indices of air and the substrate respectively) the transmission of the film is given by [15],

$$T = \frac{16n_0 n_1 n^2 \alpha}{C_1^2 + C_2^2 \alpha^2 + 2C_1 C_2 \alpha \cos(4\pi n t / \lambda)} \tag{3.2}$$

Where C_1 = (n+n_0) (n_1+n), C_2 = (n-n_0) (n_1-n) and

$$\alpha = \exp(-4\pi k t / \lambda) = \exp(-\beta t) \tag{3.3}$$

where β is the absorption coefficient of the thin film.

For a semiconducting film on a transparent non-absorbing substrate for which $n > n_1$, $C_2 < 0$, the extreme values of the transmission are given by the formulae,

$$T_{max} = \frac{16n_0 n_1 n^2 \alpha}{(C_1 + C_2 \alpha)^2} \tag{3.4}$$

$$T_{min} = \frac{16n_0 n_1 n^2 \alpha}{(C1 - C2\alpha)^2} \tag{3.5}$$

from which,

$$n = [N + (N^2 - n_0^2 n_1^2)^{1/2}]^{1/2} \tag{3.6}$$

where

$$N = \frac{\left(n_0^2 + n_1^2\right)}{2} + 2n_0 n_1 \left[\frac{(T_{max} - T_{min})}{(T_{max} T_{min})}\right]$$

Thus considering T_{min} and T_{max} as continuous functions of λ which are the envelopes of the minima and maxima in the transmission spectrum at the same wavelength, n is determined.

3.5. Results and Discussion

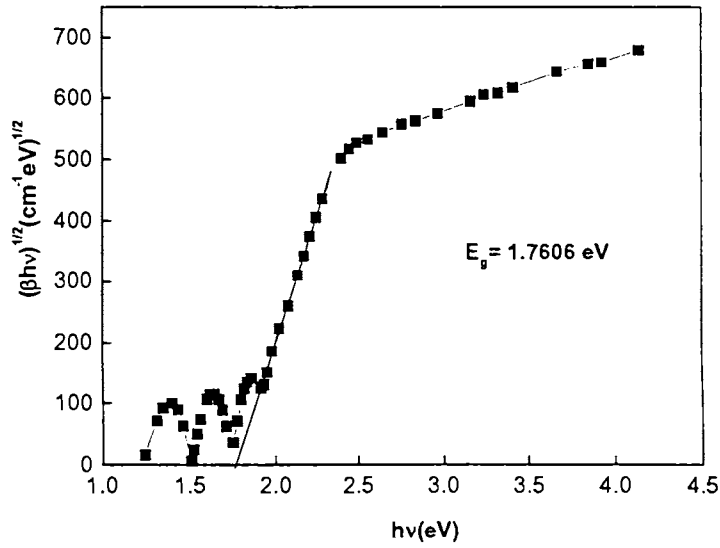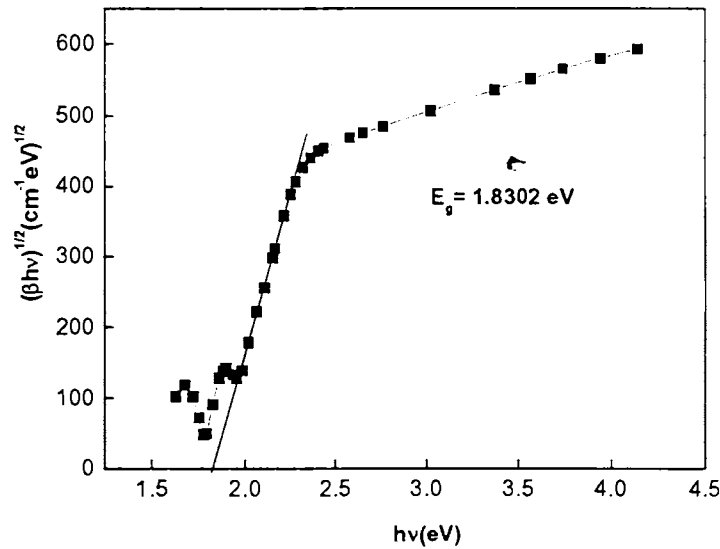The determination of optical energy gap E_g from a plot of $(\beta hv)^{1/2}$ versus hv for a representative sample of Ge_xSe_{100-x} (x = 10) is described in Fig.3.1 while that for a representative sample of As_xSe_{100-x} (x = 20) is described in Fig.3.2. Fig.3.3 gives the variation of the optical energy gap E_g determined from the absorption spectra with the composition parameter x for the different compositions of Ge_xSe_{100-x} samples. It is found that E_g increases with increase in Ge content for x < 33 and decreases with the same for x > 33, thus giving a maximum value for x = 33. This observed variation may be explained on the basis of the variation in the distribution of the different possible types of bonds in the material with the composition.

Since amorphous materials do not possess long range order, their electronic properties can be described on the basis of the nature of the short range order [16] and the formation of bonding, antibonding and non bonding bands formed in the system [17]. In Ge_xSe_{100-x} glass system, the three possible types of bonds are Ge-Se, Ge-Ge and Se-Se in the order of decreasing bond energies 49.1, 46.5 and 44 Kcal/mole respectively. [18]. According to the chemically ordered network model [19], for compositions with x < 33, the

system contains both Ge-Se and Se-Se bonds. At x = 33, known as the stoichiometric composition, the system contains only Ge-Se bonds and for x > 33, both Ge-Se and Ge-Ge bonds are present. Thus, the increase in the number of Se-Se bonds for compositions x < 33 and of Ge-Ge bonds for x > 33 has the effect of reducing the average bond energy of the system and consequently, the value of E_g decreases on either side of the stoichiometric composition.

The variation of E_g with the composition parameter x for the different compositions of As_xSe_{100-x} samples is given in Fig.3.4. It is observed that the measured values of E_g are in good agreement with the energy gap data already available [11]. From Fig.3.4, it may be seen that the value of E_g is close to that of amorphous Se (~ 2eV) for small concentrations of As. As x increases, the value of E_g decreases, reaches a minimum value at x = 40 and then increases. This composition x = 40 = x_c corresponds to the formation of stoichiometric compound As_2Se_3. This observation is not unexpected as it has been experimentally established by observing the variation of several properties of As_xSe_{100-x} system as a function of composition that the critical composition corresponding to the stoichiometric compound commonly known as the chemical threshold of the glass occurs at x = 40 in the system at which unusual variations in various physical properties have been reported. Hurst and Davis have observed a minimum in the energy gap and a maximum in conductivity at

Fig.3.1. Determination of optical energy gap E_g from a plot of $(\beta h\nu)^{1/2}$versus hv for a representative sample of Ge_xSe_{100-x} (x = 10)

Fig.3.2. The determination of optical energy gap E_g from a plot of $(\beta h\nu)^{1/2}$ versus hv for a representative sample of As_xSe_{100-x} (x = 20)

91
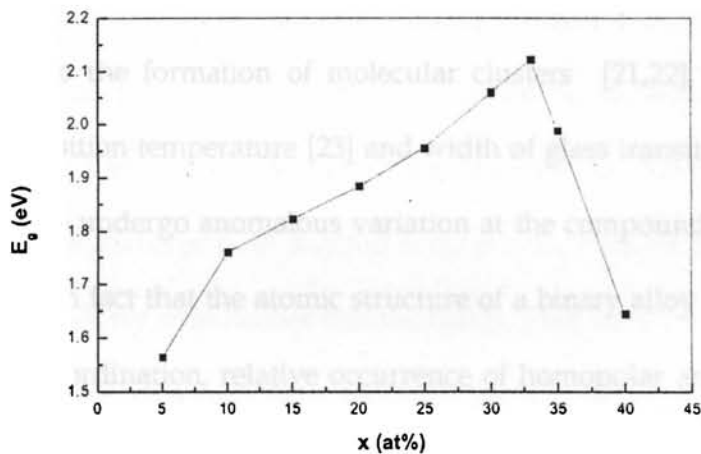
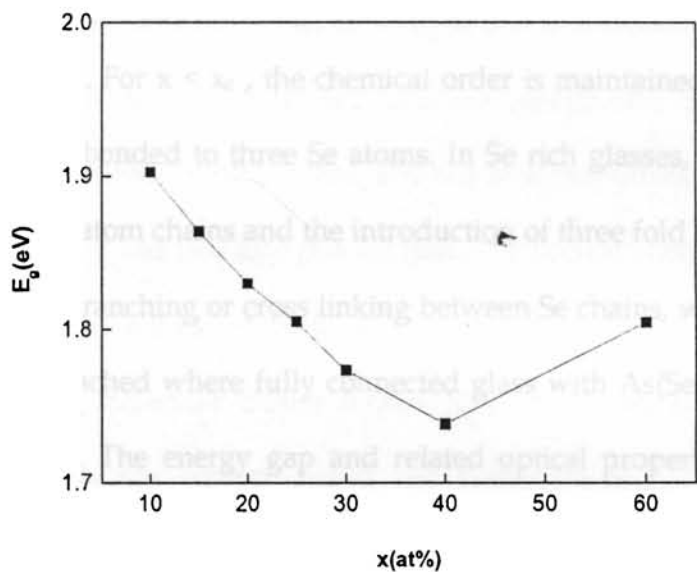**Fig.3.3.** The variation of optical band gap (E_g) with composition parameter x for Ge_xSe_{100-x} samples.

Fig.3.4. The variation of optical band gap (E_g) with composition parameter x for As_xSe_{100-x} samples .

the x = 40 composition [20]. Evidence for a medium range order in As_2Se_3 has

been obtained from the existence of a first sharp diffraction peak

corresponding to the formation of molecular clusters [21,22]. Raman shifts

[9,10], glass transition temperature [23] and width of glass transition peaks [24]

are also found to undergo anomalous variation at the compound composition.

It is a well known fact that the atomic structure of a binary alloy is determined

by the atomic coordination, relative occurrence of homopolar and heteropolar

bonds and the bonding topology. Therefore, an approach based on this

consideration may be used to explain these results.

At the stoichiometric composition, the network is formed by fully

connected $As(Se_{1/2})_3$ pyramidal structural units with minimum number of

homopolar bonds. For $x < x_c$, the chemical order is maintained for As atoms,

each of which is bonded to three Se atoms. In Se rich glasses, the network is

dominated by Se atom chains and the introduction of three fold coordinated As

atoms produces branching or cross linking between Se chains, which continues

until x = 40 is reached where fully connected glass with $As(Se_{1/2})_3$ structural

units are formed. The energy gap and related optical properties are closely

related to the nature of bonding between atoms and the short range order

existing in the system. According to the chemically ordered network (CON)

model, the As_xSe_{100-x} system contains only fully coordinated As-Se bonds at

x = 40 [19]. For $x < x_c$, the system contains As-Se and Se-Se bonds while for x >

x_c, both As-Se and As-As bonds are present. The bond energies of As-As, As-Se and Se-Se bonds are 43.4, 44.96 and 44 K Cal/mole respectively [18]. As these values are very close, it seems to be difficult to explain the variation of E_g with x on the basis of CON model. However, the increase in network disorder associated with the deviation from stoichiometry may be thought as responsible for pushing the mobility edge further into the bands, thus increasing E_g.

A variety of models have been proposed by several workers to explain the variation of E_g with x. The random network model [25] developed by White [26] for amorphous alloys which characterizes their band structure in terms of tight binding matrix elements [27] has been applied to the As-Se system. This model attributes the observed variation of E_g to the interaction involving lone pair electrons of As and Se. In As-Se, both the constituents have lone pair electrons, As atom having three bonding and one lone pair orbitals and Se atom having two bonding and two lone pair orbitals. The optical energy gap for As-Se glasses is indeed associated with the lone pair to antibonding transition. According to the molecular cluster model [28], the chemical order of the network is intrinsically broken during the formation of clusters and the presence of wrong bonds at the stoichiometric composition has the effect of reducing the average bond energy , thus causing a decrease in the value of E_g. A molecular model for As_2Se_3 based on chemically ordered raft structure has been put forward by Phillips et.al.[29] which explains well the anomalies in the

diffraction data, Raman scattering etc. The strong inter cluster interactions in the system are mediated by non bonding lone pair electrons. As, Se and As_2Se_3 have bonding electrons at lower energies compared to the lone pair electrons. When the lone pair electrons are arranged in layers, the non bonding interaction is maximized. This increases the width of the lone pair band, thus reducing the optical energy gap.

Fig.3.5 represents a typical transmission spectrum of a representative sample of Ge_xSe_{100-x} and Fig.3.6 represents that of a representative sample of As_xSe_{100-x} which show T_{min} and T_{max} as continuous functions of λ which are the envelopes of the minima $T_{min}(\lambda)$ and maxima $T_{max}(\lambda)$. The transmission spectra show that the films have an average transmission of 80%.

In Fig.3.7, the variation of refractive index for four different compositions of Ge_xSe_{100-x} samples is plotted as a function of wavelength, while in Fig.3.8, the same for seven different compositions of As_xSe_{100-x} glass samples is plotted as a function of wavelength. It may be noticed that the refractive index decreases with the increase in wavelength. It is also found that the variation of refractive indices of these samples with composition is in close correlation with the variation of densities with composition of the samples.
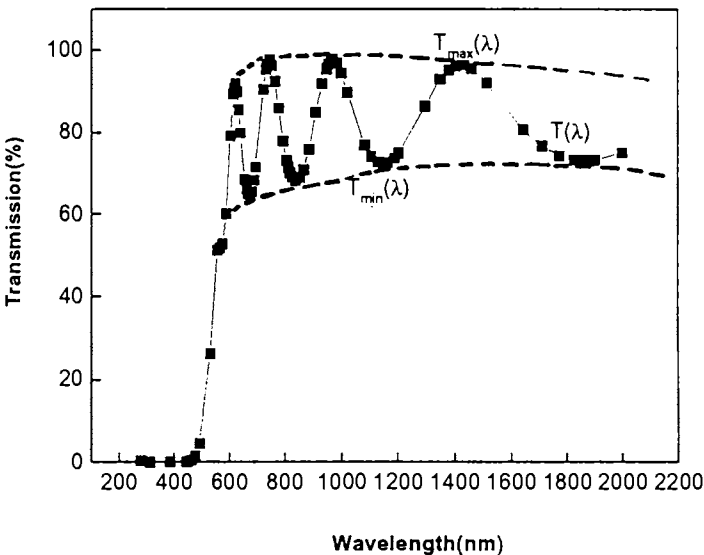
Fig.3.5. Typical transmission spectrum of a representative sample of Ge_xSe_{100-x}
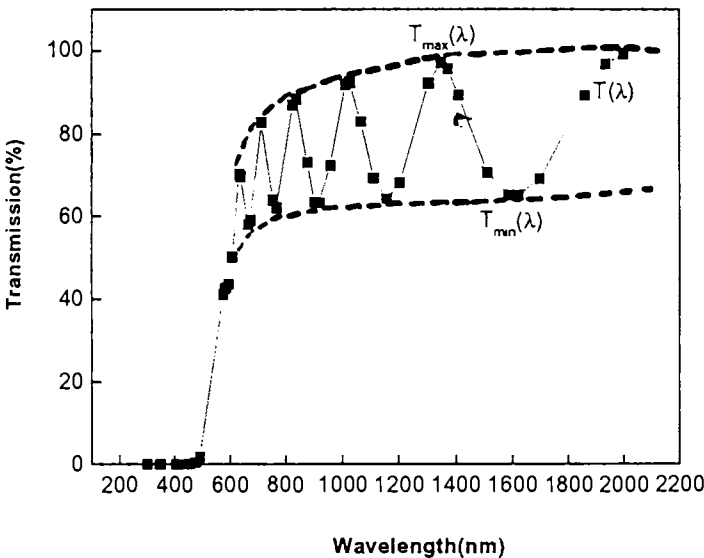
Fig.3.6. Typical transmission spectrum of a representative sample of As_xSe_{100-x}
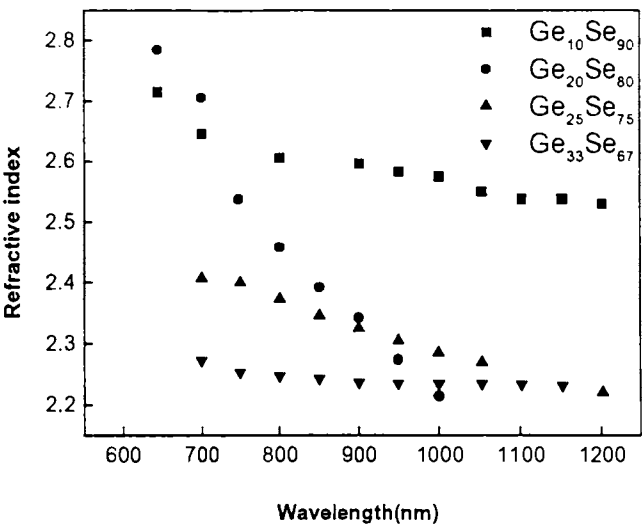
Fig.3.7. The variation of refractive index for different compositions of Ge_xSe_{100-x} samples as a function of wavelength
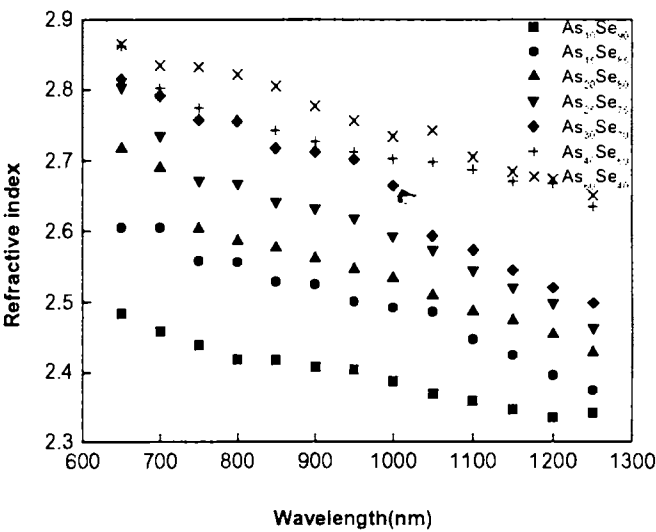

Fig.3.8. The variation of refractive index for different compositions of As_xSe_{100-x} samples as a function of wavelength

3.6. Conclusions

Thin film samples of the systems Ge_xSe_{100-x} ($5 \leq x \leq 40$) and As_xSe_{100-x} ($10 \leq x \leq 60$) have been prepared. The absorption and transmission spectra of these samples are analysed. From the absorption spectra, the optical band gaps are determined. The variation of optical band gap of these samples with composition is investigated and the observed behaviour is explained on the basis of various models. A simple calculation following traditional methods has been employed for deducing the refractive indices of the samples from the fringe pattern of the transmission spectra and the variation of refractive index with wavelength for different compositions of the samples is also investigated.

References

1. Hamakawa, "Non Crystalline semiconductors" ed.M.Pollak,Vol. I (CRC Press, 1987)

2. A.Madan and M.P.Shaw, "The Physics and applications of amorphous semiconductors" (Academic Press, 1988)

3. J.Gabona, "Glass: Current issues"(1985)

4. G.Eisenman, "Glass electrodes for hydrogen and other cations-Principle& Practice" Marcel Dekker (1967)

5. S.F.Cogan, N.M.Nguyen, S.J.Perrotti, and R.D.Rauh, J.Appl.Phys. **66** (1989) 1333

6. S.F.Cogan, T.D.Plante, M.A.Parker, and R.D.Rauh, J.Appl. Phys. **60** (1986) 2735

7. G.Pfister, J.Elect.Mat. **8** (1979) 789

8. E.A.Marseglia and E.A.Davis, J.Non-Cryst.Solids **50** (1982) 13

9. J.C.Phillips, J.Non-Cryst.Solids **43** (1981) 37

10. R.J.Nemanich, G.A.N.Connell, T.M.Hayes and R.A.Street, Phys.Rev.B **18** (1978) 6900

11. R.A.Street, R.J.Nemanich and G.A.N.Connell, Phys.Rev.B **18** (1978) 6915

12. G.Lucovsky, R.H.Geils and R.C.Keezer, in "The Physics of Non-Crystalline Solids", ed: G.H.Firschat (Trans Tech, Switzerland, 1977) p.299

13. N.F.Mott and E.A.Davis, "Electronic Processes in Non-Crystalline Materials" (Clarendon Press, 1971)

14. J.C.Phillips, J.Non-Cryst.Solids **34** (1979) 153
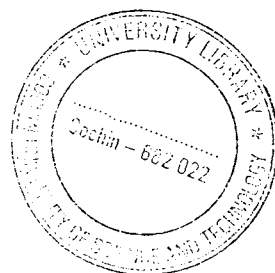
15. J.C.Manifacier, J.Gasiot, and J.P.Fillard, J. Phys. E: Sci. Instrum. **9** (1976) 1002

16. A.F.Ioffe and A.R.Regal, Progr.Semicond. **4** (1960) 239

17. M.Kastner, Phys.Rev.Lett. **28** (1972) 355

18. R.T.Sanderson, "Chemical Bonds and Bond Energy", (Academic Press, New York, 1971)

19. G.Lucovsky and T.M.Hayes, in : "Amorphous Semiconductors", Ed. M.H.Brodsky, (Springer-Verlag, Berlin, 1979) p.215

20. C.H.Hurst and E.A.Davis, Int.Conf. on Amorphous and Liquid Semiconductors, Garmisch, September 1973

21. A.A.Vaipolin and E.N.P. Koshits, Sov.Phys.Solid State **5** (1963) 186

22. A.L.Renninger and B.L.Averbach, Phys.Rev.B **8** (1973) 1507

23. M.B.Myers and E.J.Felty, Mater. Res.Bull. **2** (1967) 535

24. J.C.Phillips, Phys.Today **35** (1982) 27

25. D.E.Polk, J.Non-Cryst.Solids **5** (1971) 365

26. R.M.White, J.Non-Cryst.Solids **16** (1974) 387

27. D.Weaire and M.F.Thorpe, Phys.Rev. **4** (1971) 2508, 3518

28. J.E.Griffiths, G.P.Espinosa, J.P.Remeika and J.C.Phillips, Solid State Commun. 40 (1981) 1077; Phys.Rev.B **25** (1982) 1272

29. J.C.Phillips, C.A.Beevers and S.E.B.Gould, Phys.Rev.B **21** (1980) 5724

Chapter 4

Subgap optical absorption studies in boron implanted silicon

This chapter deals with the employment of the subgap optical absorption measurement by PDS to characterize the defects, amorphization and annealing behaviour in silicon implanted with B^+ ions. The effect of ion dose, implantation temperature and thermal annealing on the subgap absorption are investigated. The chapter also presents the profiles of the ion range and vacancy distribution obtained by the TRIM simulation. The changes induced in the band edge slopes and in the subgap features of the spectra are described. The various stages of formation, quenching and annealing of divacancies are monitored as a function of implantation conditions and annealing cycles. The chapter also describes the investigations on the structural modifications and defect evolution under annealing in amorphous material produced by implantation.

4.1. Introduction

Ion implantation technique is widely used for the controlled incorporation of dopants in silicon. As the technique employs bombardment of the target with energetic ions, creation of defects in the target material is unavoidable. Thus the defect recovery by annealing is an essential part of the doping process. The amount of defects and their nature are known to depend on various implantation parameters like ion energy, dose, temperature, ion mass etc [1]. Depending on the conditions, the process can produce either a damaged crystalline layer or a completely amorphous layer. The type and amount of crystalline damage within a damage cluster are different for heavy and light ions [2]. The possible manner in which the damage cluster interacts to promote crystalline to amorphous transition are different for these cases. It becomes important to study the defect creation and damage recovery under different implantation and annealing conditions for optimizing the implantation process. Various techniques have been used for the study of structural, electronic and optical properties of ion implanted silicon [3, 4, 5]. These studies helped in understanding various types of primary and secondary defects and their evolution.

One of the important consequences of the creation of damaged crystalline or amorphous layers as a result of implantation is the modification

of electronic structure. This results in substantial optical absorption in the subgap region below the band gap due to the modification of band edges and introduction of defect related electronic states in the gap. Thus the method of monitoring optical absorption in the subgap region can be a useful technique for studying the defects and their annealing induced recovery. Photothermal Deflection Spectroscopy (PDS) [6] is a powerful technique for the measurement of weak optical absorption and so can be used for measuring weak subgap absorption associated with defects even in a thin implanted layer [7]. A unique feature of ion implantation is that crystalline semiconductor materials can be transformed to the amorphous state in a quasi-continuous manner by varying the implantation parameters. So, in principle, it is possible to investigate changes in the electronic transport and optical properties as increasing amounts of disorder are introduced into the c-Si lattice. Implanted Si, in its amorphous structure has drawn considerable attention because amorphization and epitaxial regrowth after annealing are predominantly used in semiconductor processing. It has been reported that complete amorphization of crystalline Si during ion implantation resulted in a remarkable reduction of extended defects after annealing [8]. Structural relaxation mechanisms in which the amorphous network relaxes to a relatively stable structure also gained considerable attention [9].

The damaged crystalline state produced by implantation consists of a lot

of point defect and point defect complexes. In semiconductors, point defects often introduce electronic states in the band gap and can exist in different electronic configurations. A vacancy in Si can be either neutral or negatively or positively charged, an interstitial can be neutral or positively charged. The thermal equilibrium concentration of charged point defects depends on the doping type, i.e; on the Fermi level and on its energy level position in the energy band gap. Point defects form complexes among themselves, like divacancy V-V or V_2, di-interstitial I-I or with impurities like V-O, As-I etc [1]. The knowledge of some of the specific defects that have been observed in Si helps us formulate a reasonable picture of the types of damage that we might expect to accompany the implantation of energetic ions [10]. They are the vacancy-interstitial pair (Frenkel defect), vacancy-impurity pairs, divacancy, dislocation lines and loops and vacancy and interstitial platelets. The intrinsic defects in irradiated Si include the divacancy [11], the four vacancy [12], five - vacancy complexes [13], and the di- interstitial [14]. From the point of view of ion implantation, perhaps the most important simple defect is the divacancy. The crystallographic form of the divacancy as deduced from EPR measurements [15] is shown in Fig.4.1. Divacancies may form directly if an incident ion succeeds in displacing adjacent silicon atoms [16]. Simple vacancies may also combine to form divacancies. Since the divacancy is stable at temperatures in excess of room temperature, it is a prominent defect in silicon

that has been implanted at room temperature. The role of intrinsic point defects in determining the behaviour of microelectronic devices has been a topic of intense research [17]. The divacancy center, V_2 has been thoroughly studied for about 30 years by numerous authors applying various experimental techniques [11, 18]. V_2 can exist in four different charged states [singly positive (+), neutral (0), singly negative (-), and doubly negative (2-)]. In the case of irradiated samples, so far, eight absorption bands have been observed. At room temperature, the bands have peak absorption at 1.8, 3.3, 3.9, 5.5, 6.0, 20.5, 27.0, and 30.1μm, respectively. Absorption bands at 0.69 eV (1.8 μm), 0.37 eV (3.3 μm) and 0.32 eV (3.9 μm) have been associated with the various charge states of the divacancy [19]. Among the absorption bands, the 1.8μm band was the first to be observed. It has been deduced that the defect responsible for this absorption band has an energy level at about 0.21 eV below the conduction band and that the absorption will not be seen if the level is occupied by electrons [20]. It has been shown that it is possible to correlate the magnitude of the absorption measured at the 1.8 μm band against the divacancy concentration [21]. This enables the monitoring of the concentration of diva-cancies in ion implanted Si by subgap absorption as a function of both the implantation conditions and the annealing cycles [22].

In this chapter, subgap absorption measurement using PDS has been employed as a tool to characterize the defects, amorphization and annealing
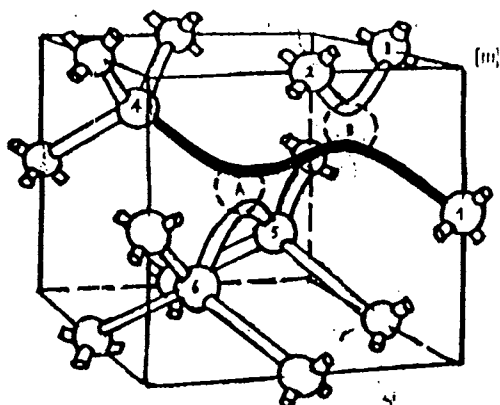
Fig.4.1. The crystallographic form of the divacancy as deduced from EPR measurements

behaviour for the case of light ion implantation in Si with B^+ ion implantation.

The effect of ion dose, implantation temperature and thermal annealing on

subgap optical absorption are investigated. The changes induced in the band –

edge slopes, and in the subgap features of the spectra are described. The

various stages of formation, quenching and annealing of divacancies are

monitored as a function of implantation conditions and annealing cycles.

Structural modifications and defect evolution under annealing in amorphous

materials produced by implantation are also investigated.

4.2. Experimental details

The investigations were carried out on 300 µm thick <111> Si samples. The

samples were implanted with B^+ ions at 300 K and 80K. Implantation was

carried out with different ion doses in order to obtain damaged crystalline samples of different defect concentration as well as completely amorphous sample. Inorder to get sufficiently thick layers with a homogeneous damage profile, B^+ions were successively implanted with energies of 300, 150 and 50 KeV. The total dose was varied from 2×10^{14} to 1×10^{16} cm^{-2}. TRIM computer simulation has been used to get profiles of the ion range and vacancy distribution.

The defect induced subgap optical absorption measurements have been carried out by Photothermal Deflection Spectroscopy (PDS), a highly sensitive technique which allows the detection of low levels of absorption. It is based on the measurement of the thermal energy deposited in the investigated sample when it absorbs modulated electromagnetic radiation. This induces a periodic temperature fluctuation in the medium in front of the sample and consequently a similar refractive index variation which is detected by monitoring the deflection of a probe laser beam grazing the sample surface using a position sensitive detector. The signal is directly related to the optical absorption coefficient. In semiconducting samples, the absorption coefficient value can be determined easily as the sample is opaque for photon energies above band gap when the sample is sufficiently thick ($\beta d \gg 1$). The absolute absorption values are obtained by normalizing the spectra with respect to the corresponding values obtained in the spectral region where the sample is optically opaque.

The signal S can be expressed as [23]

$$S = S_0 \left[1 - \exp(-\beta d) \right] \tag{1}$$

where S_0 is the signal corresponding to the saturation level above band gap. In the present case, a Xenon arc lamp with monochromator is used as the exciting source and a He-Ne laser is used as the probe beam. The coupling medium used is CCl_4.

4.3. Results and Discussion

A. Effect of ion dose and substrate temperature

Fig.4.2 shows the absorption spectra in the subgap region down to 0.48 eV for samples implanted at 300 K with different ion doses. The main features observed in this figure are increase in absorption in the entire subgap region with increase in ion dose, a change in slope in the subgap absorption with dose and the presence of an absorption peak at 0.69 eV (1.8 μm) associated with the divacancy. The corresponding spectra for the 80 K implanted samples are given in Fig.4.3, which shows that the divacancy absorption peak disappears for doses $\geq 2 \times 10^{15}$ cm^{-2}, indicating a clear difference with respect to Fig.4.2. The disappearance of divacancy peak for higher doses is known to associate with the complete amorphization of implanted layer in Si [4]. The results presented in Fig.4.2 and 4.3 are further analysed in terms of the magnitude of absorption in the subgap region (β), divacancy concentration (N_{vv}) and the inverse

108

logarithmic slope parameter (E_0) which characterizes the exponential dependence of the absorption in the subgap region. The absorption feature associated with the divacancy is analysed to estimate the divacancy concentration. For this, the excess absorption due to the divacancy band alone (β_{vv}) has been determined by subtracting from the absorption spectra, the contribution due to the background, determined by fitting the data away from the band. The β_{vv} values obtained from this procedure for samples implanted with different doses are shown in Fig.4.4(a) and 4.4(b) for 300 K and 80 K implantation respectively. For 80 K implantation, divacancy is present only for lower doses as the layer becomes amorphous at higher doses. From β_{vv}, the concentration of divacancies N_{vv} is estimated using the relation N_{vv} (cm^{-3}) = 7.7×10^{16} $\beta_{vv\ max}$ [20], where $\beta_{vv\ max}$ is the maximum value of β_{vv} in the band. The average number of divacancies produced per ion is determined as $R_{vv} = N_{vv} / l\varphi$, where φ is the ion dose and l is the implanted layer thickness.

- The depth of the implanted layer is estimated from the results of TRIM simulation [24]. The depth of the layer was taken as $d = R_p + 2\Delta R_p$, where R_p and ΔR_p are the ion projected range and straggling respectively. The value of the implanted depth obtained was 857 nm. Fig.4.5 and Fig.4.6 represent the profiles of the ion range and vacancy distribution respectively obtained by the TRIM simulation for the implantation. The dose dependence of N_{vv} and R_{vv} is presented in Fig.4.7 for both 300 K and 80 K implanted samples. In the case of
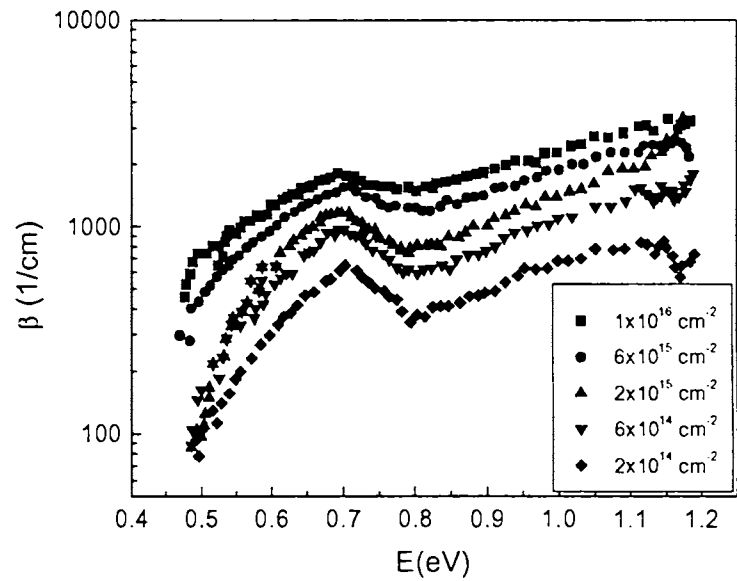
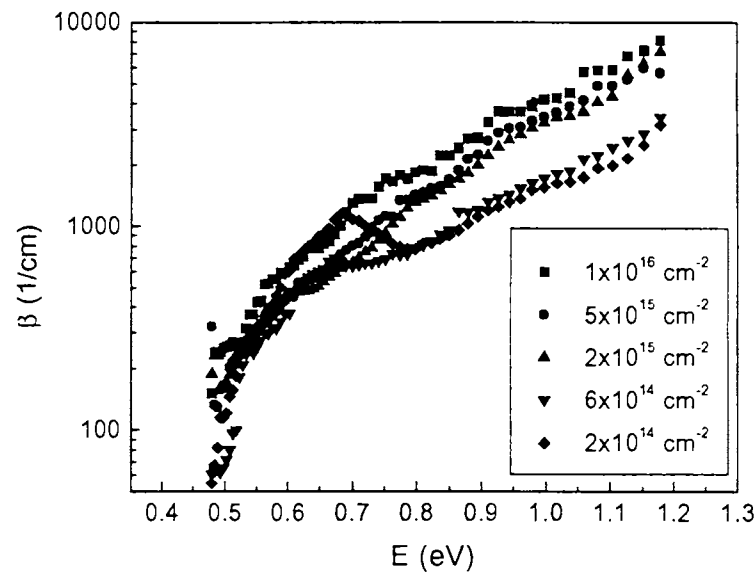**Fig.4.2.** Dose dependence of the subgap absorption for Si implanted with B⁺ ions at 300 K

Fig.4.3. Dose dependence of the subgap absorption for Si implanted with B⁺ ions at 80 K
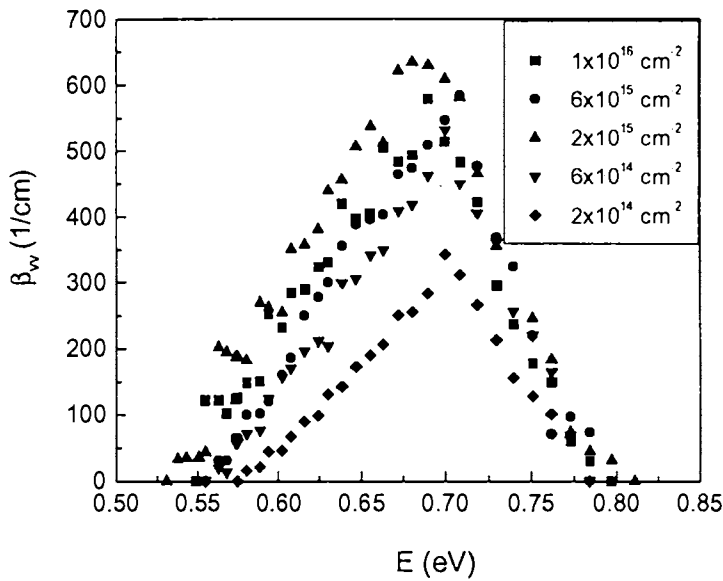
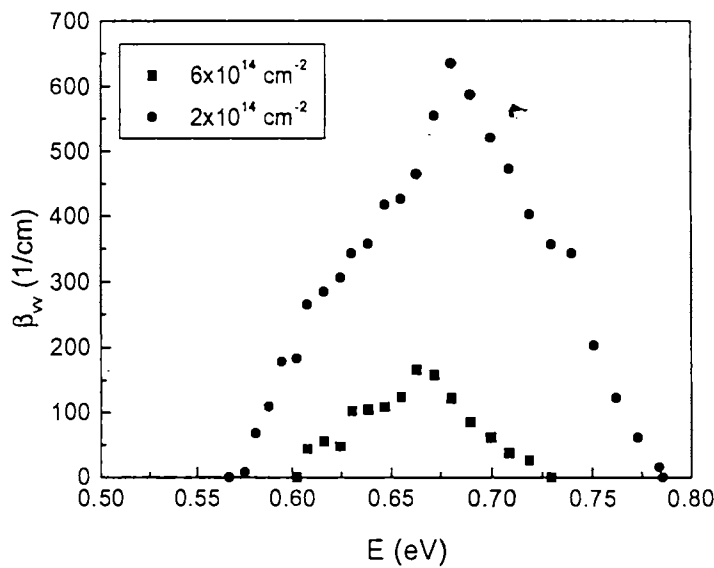**Fig.4.4(a).** Dose dependence of the divacancy absorption bands in Si implanted with B⁺ ions at 300 K

Fig.4.4(b). Dose dependence of the divacancy absorption bands in Si implanted with B⁺ ions at 80 K

300 K implantation which does not produce an amorphous layer, N_{vv} increases initially with dose and then reaches a plateau upto the maximum implanted dose of 10^{16} ions/cm^2. In contrast with this, for the case of 80 K implantation, N_{vv} shows a sharp decrease prior to the amorphization dose of 2×10^{15} cm^{-2}. The above behaviour in divacancy concentration is associated with the damage accumulation and its substrate temperature dependence in light ion implanted Si. For the case of heavier ion implantation in Si, it is known that room temperature implantation results in an increase in divacancy concentration first, goes through a maximum at a concentration of $\approx 7\times10^{19}$ cm^{-3} and then decreases before it becomes zero when a completely amorphous layer is formed with the overlap of damage clusters [16]. Taking the energy required for divacancy production as 1.5 ± 0.5 KeV [22], this corresponds to an average energy deposited per unit volume of $\approx 10^{20}$ KeV/cm^3. Beyond this, the concentration of divacancy decreases and a complete amorphization of the implanted layer occurs at an average deposited energy of $\approx 10^{21}$ KeV/cm^3 [22]. For heavier ion, this happens for relatively low doses of 10^{14}-10^{15} cm^{-2}. In the present case of 300 K implantation of B$^+$ ions, we do not observe a maximum in divacancy concentration even for a dose of 10^{16}cm^{-2}. The plateau reached in Fig.4.7 corresponds to a divacancy concentration of $\approx 5\times10^{19}$ cm^{-3} which will correspond to a maximum energy deposited per unit volume of $\approx 10^{20}$ keV/cm^3. However, in the case of 80 K implanted sample, a decrease in

divacancy concentration is observed in Fig.4.7, with an increase in dose when

the dose range is below the dose at which complete amorphization is

observed (i.e; $2x10^{15}cm^{-2}$). A clear maximum in divacancy concentration is not

seen in the figure as it could be possible that such a maximum occurs below the

minimum dose ($2x10^{14}$ cm^{-2}) used in the present study. The distinct behaviour

shown by B^+ ion implanted Si in comparison with the implantation of heavier

ions like Sb, Si etc. can be associated with the nature of defect production which

is proportional to the energy spent in atomic processes. In the case of lighter

ions like B^+, more energy is spent in electronic stopping process, compared to

the case of heavier ions, making only lesser energy available per ion for the

atomic collision process which results in lower production rate for

displacements. In this case, the defects produced directly by the projectile in

room temperature implantation are not stable. Stable defects subsequently are

produced by the diffusion of vacancies to damage nucleation sites. Therefore,

the initial damage cluster consists of species that are mobile at room

temperature which diffuse to nucleation sites to form defects that are stable at

room temperature. Such stable defect profile can consist of Frenkel defects,

divacancies etc. Amorphization does not occur in such case even for doses as

high as 10^{16} cm^{-2} as seen in the present measurement for 300 K implanted

sample. In comparison with this, in the case of heavy ion implantation, damage

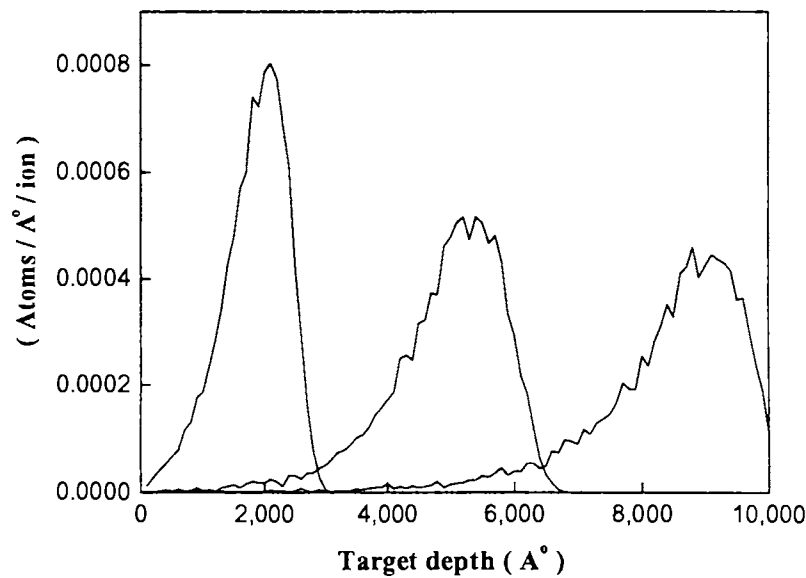nucleation takes place spontaneously in a heavily damaged region which leads

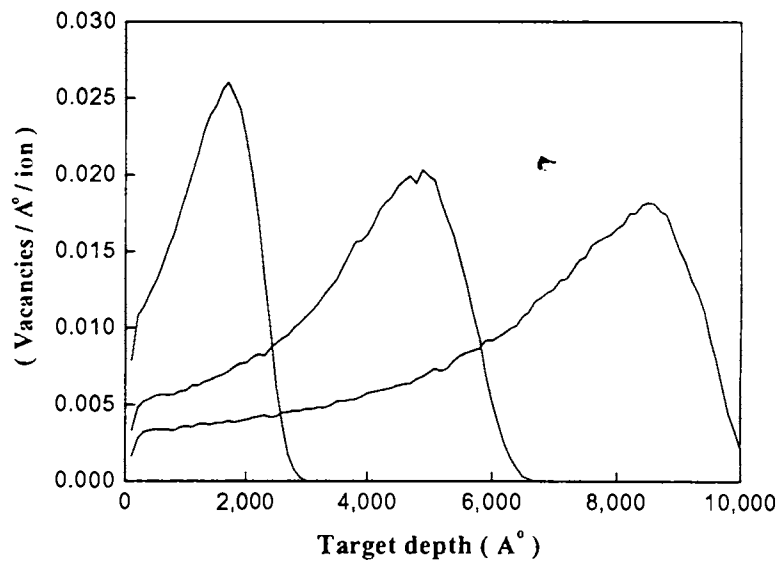**Fig.4.5.** Simulated ion range profile for 300KeV B⁺ ions implanted into Si

Fig.4.6. Simulated vacancy distribution profile for 300KeV B⁺ ions implanted into Si

to amorphization at a relatively low dose [16] The above picture based on defect

diffusion for room temperature implantation is further evident from the

fact that for low temperature implantation, lattice disorder saturates at a B^+

ion dose of $\approx 10^{15}$ ions/cm^2 leading to amorphization as the defects are much

less mobile at this temperature. R_{vv} shows a sharp decrease in the case of low

temperature implanted sample as the amorphization sets in, whereas a gradual

decrease is observed in the case of 300 K implanted samples. So, in the case of

300 K implanted samples, as the divacancy density reaches a plateau, more and

more other types of point defects like Frenkel defects are formed. An indication

of this is obtained from the comparison of the magnitude of the absorption

coefficient in the subgap region, where all defects contribute to absorption, for

samples implanted with different doses. For this, the absorption coefficient at

1eV is plotted as a function of dose for 300 K and 80 K implanted samples in

Fig.4.8. The absorption for the 300 K implanted sample is found to increase as

the dose is increased even in the range where the divacancy concentration

shows a plateau. In the case of 80 K implanted samples, the figure shows that

the absorption increases sharply as the amorphization of the layer takes place.

For 300 K samples, the fact that there is no abrupt change in the absorption in

Fig.4.8. suggests that the defect cluster that form as a result of vacancy diffusion

have no amorphous content indicating that individual light ions must probably

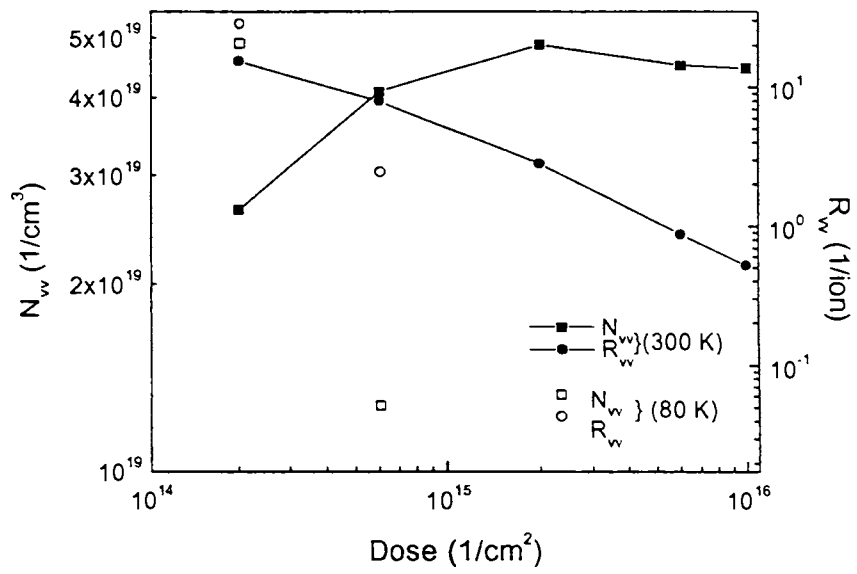produce only Frenkel defects. Evidence for the increasing production of point

Fig.4.7. Dose dependence of divacancy concentration (N_{vv}) and average number of divacancies produced per ion (R_{vv}) for 300 K and 80 K implanted samples
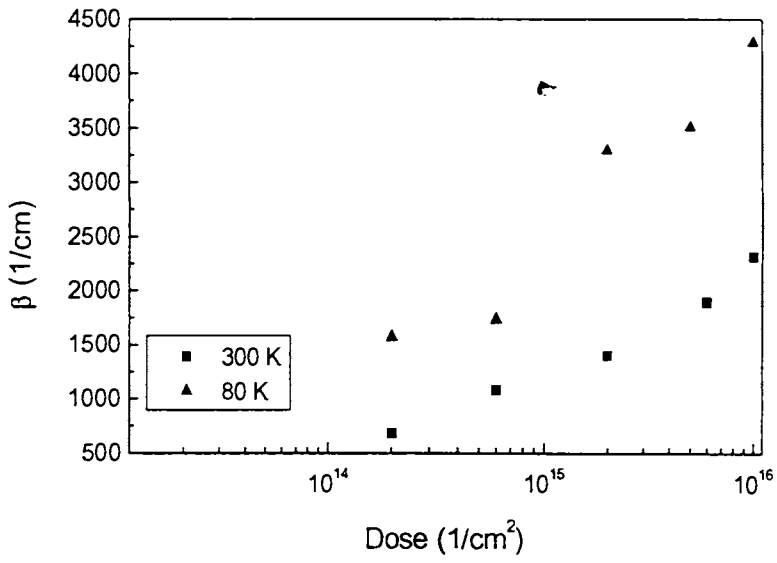

Fig. 4.8. Dose dependence of the absorption at 1 eV for 300 K and 80 K implanted samples

116

defects other than divacancies in larger number in the region of divacancy plateau has been provided earlier from RBS channeling measurement for the <111> direction [5]. RBS results were fitted well assuming a displacement distance of 0.5 A°. The concentration of the displaced atoms estimated from RBS measurements is found to increase with increasing dose.

The subgap absorption away from the divacancy peak was analysed using the exponential absorption behaviour $\beta = \beta_0 \exp\left[\dfrac{E}{E_0}\right]$ associated with band-tail states. Inverse logarithmic slope E_0 which characterizes the exponential dependence of absorption in the band edge region has been obtained by fitting the absorption data before the onset of divacancy peak with such a relation. The variation of E_0 for both 300 K and 80 K implanted samples with dose is given in Fig.4.9. The figure also shows the variation of β_0 obtained from the fit which correlates with the variations in E_0 [25]. This is further illustrated in Fig.4.10, where the mutual dependence of these parameters is shown. It is observed from Fig.4.9 that E_0 increases with dose for 300 K implanted sample where no amorphous zone is formed. This is consistent with previous observation that the band edge absorption results from the total amount of defects produced consisting of divacancies, Frenkel defects etc. The increase in E_0 again suggests that even as divacancy concentration reaches a plateau, concentration of other defects increases. In the case of 80 K implanted sample which has amorphous zone or a completely amorphous layer, the
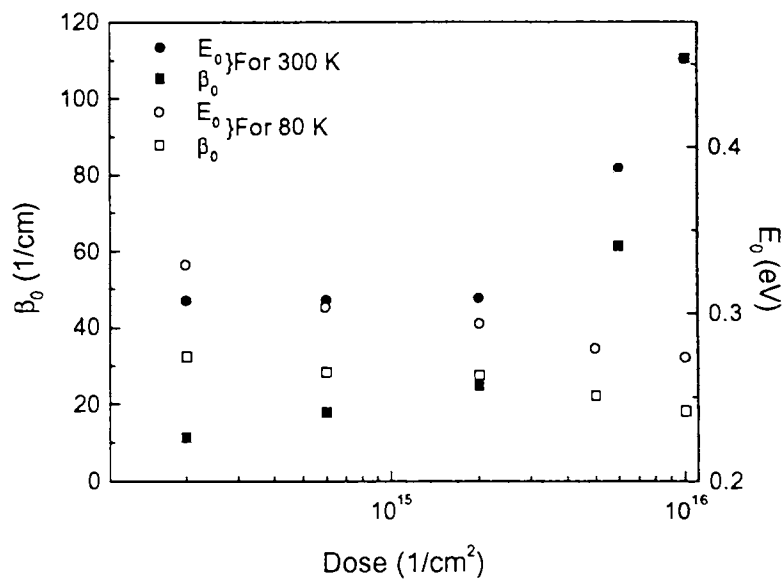
Fig. 4.9. Dose dependence of β_0 and E_0 for 300 K and 80 K implanted samples.
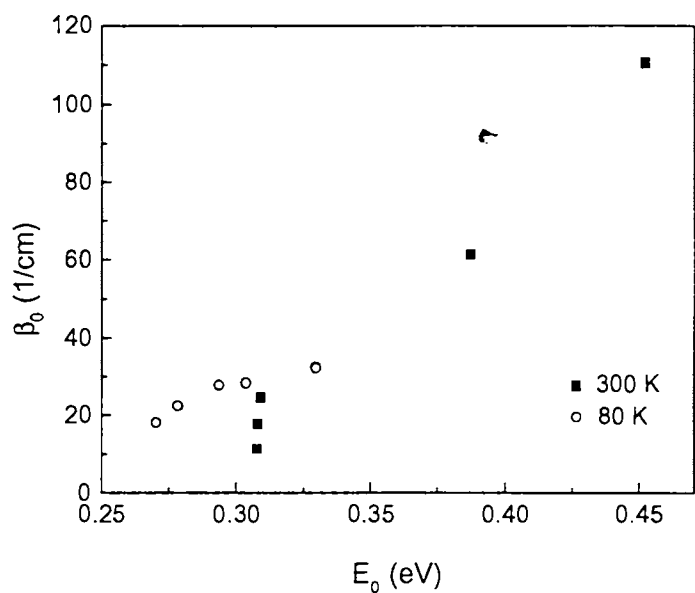

Fig. 4.10. The mutual dependence of the parameters β_0 and E_0

absorption becomes steeper and correspondingly, there is a decrease in E_0 towards the E_0 value for amorphous Si. So the nature of defects and the associated nature and distribution of band tail states are different for 300 K implanted sample which produces a damaged crystalline layer and 80 K sample which produces an amorphous layer.

B. Annealing studies

The annealing induced change in the defect profile is investigated in the sample implanted at 300 K with dose 1×10^{16} cm^{-2}. The sample is subjected to isochronal annealing for 15 minutes at increasing temperatures upto 250°C. Fig.4.11 shows the evolution of the spectra under annealing at different temperatures. The figure shows that the divacancy concentration starts to decrease substantially when the annealing temperature is 120°C. The magnitude of absorption also decreases all over the investigated spectral region of the subgap for increasing annealing temperature. The divacancy peak disappears for the 210°C annealed sample, indicating that at about 200°C, the divacancy defects are completely annealed out which closely corresponds to the previously reported results [4]. However, the subgap absorption remains high even though themagnitude decreases progressively under annealing, which means that the concentration of defects other than divacancy is still high. This can be expected as the annealing temperature of 250°C is relatively low for Si [26]. So,
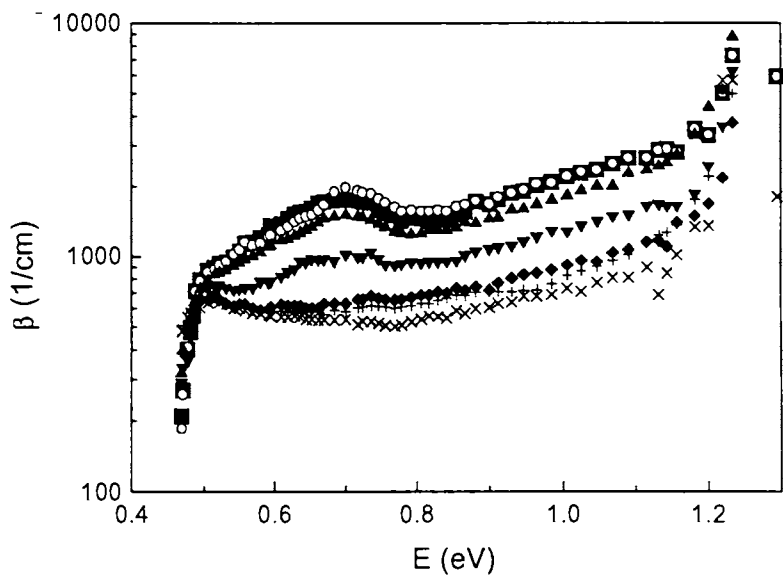
Fig. 4.11. Annealing temperature dependence of the subgap absorption in Si sample implanted at 300 K with a dose of 1×10^{16} cm^{-2}. ■ As implanted; O 120°C; ⊡ 160°C; ▫ 190°C; ◆ 210°C; + 230°C; × 250°C

in the present case, point defects, point defect complexes and other secondary defects produced under annealing are still present, resulting in considerable subgap absorption. It is known that defect evolution under annealing results in the formation of extended defects at higher temperature and much higher temperature of about 1000°C is required to anneal them out [27]. The excess absorption associated with the divacancy obtained as described before for different annealing temperatures is given in Fig.4.12. The divacancy concentration is extracted from this for different annealing temperatures. The

result is presented in Fig.4.13, in terms of relative divacancy concentration

which shows a sharp decrease as mentioned earlier. The E_0 value associated

with subgap absorption is also determined for different annealing temperatures

and presented in Fig.4.13. It is observed that E_0 increases as the annealing

temperature is increased. This is in contrast with the behaviour shown in Si

implanted with heavier ions [4]. This difference indicates that when there is no

amorphous zone formed with light ion implantation at 300 K, the nature of the

defects formed and and their evolution under annealing are different from that

for the case of implantation with heavier ions. So the defects and defect

complexes evolved and the strain in the material associated with the

intermediate stages during the annealing are different in the case of B^- ion

implantation.

Effect of annealing is also investigated in the amorphous layer with

sample implanted at 80 K with dose 1×10^{16} cm^{-2}, in which case, a completely

amorphous layer is formed. Fig.4.14 shows the subgap spectral evolution,

relative to the as-implanted sample, under isochronal annealing for increasing

temperatures upto a maximum value of 450°C. The spectra corresponding to

some of the intermediate annealing temperatures are not shown in the figure

for clarity. It is observed that the subgap absorption decreases all over the

investigated spectral range with a sharpening of the absorption profile resulting

in a decrease in the inverse - logarithmic slope parameter E_0, even as the
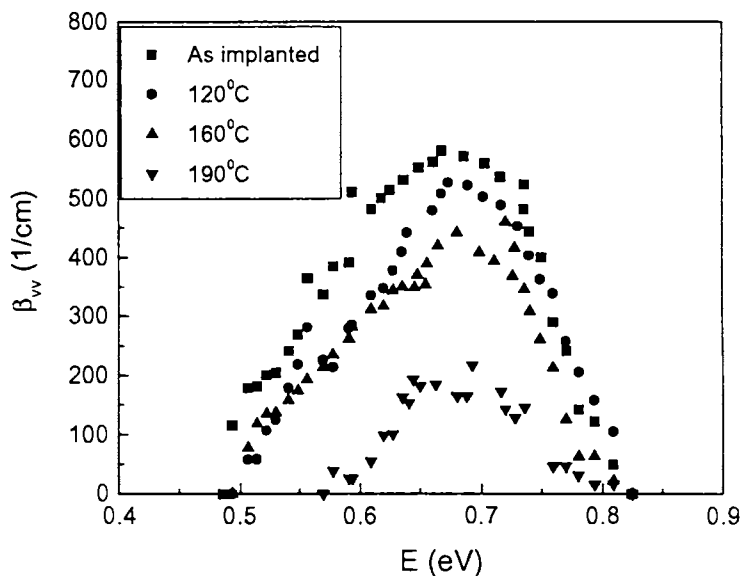
Fig. 4.12. Annealing temperature dependence of the divacancy absorption band of Si sample implanted at 300 K with a dose of 1×10^{16} cm^{-2}

implanted layer remains completely amorphous. Such a behaviour of amorphous silicon network is associated with structural relaxation taking place in the disordered network [28]. E_0 values determined for different annealing temperatures are shown in Fig.4.15 which shows a decrease in E_0 with increase in annealing temperature. It has been reported that fully relaxed amorphous silicon shows an E_0 value of ≈ 0.14 eV. The present data shown in Fig.4.15 also shows a similar trend.

The exponential absorption edge is related to the band tail states which

in turn is related to network disorder. The sharpening of the band edge and consequent reduction in E_0 suggests that the network readjustment towards relaxed state is happening progressively during annealing leading to a completely relaxed amorphous state. It has been reported that such a process can be ascribed to reduction of strain in the material [29] which can be associated with readjustment in bond angle and bond length in the amorphous network itself. It is possible that such a process is driven by a defect annealing
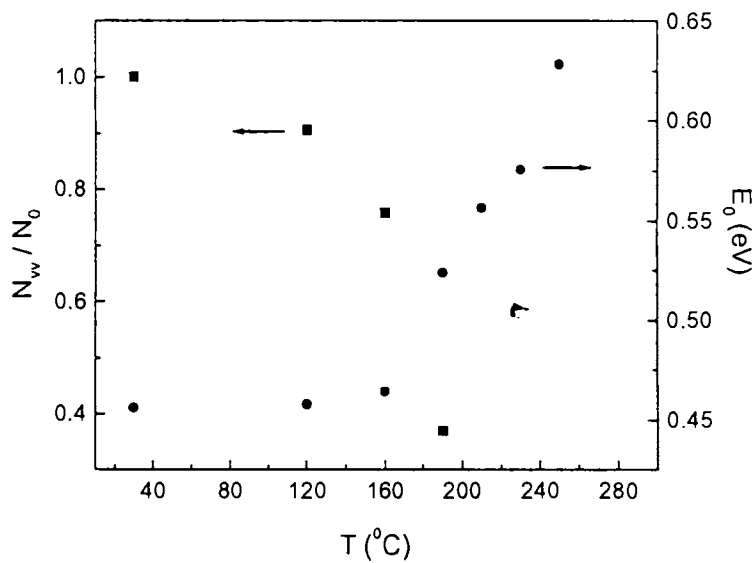
Fig. 4.13. Annealing temperature dependence of the relative concentration of divacancies and inverse logarithmic slope parameter of Si sample implanted at 300 K with a dose of 1×10^{16} cm^{-2}
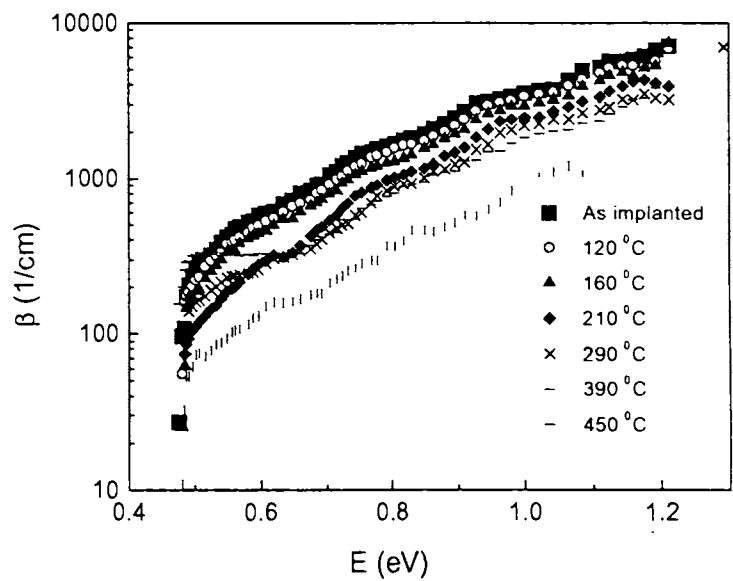
Fig. 4.14. Annealing temperature dependence of the subgap absorption in amorphous Si layer produced by 80 K B$^+$ ion implantation
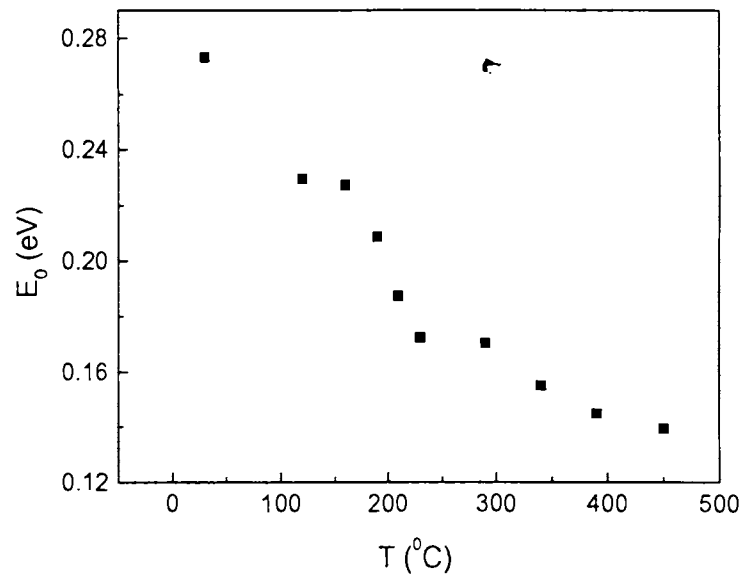

Fig. 4.15. Annealing temperature dependence of E$_o$ in amorphous Si layer

mechanism. The structural relaxation and strain reduction process in ion implanted a-Si has been investigated by a variety of techniques [9,30]. These investigations suggested that the structural relaxation in ion implanted a-Si is related to mutual annihilation of point defects and point defect complexes with consequent reduction in bond angle distortion and strain in the material.

4.4. Conclusions

Effect of light ion implantation in Si is studied using B^+ ion implantation. The subgap optical absorption measurement by Photothermal Deflection Spectroscopy (PDS) is used for the investigations. The subgap absorption is measured as a function of ion dose and substrate temperature. The magnitude of optical absorption, divacancy concentration and inverse logarithmic slope E_0 obtained from absorption measurements are used for analyzing the results. It is found that the 300 K implanted samples do not undergo amorphization even at a dose of 1×10^{16} cm^{-2}. In the case of 80 K implanted sample, amorphization occurs at a dose of $\approx 10^{15}$ cm^{-2}. The dose and temperature dependence of the above parameters and their annealing induced changes are discussed in terms of the nature and evolution of defects in the case of a light ion like B^+ implantation in Si.

References

1. Emanuele Rimini, "Ion Implantation: Basics to Device Fabrication" (Kluwer Academic Publishers, 1994)

2. G.Carter and W.A.Grant, "Ion Implantation of Semiconductors" (Edward Arnold Publishers Ltd., 1976)

3. J.Narayan and O.W.Holland, J.Electrochem.Soc. **131** (1984) 2651

4. U.Zammit, K.N.Madhusoodanan, M.Marinelli, F.Scudieri, R.Pizzoferrato, and F.Mercuri, Phys.Rev.B **49** (1994) 14322

5. E.Wendler, K.Gartner, W.Wesch, U.Zammit and K.N.Madhusoodanan, Nuclear Inst.and Meth. in Phy.Research B **85** (1994) 528

6. N.Amer and J.D.Jackson, Semiconductors and Semimetals, vol. **21B** Ed: J.I.Pankove (Academic, New York, 1984)

7. K.L.Narasimhan and Shailendra Kumar, Ind.J.of Pure & Appl. Phys. **27** (1989) 390

8. T.Suzuki, H.Tamaguchi, S.Ohzono,and N.Natsuaki, 22nd International Conference on Solid State Devices and Materials, Sendai, 1990 (Business Center for Academic Societies Japan, Tokyo)

9 G.N.Van den Hoven, Z.N.Liang, and L.Niesen, Phys. Rev. Lett. **68** (1992) 3714

10. J.W.Corbett and G.D.Watkins, Phys.Rev. **138** (1965) 555

11. G.D.Watkins and J.W.Corbett, Phys.Rev.**138** (1965) A543

12. K.L.Brower, Radiat.Eff. **8** (1971) 213

13. Y.H.Lee and J.W.Corbett, Phys.Rev.B **8** (1973) 2810

14. Y.H.Lee, N.N.Gerasimenko and J.W.Corbett, Phys.Rev. **B 14** (1976) 4506

15. J.W.Corbett, "Radiation damage in Silicon and Germanium" in Proc.1st Int.Conf. on Ion Implantation, L.Chadderton and F.Eisen, Eds. Gordon and Breach, 1971, p.1-8

16. J.F.Gibbons, Proceedings of the IEEE, **60** (1972) 1062

17. P.M.Fahey, P.B.Griffin and J.D.Plummer,Rev.Mod.Phys. **61** (1989) 289

18. J.H.Svensson, B.G.Svensson, and B.Monemar, Phys.Rev.B **38** (1988) 4192

19. L.J.Cheng, J.C.Corelli, J.W.Corbett, and G.D.Watkins, Phys.Rev.**152** (1966) 761

20. H.Y.Fan and A.K.Ramdas, J.Appl.Phys. **30** (1959) 1127

21. L.J.Cheng and J.Lori, Phys. Rev. **171** (1968) 856

22. H.J.Stein, F.L.Vook, D.K.Brice, J.A.Borders and S.T.Picraux, Radiat.Eff.**6** (1970) 19

23. A.C.Boccara, D.Fournier, W.B.Jackson, and N.M.Amer, Opt. Lett. **5** (1980) 377

24. J.P.Biersack and L.G.Haggmark, Nucl. Instrum. Methods **174** (1980) 257

25. J.I.Pankove, Phys. Rev.**140** (1965) A2029

26. B.L.Crowder, J.Electrochem.Soc. **118** (1971) 943

27. K.S.Jones, S.Prussin, and E.R.weber, Appl.Phys.A **45** (1988) 1

28. U.Zammit, K.N.Madhusoodanan, F.Scudieri, and F.Mercuri, Phys.Rev.B

49 (1994) 2163

29. G.D.Cody, T.Tiedje,B.Abeles, and Y.Goldstein, Phys. Rev.Lett.**47** (1981) 1480

30. W.C.Sinke, T.Warabisaco, M.Miyao, T.Tokuyama, S.Roorda and F.Saris,

    J. Non-Cryst. Solids **99** (1988) 308

Chapter 5

Thermal diffusivity measurements of Ge_xSe_{100-x} and As_xSe_{100-x} thin films using photothermal beam deflection technique

This chapter outlines the results of thermal diffusivity measurements of the thin film samples of the glass systems Ge_xSe_{100-x} $(5 \leq x \leq 40)$ and As_xSe_{100-x} $(10 \leq x \leq 60)$ using PBD technique. For this, we have adopted the phase method, making use of the tangential (parallel) component of deflection signal based on the skimming configuration, where the probe beam grazes the sample surface. The experiment has been performed for two different modulation frequencies and the results are verified using the amplitude method. The variation of thermal diffusivity with composition for the two sets of samples has also been investigated and explained on the basis of structural changes taking place in the glass network with the change in composition.

5.1. Introduction

The determination of thermal parameters is an important method for characterizing materials. During the past few years, thermal wave physics has emerged as a valuable tool for the characterization and analysis of the material parameters [1-3]. The non-intrusive and non-destructive laser induced photothermal techniques such as probe beam deflection (PBD) and photoacoustic (PA) methods are widely used for the investigation of the thermal, transport and optical properties of semiconductors, ceramics, liquid crystals etc. [4-6]. Thermal diffusivity is an important thermo-physical parameter which is of direct importance in heat flow studies as it determines the rate of periodic or transient heat propagation through a medium. Its determination is often necessary because of its controlling effect and common occurrence in thermal conduction problems. Probe beam deflection technique or the mirage technique [7-9] being non-destructive and non-contact in nature, is found to be a powerful tool in thermal diffusivity measurements. The technique is based on the detection of thermal waves generated in a sample due to the absorption of an intensity modulated light beam (pump beam) and subsequent non-radiative relaxation. The thermal wave generated in the sample is propagated to the adjacent coupling medium and produces corresponding change in refractive index. This change in refractive index induces periodic deflection of another light beam (probe beam) grazing the sample surface. The mirage signal can be analysed

using various methods such as zero crossing technique [10,11], phase method [12], amplitude method [13] etc., among which we have adopted the phase method, making use of the tangential (parallel) component of deflection signal based on the skimming configuration, where the probe beam grazes the sample surface. The results are verified using the amplitude method.

5.2. Theory

Consider a radiation beam (pump beam), the intensity of which is modulated with frequency $\omega = 2\pi f$ using a chopper and then focussed to a tiny region of the sample surface. A 'thermal wave' is then generated in the sample. The thermal wavelength is defined as [10,14];

$$\lambda_{th} = 2\pi \left(\frac{2D}{\omega} \right)^{1/2} \tag{5.1}$$

where D is the thermal diffusivity.

The thermal diffusion length in the medium [2] (or reduced wavelength [15]) is the length to which heat diffuses at a particular frequency f and is given by,

$$\mu = \frac{\lambda_{th}}{2\pi} \tag{5.2}$$

The amplitude (A_t) and phase $(Arg [\theta_t])$ of the tangential component of the deflection signal is given by [16] as

$$\ln[A_t] = c - \frac{y}{l_t} \tag{5.3}$$

131

$$\text{Arg}[\theta_t] = \frac{y}{l_t} - \phi \tag{5.4}$$

where y is the pump-probe offset, c is a constant and l_t is the characteristic length, i.e; the distance corresponding to one radian shift. ϕ is a slowly varying function depending on pump-probe offset, pump beam spot size, height of the probe beam above the sample surface etc. For samples having high thermal diffusivity, the characteristic length is equal to the thermal diffusion length, $\mu = \sqrt{\dfrac{D}{\pi f}}$. Hence the slope of ln $[A_t]$ vs y and $\text{Arg}[\theta_t]$ vs y yields $\dfrac{1}{l_t}$ from which the thermal diffusivity of the sample can be calculated. The phase of the tangential component of the deflection signal varies linearly with the pump-probe offset. Thus, the phase method [12] consists of the evaluation of the linear slope of the phase versus pump-probe offset, whereas the amplitude method evaluates the slope of the linear relation between the natural logarithm of amplitude of the tangential component of the deflection signal and the pump-probe offset so that

$$D = \frac{\pi f}{(\text{slope})^2} \tag{5.5}$$

5.3. Experimental details

The details of sample preparation are given in chapter 3. A compact photothermal

132

beam deflection set up has been used for the measurements, the schematic diagram of which is shown in Fig.5.1. Fig.5.2. shows the photograph of the setup. The thin film sample is fixed in a glass cuvette of dimensions 10 mm x 10 mm x 50 mm. A He-Ne laser (20mW, λ = 6328 A^0) is used as the pump source. The pump beam is intensity modulated using a mechanical chopper (Stanford Research Systems, Model 450) and then focussed to a spot size of 80 μm onto the sample surface. A diode laser (5mW, λ = 6500 A^0) is used as the source of the probe beam which is focussed to a spot size of 40 μm, propagating perpendicular to the pump beam grazing the sample surface. The deflection is detected using a bi-cell (SPOT 2D) and is amplified using a low noise home-built pre-amplifier and is then fed to a lock-in-amplifier (Stanford Research Systems, Model 830) from which the amplitude and phase of the deflection signal is obtained. The probe laser, its focussing lens and the detector are fixed on a strong aluminium flat which in turn is mounted on an XYZ translator. This ensures the synchronous movement of the three while scanning the sample surface as well as considerable reduction of space consumption by making the experimental setup more simple and compact.

All the optomechanical components are fixed on an optical breadboard with honeycomb structure mounted on a vibration free granite table. This ensures the elimination of mechanical vibrations which is the source of the biggest noise contribution, thus increasing the accuracy of the experiment. The PBD setup is initially standardized by the measurement of the thermal diffusivity of indium

phosphide using carbon tetrachloride as the coupling medium for which the value

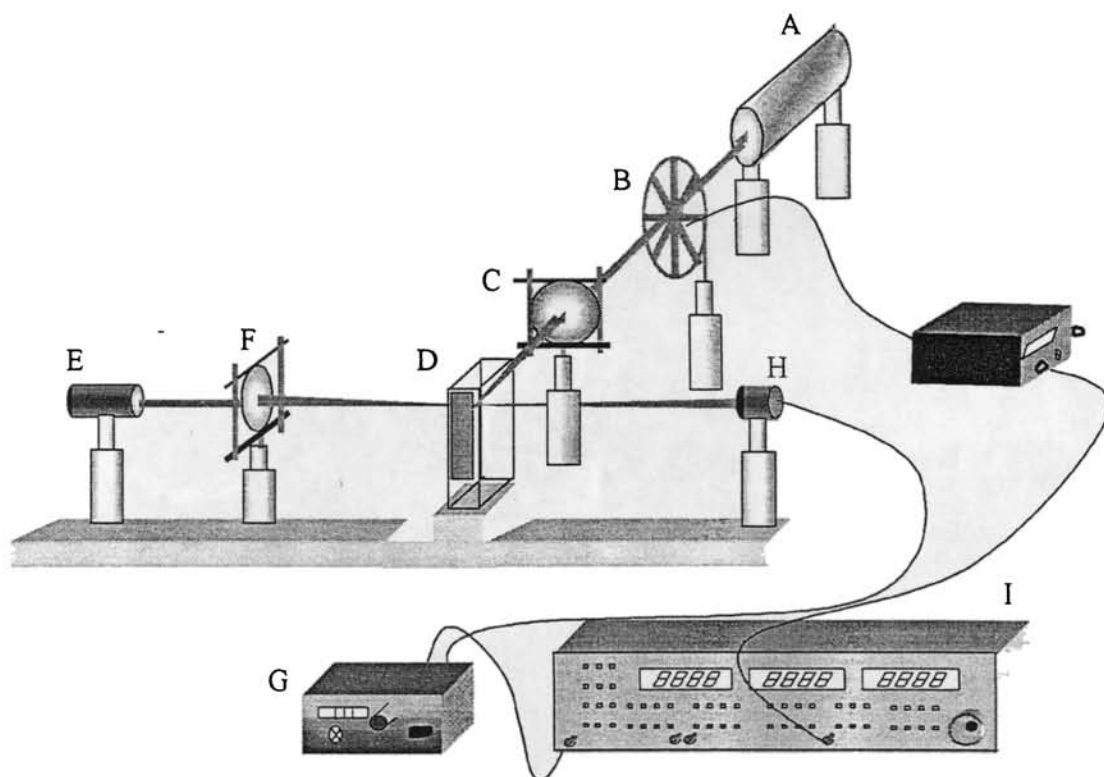obtained , 0.44 cm²s⁻¹ is found to agree with the reported value [17].

Fig 5.1. Schematic diagram of the PBD set up: A: He-Ne laser B: Mechanical chopper C: Focussing lens D: Sample cell (quartz cuvette 10 x 10 x 50 mm) E: Diode laser F: Focussing lens G: Pre-amplifier H: bi-cell I: Lock-in-amplifier

5.4. Results and Discussion

The plots of the variation of phase of the deflection signal versus the pump-probe

offset for a representative thin film sample of Ge_xSe_{100-x} are shown in Fig.5.3(a) and

Fig.5.3(b) for two different modulation frequencies 10 Hz and 11 Hz respectively,

while Fig.5.4(a) and 5.4(b) show the plots of the variation of natural logarithm of amplitude of the deflection signal versus the pump-probe offset for the same sample for the frequencies 10 Hz and 11 Hz respectively.
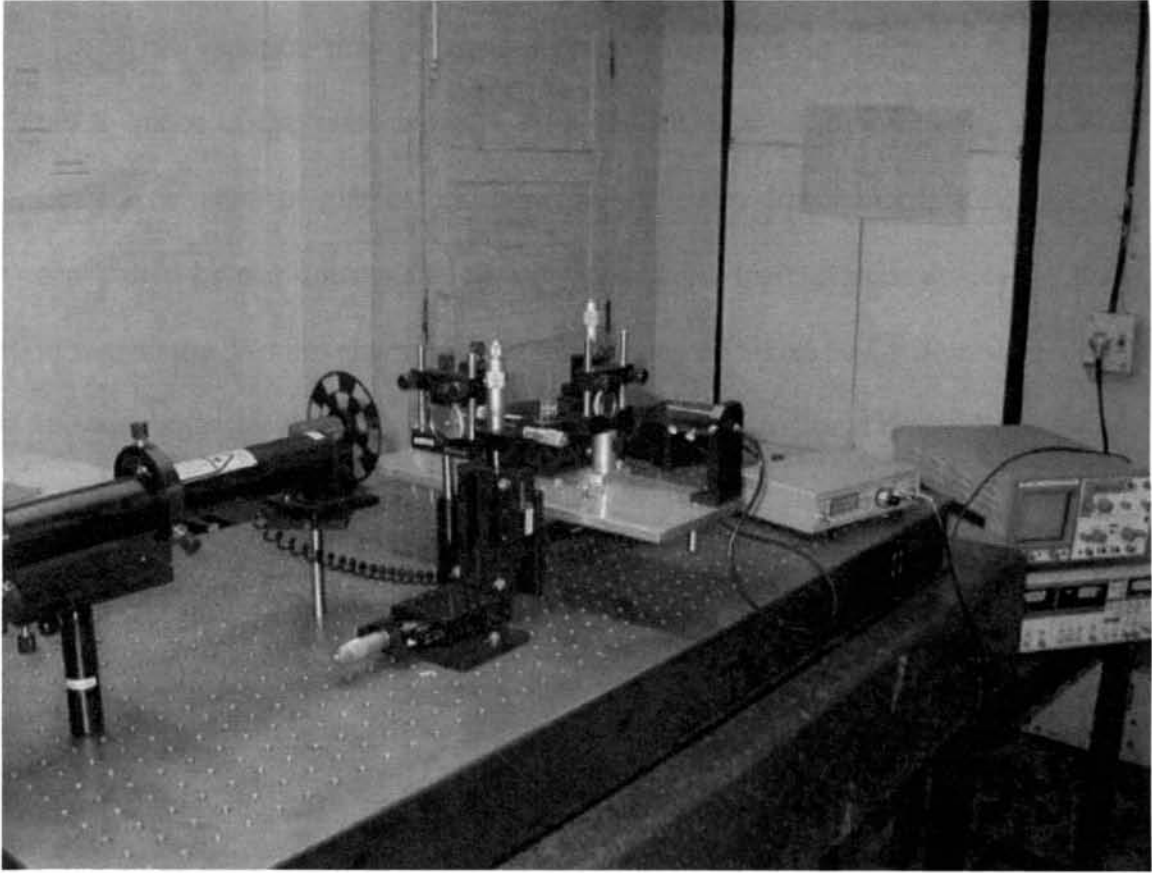

Fig.5.2 Photograph of the PBD setup

The thermal diffusivity values determined using the phase method and the amplitude method are given in Table 5.1. It may be observed that both the methods yielded nearly the same value and that the values for the different modulation frequencies also agree with each other. The variation of thermal diffusivity D as a

function of the composition parameter x is given in Fig. 5.5. It is found that D shows a peak value at the stoichiometric composition x = 33 corresponding to the chemical threshold of this system, while a discontinuous change is observed at x = 20.

This variation may be attributed to the changes in the short range order taking place in the glass network with the increase in concentration of Ge. In Ge_xSe_{100-x} system of glasses, the network with very low concentration of Ge is constituted by one dimensional Se atom chains. As the concentration of Ge atoms increases, the Se atom chain gets increasingly cross linked by Ge atoms. At x = 20, the one dimensional chain gets changed to a three dimensional network, attaining a stable structure consisting of $GeSe_4$ tetrahedral units. This stable structure offers relatively small resistance to the propagating thermal waves since the system contains small amount of disorder at this composition compared to other compositions. This accounts for the threshold peak in the thermal diffusivity value at this composition. The continuation of cross linking leads to the formation of fully connected random network of tetrahedral $Ge(Se_{1/2})_4$ units at the composition x =33, known as the stoichiometric composition of the system.

For the Ge_xSe_{100-x} glass system, two kinds of thresholds exist, one is the mechanical threshold which occurs at x=20, at which there occurs a threshold percolation of rigidity in the glass network. The other is the chemical threshold which occurs at x = 33, at which the system contains only Ge-Se bonds having higher bond enegy compared to Ge - Ge and Se - Se bonds. Thus, the observed
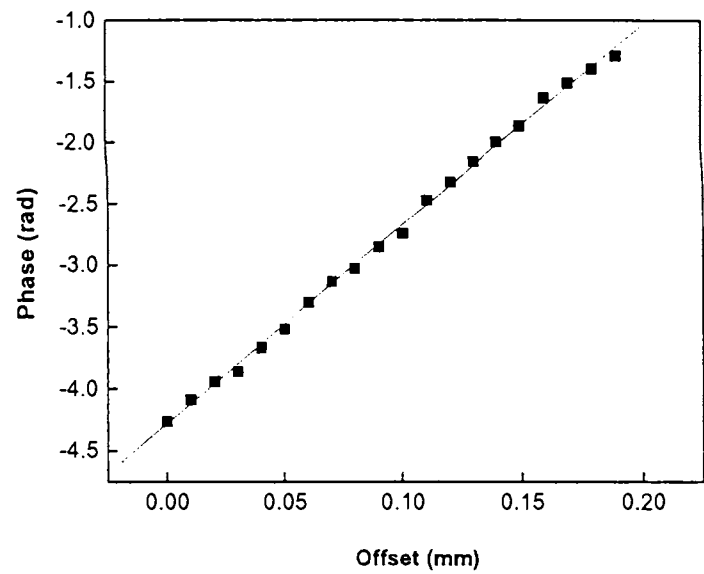
Fig.5.3.(a). Variation of phase of the deflection signal with the pump-probe offset at f=10Hz for a representative sample of Ge_xSe_{100-x}
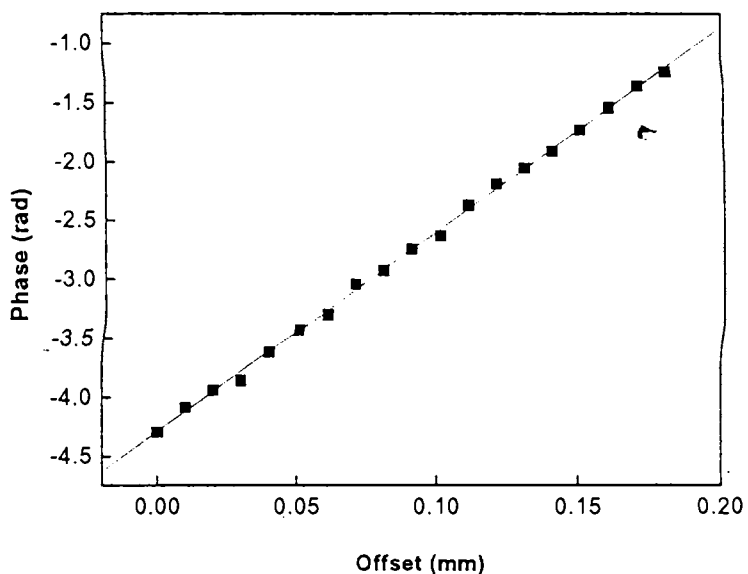

Fig.5.3.(b). Variation of phase of the deflection signal with the pump-probe offset at f=11Hz for a representative sample of Ge_xSe_{100-x}
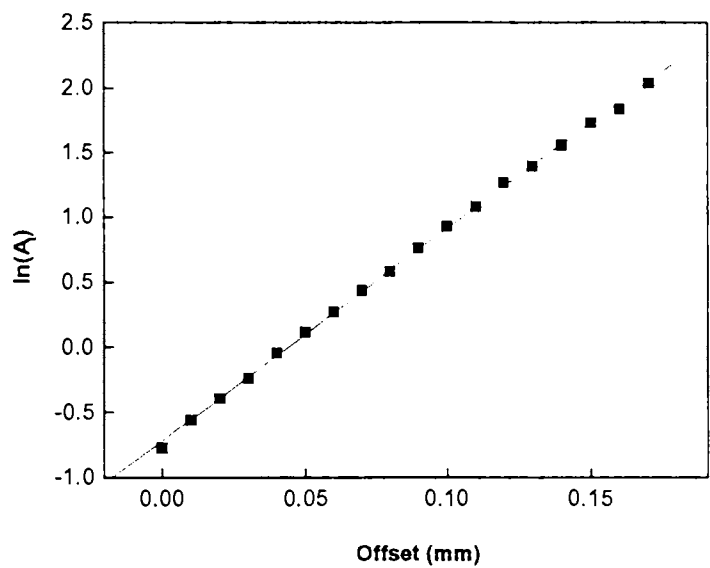
Fig.5.4.(a). Variation of natural logarithm of amplitude of the deflection signal with the pump-probe offset at f=10Hz for a representative sample of Ge_xSe_{100-x}

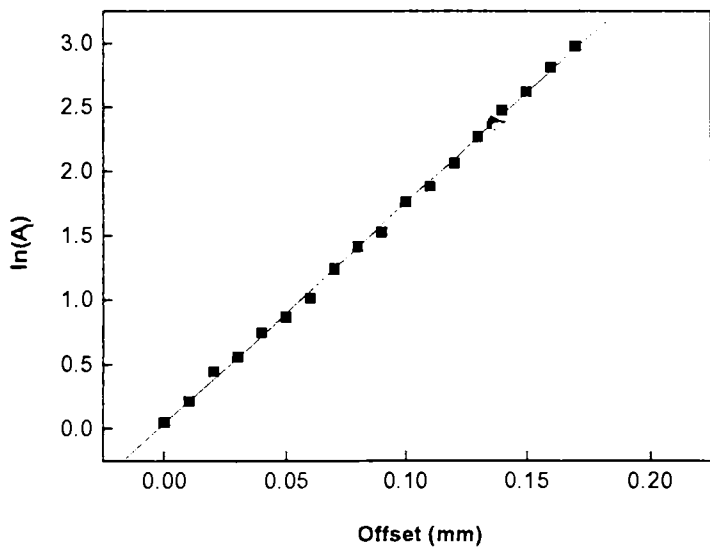**Fig.5.4.(b).** Variation of natural logarithm of amplitude of the deflection signal with the pump-probe offset at f=11Hz for a representative sample of Ge_xSe_{100-x}

Table 5.1. The thermal diffusivity values of Ge_xSe_{100-x} system determined using the phase method and the amplitude method

Sample	Method of Analysis	Frequency (Hz)	Slope (cm)	Thermal diffusivity D (cm^2s^{-1})	Mean D
Ge_5Se_{95}	Phase method	10	124	0.00204	
		11	129.81	0.00205	0.00205
	Amplitude method	10	123.99	0.00204	
		11	129.48	0.00206	
$Ge_{10}Se_{90}$	Phase method	10	98.59	0.00323	
		11	103.73	0.00321	0.00322
	Amplitude method	10	98.88	0.00321	
		11	103.25	0.00324	
$Ge_{15}Se_{85}$	Phase method	10	90.9	0.0038	
		11	94.96	0.00383	0.0038
	Amplitude method	10	91.2	0.00377	
		11	95.15	0.00381	
$Ge_{20}Se_{80}$	Phase method	10	83.79	0.00447	
		11	87.42	0.00452	0.0045
	Amplitude method	10	82.62	0.0046	
		11	88.6	0.0044	
$Ge_{25}Se_{75}$	Phase method	10	89.49	0.00392	
		11	94.11	0.00389	0.00391
	Amplitude method	10	89.82	0.00389	
		11	93.51	0.00395	
$Ge_{30}Se_{70}$	Phase method	10	97.69	0.00329	
		11	102.31	0.00329	0.00332
	Amplitude method	10	97.37	0.00331	
		11	100.79	0.0034	
$Ge_{33.3}Se_{66.7}$	Phase method	10	56.86	0.00971	
		11	57.69	0.01038	0.00994
	Amplitude method	10	56.32	0.0099	
		11	59.37	0.00979	
$Ge_{35}Se_{65}$	Phase method	10	61.99	0.00817	
		11	65.1	0.00815	0.00819
	Amplitude method	10	61.88	0.0082	
		11	64.7	0.00825	
$Ge_{40}Se_{60}$	Phase method	10	64.28	0.0076	
		11	66.27	0.00786	0.00775
	Amplitude method	10	63.86	0.0077	
		11	66.27	0.00786	

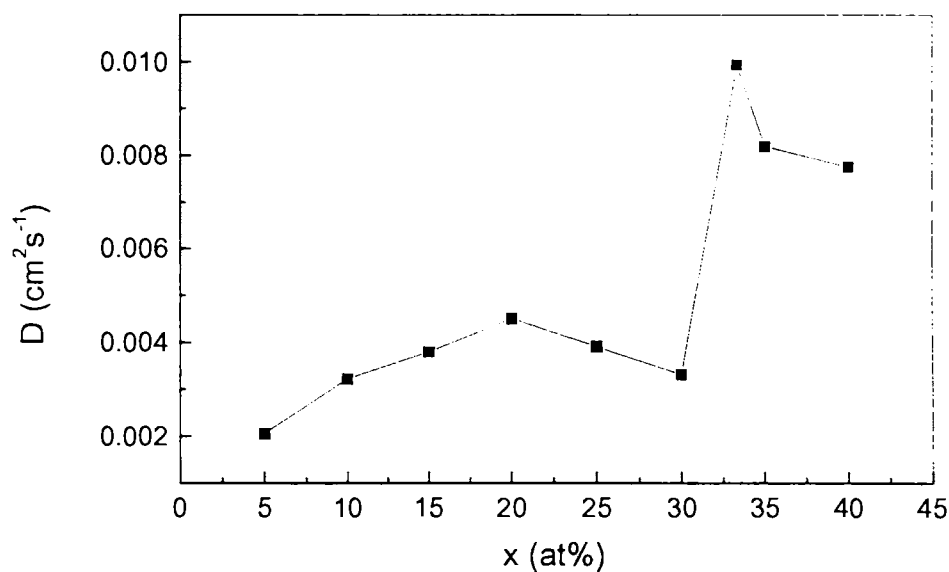**Fig.5.5.** Variation of thermal diffusivity as a function of the composition parameter x for Ge_xSe_{100-x} system

behaviour in the variation of thermal diffusivity with x may be attributed to the occurence of these two kinds of thresholds in the system. The results are not unexpected as there have been experimental reports on a wide variety of physical properties of Ge_xSe_{100-x} glass system exhibiting anomalous behaviour at x = 20 and x = 33. The measurement of the composition dependence of acoustic attenuation and velocity in Ge_xSe_{100-x} and Ge_xS_{100-x} glass systems by Gilroy and Phillips exhibit a low temperature peak in the attenuation for x = 20 and x = 33 [18]. Also, the studies of the composition dependence of several narrow Raman bands in Ge_xSe_{100-x} glass alloys by Murase et.al have reported a discontinuity near x = 20 composition [19].

The plots of the variation of phase of the deflection signal versus the pump-probe offset for a representative thin film sample of As_xSe_{100-x} are shown in Fig.5.6(a) and Fig.5.6(b) for two different modulation frequencies 10 Hz and 11 Hz respectively, while Fig.5.7(a) and 5.7(b) show the plots of the variation of natural logarithm of amplitude of the deflection signal versus the pump-probe offset for the same sample for the frequencies 10 Hz and 11 Hz respectively. The thermal diffusivity values determined using the phase method and the amplitude method are given in Table 5.2. It may be observed that both the methods yielded nearly the same value and that the values for the different modulation frequencies also agree with each other.

The variation of thermal diffusivity D as a function of the composition parameter x is given in Fig. 5.8. It is found that D increases with the increase in As content for x < 40 and decreases with the same for x > 40 ,hence giving a maximum value at x = 40. For the As_xSe_{100-x} system, x = 40 = x_c is known as the stoichiometric composition which corresponds to the chemical threshold of this system and the formation of the stoichiometric compound As_2Se_3. At the stoichiometric composition, the network is formed by fully connected $As(Se_{1/2})_3$ pyramidal structural units with minimum number of homopolar bonds like As-As and Se-Se. For x < x_c , the chemical order is maintained for As atoms, each of which is bonded to three Se atoms.The compositional variability is achieved by the Se atoms each of which is bonded to two Se atoms or to one Se and one As. For pure Se, the network
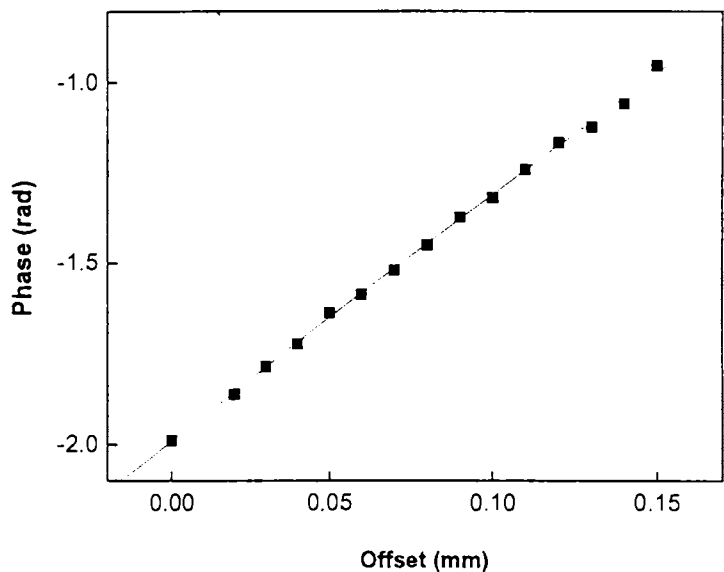
Fig.5.6.(a). Variation of phase of the deflection signal with the pump-probe offset at f=10Hz for a representative sample of As_xSe_{100-x}
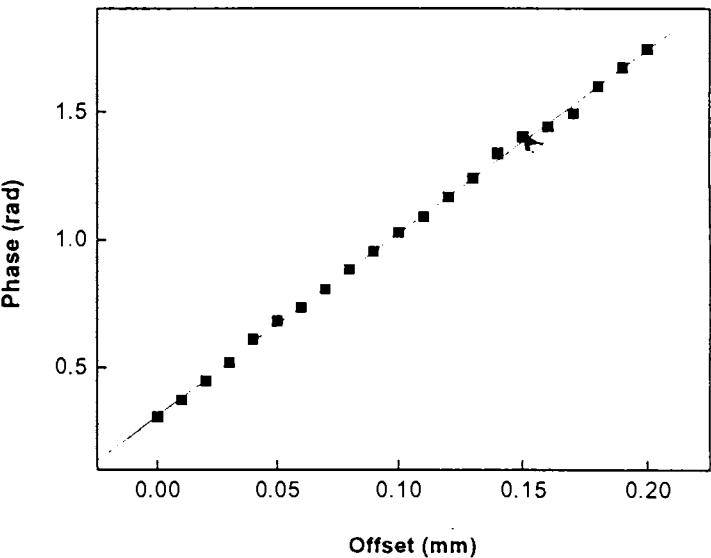

Fig.5.6.(b). Variation of phase of the deflection signal with the pump-probe offset at f=11Hz for a representative sample of As_xSe_{100-x}

142

Fig.5.7.(a). Variation of natural logarithm of amplitude of the deflection signal with the pump-probe offset at f=10Hz for a representative sample of As_xSe_{100-x}
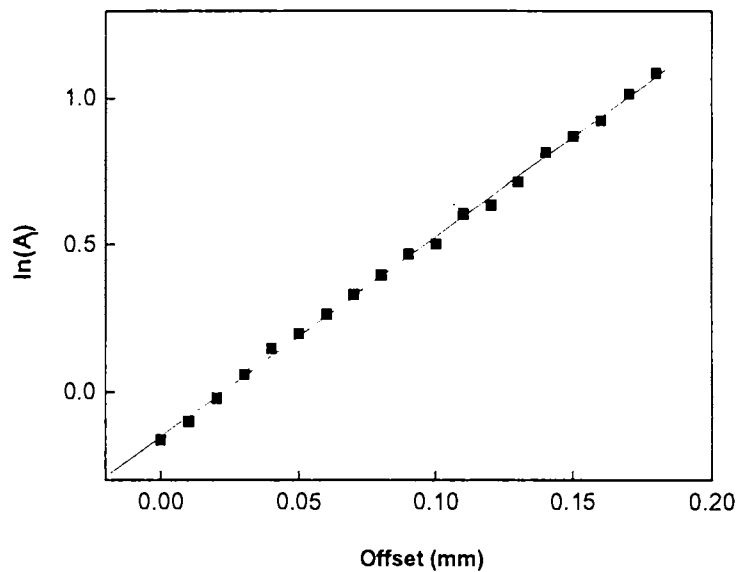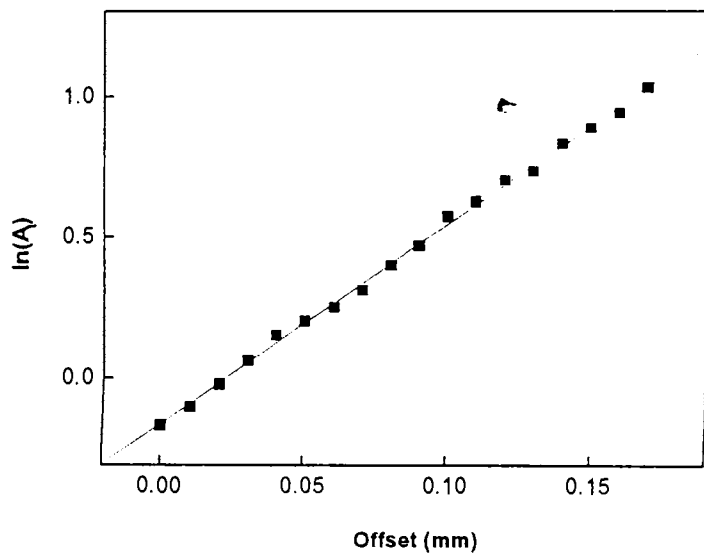

Fig.5.7.(b). Variation of natural logarithm of amplitude of the deflection signal with the pump-probe offset at f=11Hz for a representative sample of As_xSe_{100-x}

Table 5.2. The thermal diffusivity values of As_xSe_{100-x} system determined using the phase method and the amplitude method

| Sample	Method of Analysis	Frequency (Hz)	Slope (cm)	Thermal diffusivity D (cm^2s^{-1})	Mean D
$As_{10}Se_{90}$	Phase method	10	161.76	0.0012	
		11	171	0.00118	0.00119
	Amplitude method	10	162	0.00119	
		11	171.41	0.00118	
$As_{15}Se_{85}$	Phase method	10	121.7	0.00212	
		11	127	0.00214	0.00212
	Amplitude method	10	122	0.00211	
		11	127.5	0.00212	
$As_{20}Se_{80}$	Phase method	10	96	0.00341	
		11	100.79	0.0034	0.00343
	Amplitude method	10	95.92	0.00341	
		11	99.34	0.0035	
$As_{25}Se_{75}$	Phase method	10	79.79	0.00493	
		11	83.63	0.00494	0.00493
	Amplitude method	10	80	0.00491	
		11	83.70	0.00493	
$As_{30}Se_{70}$	Phase method	10	79.01	0.00503	
		11	83.12	0.00499	0.00501
	Amplitude method	10	79.21	0.005	
		11	82.92	0.00502	
$As_{40}Se_{60}$	Phase method	10	67.95	0.0068	
		11	71.34	0.00679	0.00685
	Amplitude method	10	68.03	0.00678	
		11	69.75	0.0071	
$As_{60}Se_{40}$	Phase method	10	73.55	0.0058	
		11	77.17	0.00579	0.00576
	Amplitude method	10	74	0.00573	
		11	77.63	0.00573	
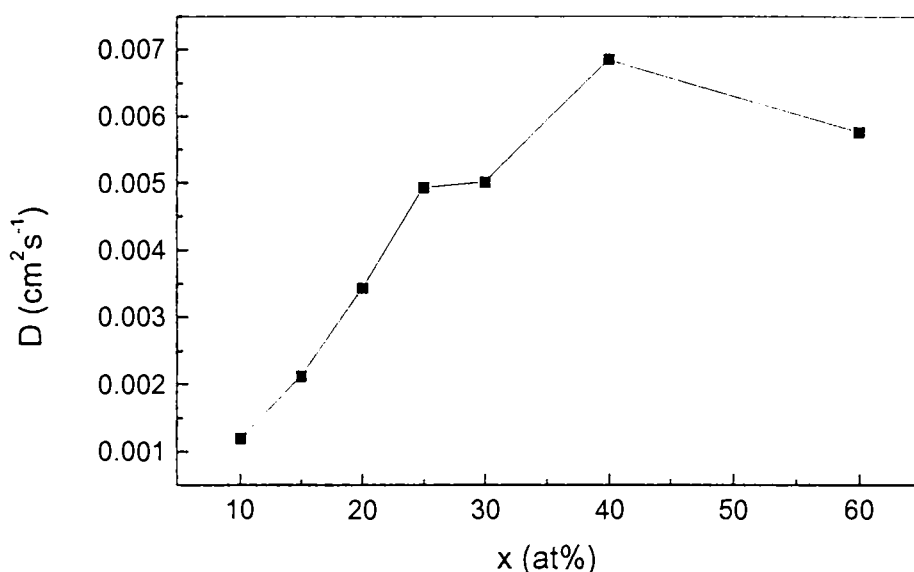
Fig.5.8. Variation of thermal diffusivity as a function of the composition parameter x for As_xSe_{100-x} system

dimensionality is one and the structural elements are extended chains. In Se rich glasses, the network is dominated by Se atom chains and the introduction of three fold coordinated As atoms produces branching or cross linking between Se chains. With this cross linking, the topologically linear $(Se)_n$ chains are interconnected at regular intervals to form large, highly connected structures. This process continues until x = 40 is reached, where fully connected glass with stable pyramidal $As(Se_{1/2})_3$ structural units is formed. At this composition, the disorder which causes the scattering of thermal phonons is minimum. This accounts for the peak value of thermal diffusivity at this composition. Beyond this, the network may contain other

basic structural units like As_4Se_4. As the value of x is varied from that corresponding to the compound composition, disorder in the network increases, which may be thought as responsible for the decrease of thermal diffusivity on either side of the stoichiometric composition. The observation is not unexpected as it has been experimentally established by observing the variation of several properties of As_xSe_{100-x} system as a function of composition that the critical composition corresponding to the stoichiometric compound commonly known as the chemical threshold of the glass occurs at x = 40 in the system at which unusual variations in various physical properties have been reported. Hurst and Davis have observed a minimum in the energy gap and a maximum in conductivity at the x = 40 composition [20]. Evidence for a medium range order in As_2Se_3 has been obtained from the existence of a first sharp diffraction peak corresponding to the formation of molecular clusters [21]. Raman shifts [22], glass transition temperature [23] and width of glass transition peaks [24] are also found to undergo anomalous variation at the compound composition.

5.5. Conclusions

Semiconducting amorphous Ge_xSe_{100-x} ($10 \leq x \leq 40$) and As_xSe_{100-x} ($10 \leq x \leq 60$) thin films are prepared by the technique of thermal evaporation onto glass substrates. Photothermal beam deflection technique has been employed for the measurement of thermal diffusivity (D) of these samples by determining the slope from the

tangential component of the deflection signal with the pump-probe offset. The

mirage signal is analysed using the phase method and the result of the

measurement is verified using the amplitude method, both of which have yielded

the same value of thermal diffusivity. The experiment was performed for two

different modulation frequencies and the values of D obtained for both were also

found to agree with each other. For Ge_xSe_{100-x} system, D was found to show a peak

value at the stoichiometric composition x = 33 corresponding to the chemical

threshold of this system, while a discontinuous change is observed at x = 20. For

As_xSe_{100-x} system, it is found that D increases with the increase in As content for

x < 40 and decreases with the same for x > 40, thus giving a maximum value at

x = 40. The observed variation is explained on the basis of structural changes taking

place in the glass network in both the systems.

References

1. A.Mandelis, "Photoacoustic and Thermal Wave Phenomena in Semiconductors" (North-Holland, New York, 1987)

2. A.Rosencwaig, "Photoacoustics and Photoacoustic Spectroscopy" (Wiley Interscience, New York, 1983)

3. Yu.G.Gurevich , G.Gonzalez de la Cruz, G.N.Logvinov and M.N.Kasyanchuck, Semiconductors **32** (1998) 1179

4. I.Reich, P.Diaz, T.Prutskij, J.Mendoza, H.Vargas and E.Marin, J.Appl.Phys. **86** (1999) 6222

5. S.Sankara Raman, V.P.N.Nampoori, C.P.G.Vallabhan, G.Ambadas and S.Sugunan, Appl.Phys.Lett. **67** (1995) 2939

6. N.A.George, C.P.G.Vallabhan, V.P.N.Nampoori, A.K.George and P.Radhakrishnan, J.Phys.D: Cond.Matt **13** (2001) 365

7. J.C.Murphy and L.C.Aamodt, J.Appl.Phys. **51(9)** (1980) 4580

8. L.C.Aamodt and J.C.Murphy, J.Appl.Phys. **52(8)** (1981) 4903

9. L.C.Aamodt and J.C.Murphy, J.Appl.Phys. **54(2)** (1983) 581

10. P.K.Kuo, M.J.Lin, C.B.Reyes, L.D.Favro, R.L.Thomas and D.S.Kim, Can.J.Phys. **64** (1986) 1165

11. P.K.Kuo, E.D.Sendler, L.D.Favro and R.L.Thomas, Can.J.Phys. **64** (1986) 1168

12. M.Bertolotti and R.Li Voti, Rev.Sci.Instrum. **64(6)** (1993) 1576

13. X.Quelin, B.Perrin, G.Louis and P.Peretti, Phys.Rev.B **48** (1993) 3677

148

14. A.Rosencwaig, Science **218** (1982) 223

15. G.Busse and A.Rosencwaig, Appl.Phys.Lett. **36** (1980) 815

16. A.Skumanich, H.Dersch, M.Fathallah and N.M.Amer, Appl.Phys. A **43** (1987) 297

17. M.Bertollotti, V.Dorogan, G.Liakhou, R.Li Voti, S.Paolini and C.Sibilia, Rev.Sci.Instrum. **68(3)** (1997) 1521

18. K.S.Gilroy and W.A.Phillips, Phil.Mag.B **47** (1983) 655

19. K.Murase, T.Fukunaga, K.Yakushiji, T.Yoshimi and I.Yunoki, J.Non-Cryst.Solids **59** (1983) 885

20. C.H.Hurst and E.A.Davis, Int.Conf. on Amorphous and Liquid Semiconductors, Garmisch, September, 1973

21. A.A.Vaipolin and E.N.P. Koshits, Sov.Phys.Solid State **5** (1963) 186

22. R.J.Nemanich, G.A.N.Connell, T.M.Hayes and R.A.Street, Phys.Rev.B **18** (1978) 6900

23. M.B.Myers and E.J.Felty, Mater. Res.Bull. **2** (1967) 535

24. J.C.Phillips, Phys.Today **35** (1982) 27

Chapter 6

Optical absorption studies in nitrogen implanted Ge_xSe_{100-x} and As_xSe_{100-x} thin films

This chapter reports the results of the optical absorption measurements by PDS in nitrogen implanted thin film samples of Ge-Se and As-Se systems. The profiles of the ion range and vacancy distribution are obtained by the TRIM simulation. The variations of optical band gap and inverse logarithmic slope with implantation for the different compositions of the samples are investigated and are explained on the basis of structural changes taking place in the network due to ion bombardment.

6.1. Introduction

Amorphous chalcogenide semiconductors form an important class of materials with great potential as electronic and optoelectronic materials[1, 2]. These materials exhibit several interesting physical properties different from that of tetrahedrally coordinated amorphous semiconductors like a-Si[3]. The origin of such differences are related to the difference in network structure, presence of lone pair electrons and the nature of coordination defects. Tetrahedrally coordinated materials are known to be overconstrained with coordination 4 whereas amorphous chalcogenides have relatively lower average coordination in the range between 2 and 3 depending on composition[4]. Such lower average coordination offers large network flexibility allowing the possibility for different topological configurations. The electronic properties of chalcogenides are influenced by the presence of lone pair states which generally form the valence band. The distribution of these states are sensitive to network disorder like bond angle and bond length variations. The coordination defects in a-Si like materials are mostly dangling bonds whereas in chalcogenides, valence alternation pairs of triply coordinated C$^+$ and single coordinated C$^-$ defects constitute the coordination defects[5, 6]. The structural and electronic features lead to interesting properties like photodarkening, photobleaching, non-linear optical response etc.[7]. The electronic density of states associated with structural and coordination defects in these materials result in optical

absorption in subgap region over a wide wavelength range. As this defect related absorption is closely associated with many of the physical effects in chalcogenides, it is interesting to study the optical absorption when the defect configuration is modified by techniques like ion implantation. In the present study, we have carried out such an investigation using a relatively low dose of 10^{14} cm^{-2} nitrogen ion implantation in Ge-Se and As-Se samples. The dose is kept low so that there is no appreciable chemical change due to incorporation of nitrogen and the effect is restricted only to network disorder. With the present dose, the nitrogen concentration will be less than 0.01%. It may be noted that the effects of impurities on the electronic properties of chalcogen-based amorphous semiconductors have been controversial ever since their discovery[8]. Earlier studies showed that they are insensitive to various added impurities. More experiments revealed that some added impurity atoms in large concentrations may be situated at sites with unusual configurations. These sites do not allow them to satisfy their valencies and can therefore behave in an electrically active manner leading to donor-like or acceptor-like behaviour [9, 10].

From the point of view of implantation induced disorder, we have investigated the optical absorption in model amorphous chalcogenide semiconductors Ge$_x$Se$_{100-x}$ ($5 \leq x \leq 40$) and As$_x$Se$_{100-x}$ ($10 \leq x \leq 50$), which are implanted with low dose nitrogen ions, over a wide range of wavelength using

152

Photothermal Deflection Spectroscopy (PDS). PDS is a powerful technique for the measurement of weak absorption even for thin film samples where absorption length is small [11, 12]. Therefore it is well suited for absorption measurement over a wide range in amorphous semiconducting thin films.

6.2. Experimental Details

The details of preparation of thin film samples of Ge$_x$Se$_{100-x}$ and As$_x$Se$_{100-x}$ glass systems are given in chapter III. Thickness of the films is in the range 4000 to 5000 A^0. Optical absorption measurements over a wide range of wavelength were done using PDS technique. The set up consists of a 1KW Xe- lamp as source, He-Ne probe beam, position sensor, lock-in amplifier and a set up for online normalization of the spectrum. The absorption coefficient values are deduced from the PDS data in relation with the saturation in the spectrum from the relation [13]

$$\frac{S}{S_{sat}} = 1 - \exp(-\beta l) \tag{6.1}$$

where S is the wavelength dependent PDS signal, S$_{sat}$ is the saturation signal, l is the thickness of the film and β, the absorption coefficient.

The thin film samples were implanted with nitrogen ions with multiple energy in the range 50 to 150 KeV to a total dose of 10^{14} cm^{-2}, according to the scheme proposed by TRIM simulation. The chosen energies give an approximately homogeneous distribution of ions and defects over the thickness

of the sample film. The densities of $GeSe_2$ and As_2Se_3 were considered for simulation. Composition dependent variation of density was not considered as the change in simulated pattern is negligible. The profiles of ion range and vacancy distribution obtained by TRIM simulation are given in Figs. 6.1 and 6.2 respectively for Ge-Se samples and in Figs. 6.3 and 6.4 respectively for As-Se samples. Optical absorption measurements were carried out in both implanted and unimplanted samples of all the compositions belonging to both Ge-Se and As-Se systems. The higher sensitivity of PDS technique is made use of to record the spectrum over a wide range of wavelength extending down to the weak absorption region.

6.3. Results and Discussion

A. Results on Ge_xSe_{100-x} System

Fig.6.5 shows the optical absorption spectrum obtained from PDS measurement for a representative sample for both unimplanted and implanted cases. The general feature in the absorption spectrum of all the samples is the presence of three absorption regions. One corresponds to high absorption with $\beta \geq 10^4$ cm^{-1}, the second region which shows an exponential behaviour with 10^2 cm$^{-1} \leq \beta \leq 10^4$ cm^{-1} and a third low absorption region with $\beta < 10^2$ cm^{-1} corresponding to higher wavelength. The high absorption region corresponds to absorption
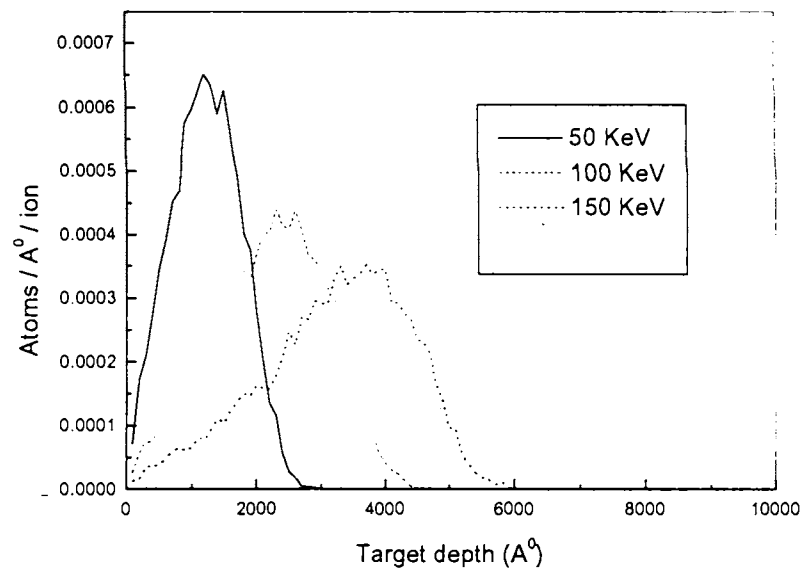
Fig.6.1. Simulated ion range profile for nitrogen ions implanted into Ge-Se system. The density of GeSe$_2$ is used for simulation.
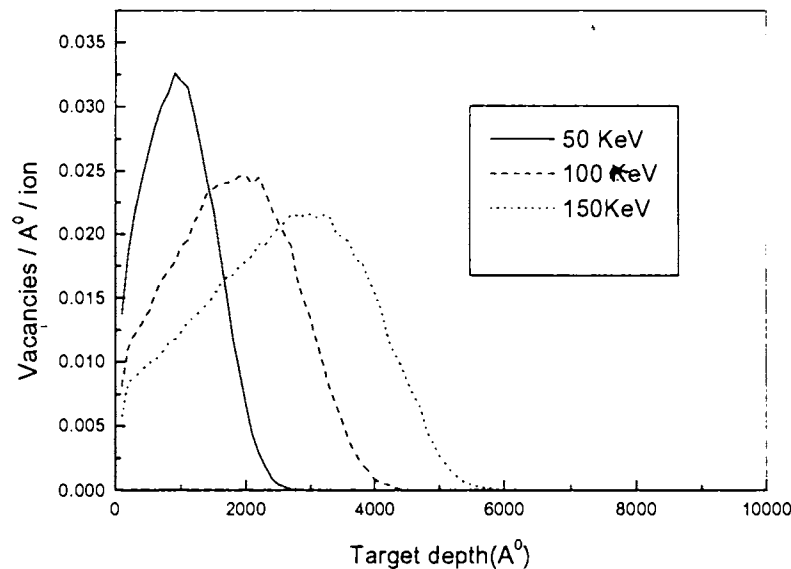

Fig.6.2. Simulated vacancy distribution profile for nitrogen ions implanted into Ge-Se system.
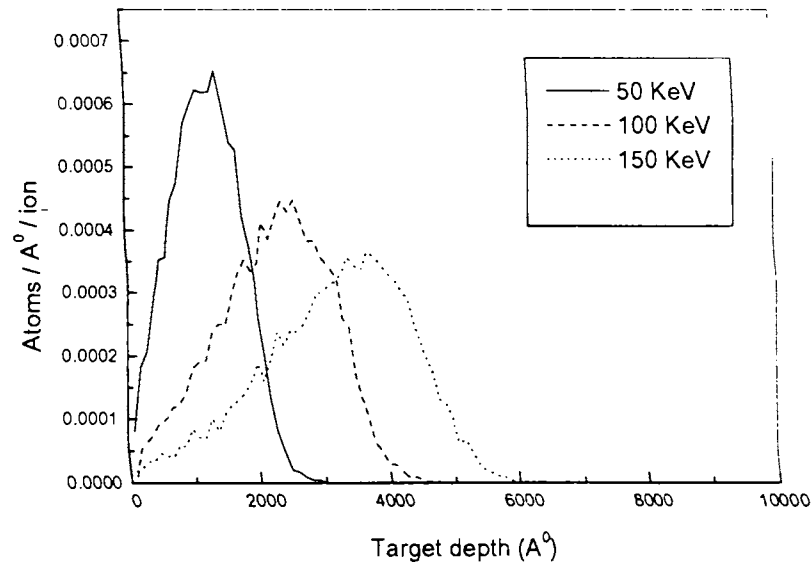
Fig.6.3. Simulated ion range profile for nitrogen ions implanted into As-Se system. The density of As_2Se_3 is used for simulation.
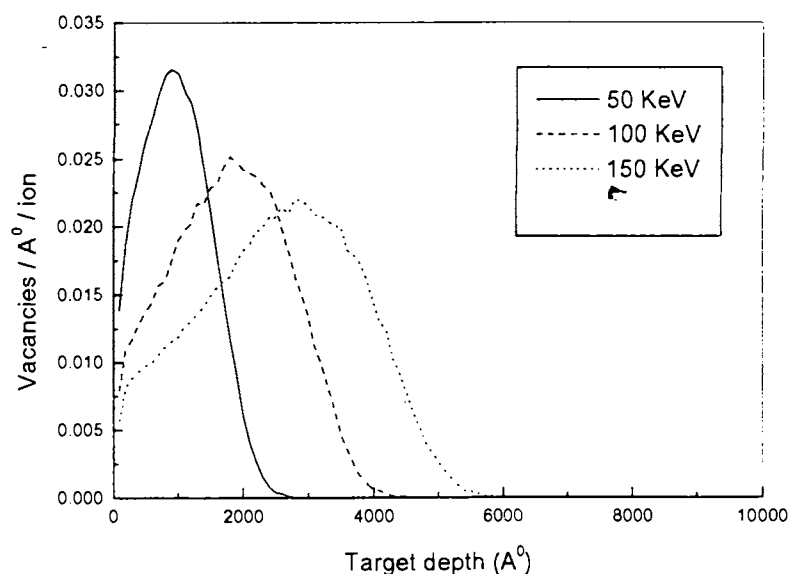

Fig.6.4. Simulated vacancy distribution profile for nitrogen ions implanted into As-Se system.

involving valence band and conduction band. Assuming parabolic bands, optical energy gap E_g can be determined from absorption data in this region using conventional Tauc's plot in which $(\beta h\nu)^{1/2}$ Vs $h\nu$ is plotted[14]as shown in Fig.6.6. The absorption then follows the relation $\beta h\nu \propto (h\nu - E_g)^2$[15]. The absorption data in the high absorption region below the saturation is fitted to straight line and the intercept on hv axis is taken as the optical gap E_g. The E_g values for all the Ge-Se samples for both the unimplanted and implanted cases were estimated in this way. The absorption in the region below E_g depends on the distribution of band tail states, especially that of valence band tail. These states are associated with the network structural disorder mainly arising from bond length and bond angle variations. The absorption in this region has an exponential dependence on the incident energy represented by $\beta = \beta_0 \exp(h\nu/E_0)$. The inverse logarithmic slope E_0 for this region characterizes the network disorder in the sample[16]. This parameter has been obtained for all the samples by fitting the absorption data in the band edge region (i.e; below E_g) with such an exponential dependence as shown in Fig.6.5. The subgap absorption deviates from the exponential behaviour in the low absorption region as observed previously for the case of a-Si. In this region, the absorption is associated with localized states in the gap which arise due to coordination defect centers.
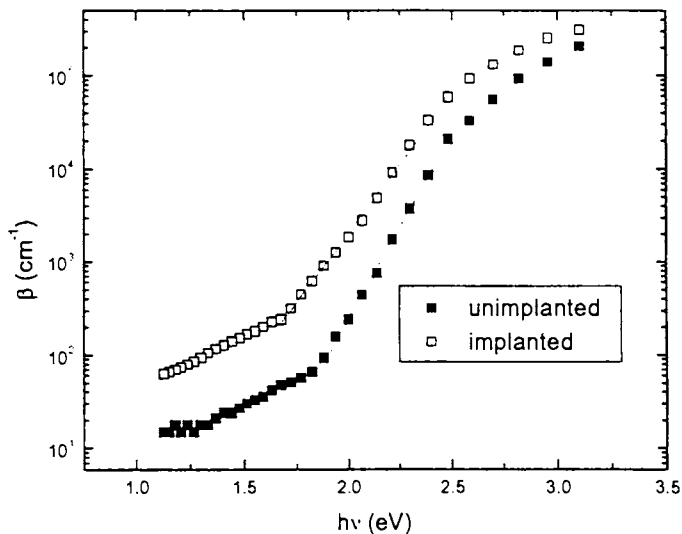
Fig.6.5. The optical absorption spectrum for a representative sample of Ge-Se system (Ge$_{33}$Se$_{67}$) for both unimplanted and implanted cases (The straight lines show the fits to the exponential absorption regions which are used to determine E$_0$)
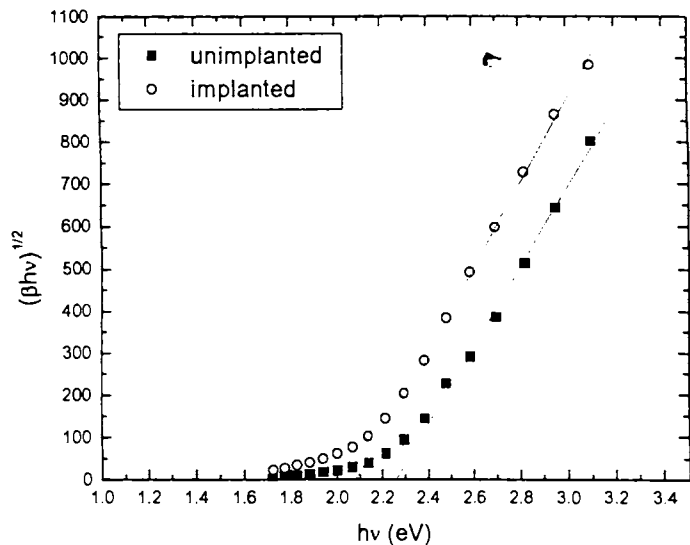

Fig.6.6. The determination of optical energy gap(E$_g$) for a representative sample of Ge-Se system (Ge$_{33}$Se$_{67}$) using Tauc's plot

The variation of optical energy gap E$_g$ obtained as described above using absorption data in the high absorption region is given in Fig.6.7 for Ge-Se samples. It may be noted that the E$_g$ values obtained for the unimplanted samples are comparable to the values reported in the results of optical absorption measurements of the same samples presented in chapter 3. The small difference in values is associated with the relative inaccuracies involved in the two methods. The E$_g$ value increases with x and shows a maximum for x = 33 which is the stoichiometric composition. This behaviour is the same for implanted and unimplanted samples. However, in the case of implanted sample, the E$_g$ value is smaller than that of unimplanted samples for all the compositions. Similar composition dependence for E$_g$ has been reported for bulk Ge-Se glasses[17]. The composition dependence can be explained using the chemically ordered network model[18] which suggests an extremum for the physical properties for stoichiometric composition[19] and the relative bond energy of the various bonds. Depending on composition, the Ge-Se system can have three possible types of bonds, i.e; Se-Se (44 K Cal/ mole), Ge-Ge (46.5 K Cal/ mole) and Ge-Se (49.1 K Cal/ mole) bonds in the order of increasing bond energies [20]. When x is small, the amorphous network mainly consists of Se-Se chain. As x increases, these chains are increasingly interlinked with the four fold coordinated Ge with the formation of Ge-Se bonds. The average bond energy increases as the number of Ge-Se bonds increases when x increases. This

results in an increase in the optical energy gap E_g. At the stoichiometric composition, the network in principle has only Ge-Se bonds with maximum average bond energy and correspondingly maximum E_g. When x > 33, the system will contain Ge-Se and Ge-Ge bonds which will again reduce the average bond energy. The variation in E_g follows the above description. However it is possible that small number of different types of homonuclear bonds will be present at different concentrations. The E_g values for implanted samples is found to be smaller compared to the unimplanted samples. This is due to the presence of larger amount of network disorder in the network, as well as the possible wrong homonuclear bonds introduced by the implantation process. This leads to widening of the band edge into the gap region, thus reducing the gap.

The variation of inverse logarithmic slope E_0 as a function of composition index x for Ge-Se samples is given in Fig.6.8 for both implanted and unimplanted samples. E_0 increases with x and reaches a maximum for the stoichiometric composition with x = 33. E_0 variation, being sensitive to the network disorder and the band edge states associated with it, indicates that network disorder increases with increased cross linking of the network with the increase in x or in other words, when the network flexibility decreases. The value of E_0 shows a maximum for the stoichiometric composition which also
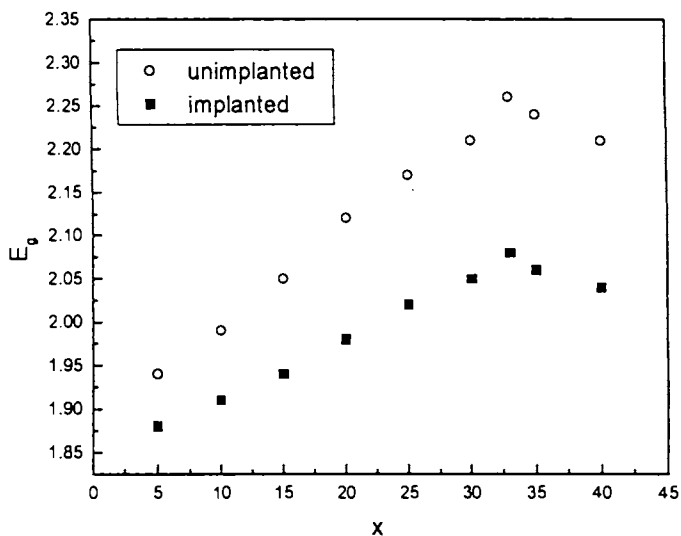
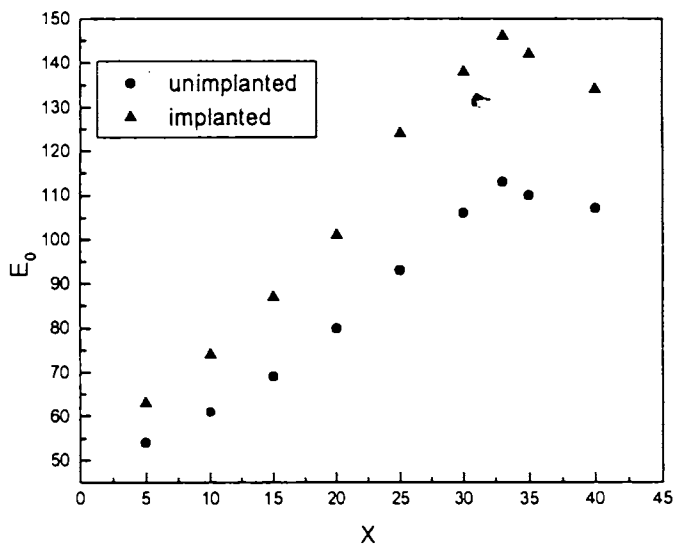Fig.6.7. The variation of optical energy gap (E_g) with composition index x for thin film samples of Ge_xSe_{100-x}

Fig.6.8. The variation of inverse logarithmic slope (E_0) with composition index x for thin film samples of Ge_xSe_{100-x}.

has a relatively high average coordination (2.67). In comparison to this, the coordination in a - Si which has an overconstrained network is 4 and it shows generally high value for E_0 [21, Refer Chapter 4]. Thus, the coordination and the network flexibility play an important role in determining the network disorder. In the case of implanted Ge-Se samples, the E_0 values are found to be higher for all the compositions compared to unimplanted samples. The implantation results in more network disorder which increases the absorption in the subgap region as well as the E_0 values. The composition dependence of E_0 shows similar variation as in the case of unimplanted samples, with the rate of increase higher for larger x values in the range x < 33. This suggests that the overall coordination corresponding to each x remains same and only the network disorder varies. This is in agreement with the variations in E_g which shows similar composition dependence for implanted and unimplanted samples with a relatively smaller E_g for implanted samples. So, it can be concluded that the increased network disorder results in increased lone pair interaction leading to widening of the valence band and a decrease in E_g.

B. Results on As_xSe_{100-x} System

The optical absorption spectrum for a representative As-Se system $As_{40}Se_{60}$ is given in Fig.6.9 for the implanted and unimplanted cases. The optical energy gap is determined from Tauc plot (Fig.6.10). The inverse logarithmic parameter is also determined as shown in Fig.6.9. The results for the E_g and E_0 variation as
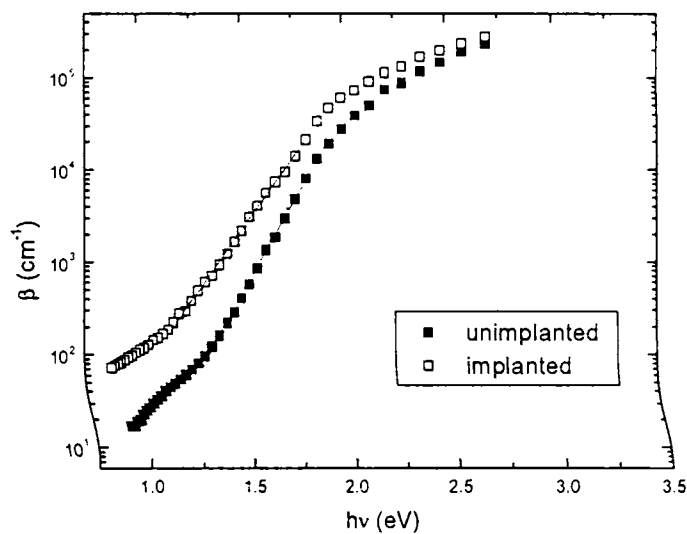
162

Fig.6.9. The optical absorption spectrum for a representative sample of As-Se system (As$_{40}$Se$_{60}$) for both unimplanted and implanted cases (The straight lines show the fits to the exponential absorption regions which are used to determine E$_0$)
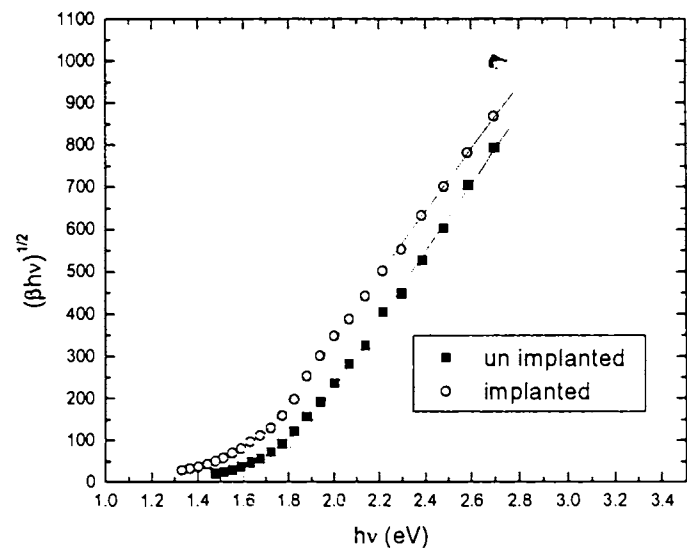

Fig.6.10. The determination of optical energy gap(E$_g$) for a representative sample of As-Se System (As$_{40}$Se$_{60}$) using Tauc's plot

a function of composition parameter x for As-Se samples is given in Fig.6.11

and Fig.6.12 respectively. It may be noted that the E_g values obtained for the

unimplanted samples are in close agreement with those reported in the results

of optical absorption measurements of the same samples presented in chapter 3.

In this case, E_g decreases with x and shows a minimum at the stoichiometric

composition with x = 40. Similar behaviour has been reported earlier[22]. These

results may also be considered on the basis of chemically ordered network

model and lone pair interaction. In such a model, the three different types of

bonds in this system are Se-Se, As-Se, and As-As, bonds with excess Se-Se

bonds present for x < 40, excess As-As bonds for x > 40 and at x = 40, the system

contains maximum number of As-Se bonds. The bond energies of Se-Se, As-Se,

and As-As bonds are 44, 44.96 and 43.4 K Cal/mole respectively[20]. These

values being very close, the variation in average bond energy with composition

alone cannot explain the composition dependence of E_g. However, it may be

noted that both As and Se have lone pair electrons and thus the variation in

lone pair interactions as the composition varies is playing an important role.

The optical energy gap in the entire composition range is associated with lone

pair to antibonding transitions. As the coordination increases with increase in x,

(average coordination increases from 2 to 2.4 when x changes from 0 to 40), the

increased lone pair interaction results in widening the valence band and

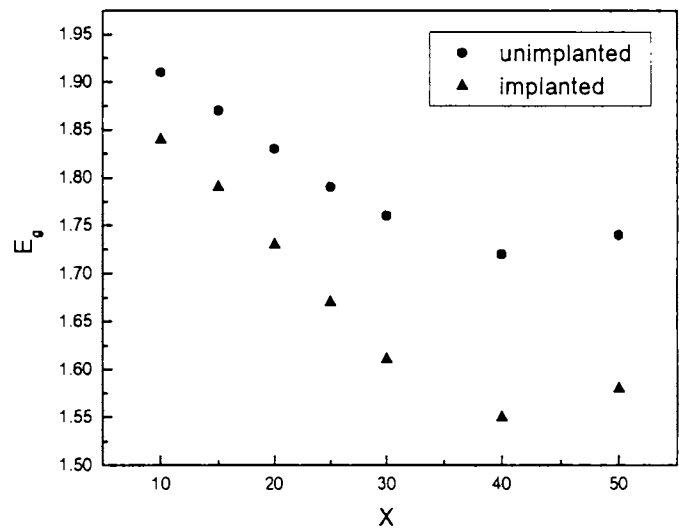correspondingly, E_g decreases. Such an effect is maximum at the stoichiometric

Fig.6.11. The variation of optical energy gap (E_g) with composition index x for thin film samples of As_xSe_{100-x}
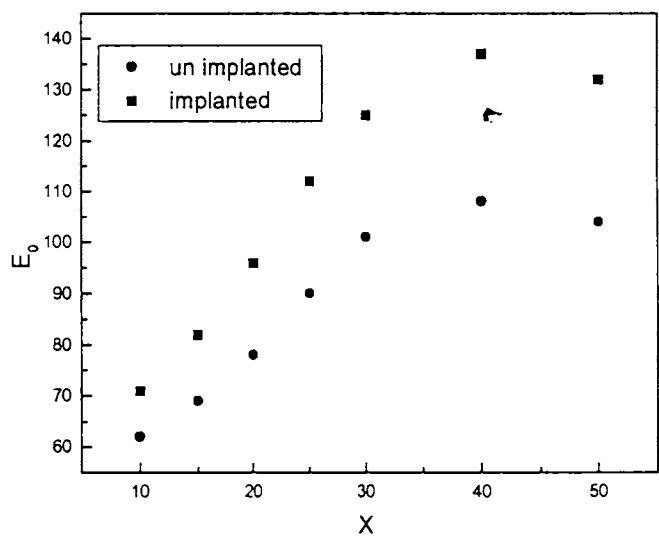

Fig.6.12. The variation of inverse logarithmic slope (E_0) with composition index x for thin film samples of As_xSe_{100-x}

composition where As-Se bonds are maximum. This interaction and the effect of it in E_g variation with x is also associated with network disorder. Such a conclusion is also supported by the nature of variation of inverse logarithmic slope E_0 with x. The E_0 value increases with x, similar to the case of Ge-Se, showing that increase in network disorder increases with increase in coordination. These arguments can be confirmed from the variation of E_g and E_0 in implanted sample. Here, E_g shows similar variation as in the case of unimplanted sample, but with relatively smaller E_g values (Fig.6.11). E_0 shows higher values in comparison with unimplanted sample (Fig.6.12). The composition dependence of E_0 is similar to unimplanted sample though, again, the rate of increase is higher for higher x values. As seen in the case of Ge-Se, the network disorder increases in implanted As-Se samples also. From the variation of E_g and E_0, it is clear that the network disorder plays an important role in modifying the valence band edge in this lone pair system.

6.4. Conclusions

Optical absorption measurements in nitrogen implanted thin film samples of Ge_xSe_{100-x} ($5 \leq x \leq 40$) and As_xSe_{100-x} ($10 \leq x \leq 50$) glass systems have been carried out by PDS. The profiles of ion range and vacancy distribution are obtained by the TRIM simulation for implantation. The variations of the optical energy gap (E_g) and the inverse logarithmic slope (E_0) with implantation for different

166

compositions of both the samples are investigated. For the Ge-Se system, it is found that E_g has a maximum value at the stoichiometric composition x = 33, while for the As-Se system, a minimum value of E_g is obtained at its stoichiometric composition x = 40. For both the systems, the value of E_g is found to be smaller and the value of E_0 is found to be higher for implanted samples compared to unimplanted samples. However, the behaviour of the variation of E_g as well as E_0 with x is similar for both implanted and unimplanted samples. Also, for both the systems, the value of E_0 shows a maximum for the stoichiometric composition. These results are explained on the basis of chemically ordered network model proposed for amorphous semiconductors and also on the basis of structural changes taking place in the glass network due to ion bombardment.

References

1. Hamakawa, "Non Crystalline semiconductors" ed.M.Pollak, Vol. 1 (CRC Press, 1987)

2. A.Madan and M.P.Shaw, "The Physics and applications of amorphous semiconductors" (Academic Press, 1988)

3. E.A.Davis, "Amorphous Semiconductors", ed: M.H.Brodsky (Springer – Verlag, Berlin, 1979)

4. J.C.Phillips, Physics Today 2 (1982) 27

5. R.Zallen, "The Physics of Amorphous Solids" (John Wiley, New York, 1983)

6. G.A.N.Connell, "Amorphous Semiconductors", ed: M.H.Brodsky (Springer-Verlag, New York, 1979)

7. K.Tanaka, Current Opinion in Sol.State and Mat.Sci. 1 (1996) 567

8. R.A.Street and N.F.Mott, Phys.rev.Lett. 35 (1975) 1293

9. M.Kastner, D.Adler and H.Fritzsche, Phys.rev.Lett. 37 (1976) 1504

10. K.L.Bhatia, G.Parthasarathy, A.K.Sharma and E.S.R.Gopal, Phys.Rev.B 38 (1988) 6342

11. N.Amer and J.D.Jackson, "Semiconductors and Semimetals", vol. 21B, ed: J.l.Pankove (Academic, New York, 1984)

12. K.L.Narasimhan and Shailendra Kumar, Ind.J.of Pure & Appl. Phys. 27 (1989) 390

13. A.C.Boccara, D.Fournier, W.B.Jackson, and N.M.Amer, Opt. Lett.
5 (1980) 377

14. J.Tauc, "Optical Properties of Highly Transparent Solids", ed: S.S.Mitra and B.Bendow (Plenum, New York, 1975) 245

15. J.Tauc, "Amorphous and Liquid Semiconductors", ed: J.Tauc (Plenum, London, 1974) 159

16. G.D.Cody, T.Tiedje, B.Abeles, B.Brooks and Y.Goldstein, Phys.Rev.Lett. **47** (1981) 1480

17. K.N.Madhusoodanan and J.Philip, Phys.Stat.Sol.(a) **108** (1988) 775

18. G.Lucovsky and T.M.Hayes, "Amorphous Semiconductors", ed: M.H.Brodsky, (Springer – Verlag, Berlin, 1979)

19. T.Wagner, S.O.Kasap and K.Maeda, J.Mater.Res. **12(7)** (1997) 1892

20. R.T.Sanderson, Chemical Bonds and Bond Energy (Academic Press, New York, 1971)

21. D.E.Polk, J.Non-Cryst.Solids **5** (1971) 365

22. Alex Mathew and K.N.Madhusoodanan, Asian J.of Spectroscopy 7(1) (2003) 27

Chapter 7

Summary and Conclusions

This is the concluding chapter incorporating overall conclusions of the work presented in earlier chapters. Further scopes for the work that can be done in this direction on other chalcogenide glass systems are also discussed.

Amorphous semiconductors are mainly classified into two groups as tetrahedrally coordinated semiconductors like a-Si, a-Ge etc and chalcogenide semiconductors like Se, Ge-Se, As-Se etc. One of the major differences between these two groups of materials is the coordination number and the network features associated with it. This difference is reflected in many of the physical properties as well as in the preparation techniques. a-Si is generally prepared in thin film form condensing from the vapour phase whereas chalcogenides can be prepared in bulk glass form as well as in thin film form. The tetrahedrally coordinated materials form an overconstrained network with four fold coordination whereas chalcogenides can be prepared with different coordination numbers, starting from 2 for Se, with the addition of other elements. The work presented in this thesis deals with the optical studies carried out in representative systems belonging to both these classes of materials.

We have selected silicon as a representative of the family of tetrahedrally co-ordinated materials and the thin film samples of the glass systems Ge_xSe_{100-x} ($5 \leq x \leq 40$) and As_xSe_{100-x} ($10 \leq x \leq 60$) as representatives of the class of chalcogenides for our studies. For the preparation of thin films, we have also designed and fabricated a vacuum coating unit capable of creating ultimate pressures of about 10^{-5} Torr. Initially we carried out the optical characterization of the thin film samples of the systems Ge-Se and As-Se, which includes the

determination of their optical band gaps and refractive indices, using conventional UV-Vis-NIR spectrophotometer. For the Ge_xSe_{100-x} system, it is found that the band gap E_g increases with increase in Ge content for $x < 33$ and decreases for $x > 33$, thus giving a maximum value for $x = 33$, the stoichiometric composition of the system. For the As_xSe_{100-x} system, a minimum in the band gap E_g is observed at the stoichiometric composition $x = 40$. The results are explained on the basis of different models proposed for the systems. It is found that the refractive index decreases with the increase in wavelength and also that the variation of refractive indices of these samples with composition is in close correlation with the variation of densities with composition of the samples.

Incorporation of impurities into a semiconductor by high-energy ions is a non-equilibrium process which can result in intriguing property changes in the material. Ion implantation is a key technology for the fabrication of doped layers in silicon semiconductor microelectronic devices. Also the nature and extent of defects/network modification produced during such a process are important from the point of view of basic understanding. In this context, we have carried out a study of implantation effects in the two classes of materials by the technique of ion implantation. Optical absorption measurements in the implanted samples have been carried out by Photothermal Deflection Spectroscopy (PDS). The technique, being very sensitive, enables the

measurement of optical absorption over a wide range in the weak subgap absorption region. We have used the technique to characterize the defects, amorphization and annealing behaviour in silicon implanted with B^+ ions. The profiles of ion range and vacancy distribution are obtained by the TRIM simulation for implantation. The effect of ion dose, implantation temperature and thermal annealing on the subgap optical absorption are investigated. The changes induced in the band edge slopes and in the subgap features of the spectra are described. It is found that the subgap optical absorption depends very much on the nature and evolution of defects. The formation of divacancies significantly influence the subgap absorption. The various stages of formation, quenching and annealing of divacancies are monitored as a function of implantation conditions and annealing cycles. It is observed that for amorphization with light ion like boron, implantation has to be performed at low temperature. Investigations have also been carried out on the structural modifications and defect evolution under annealing in amorphous material produced by implantation.

We have used optical method based on photothermal beam deflection technique to carry out thermal diffusivity measurements on the thin films of the systems Ge-Se and As-Se . The experiment has been performed making use of the phase method and the results are verified using the amplitude method. The variation of thermal diffusivity with composition for the two sets of samples

has also been investigated. It is observed that for Ge_xSe_{100-x} system, the value of thermal diffusivity D shows a peak value at the stoichiometric composition x = 33 and a discontinuous change is observed at x = 20, while the As_xSe_{100-x} system shows a maximum value of D at x = 40 corresponding to its stoichiometric composition. The observed variation is explained on the basis of structural changes taking place with composition in the glass network in both the systems.

As the defect related absorption is closely associated with many of the physical effects in chalcogenides, it is interesting to study the optical absorption by introducing additional defects by the techniques like ion implantation. In this context, we have carried out optical absorption measurements by PDS in nitrogen ion implanted thin film samples of Ge_xSe_{100-x} ($5 \leq x \leq 40$) and As_xSe_{100-x} ($10 \leq x \leq 50$) glass systems. The profiles of ion range and vacancy distribution are obtained by the TRIM simulation for implantation. The variations of the optical energy gap (E_g) and the inverse logarithmic slope (E_0) with implantation for different compositions of both the samples are investigated. For the Ge-Se system, it is found that E_g has a maximum value at the stoichiometric composition x = 33, while for the As-Se system, a minimum value of E_g is obtained at its stoichiometric composition x = 40. These results are comparable to those obtained earlier using conventional technique. For both the systems, the value of E_g is found to be smaller for implanted samples compared to

174

unimplanted samples. However, the behaviour of the variation of E_g with x (i.e; the presence of maximum at the stoichiometric composition) is the same for both implanted and unimplanted samples. As it is possible to measure the absorption in the subgap region over a wide range with PDS technique, the exponential absorption tail region and the weak absorption region are also present in the spectrum. The values of inverse logarithmic slope E_0 obtained from exponential tail regions were presented for both implanted and unimplanted samples. For Ge-Se and As-Se systems, the value of E_0 shows a maximum for the stoichiometric composition. It is also found that E_0 values for implanted samples are higher than those of unimplanted samples. The above results are explained on the basis of chemically ordered network model proposed for amorphous semiconductors and also on the basis of changes in network structure taking place in the glass network due to ion bombardment.

It would be interesting to study various physical properties of amorphous materials having coordination from 2 to 4 in order to have a comprehensive understanding about the role of network topology. The influence of the change in network topology can be investigated by modifying the network structure with techniques like ion implantation. The presence and nature of coordination defects in such networks need to be investigated. The microscopic nature of such defects has to be investigated by techniques which

can probe the local coordination. This opens up scope for wide ranging

investigations in these amorphous semiconductors.